Report no: CSM/MT/CWJCR/2012/002

FINAL PROJECT REPORT

EFFECT OF CONCENTRATION AND TEMPERATURE OF ETHANOL IN FUEL BLENDS ON MICROBIAL AND STRESS CORROSION CRACKING OF HIGH-STRENGTH STEEL

USDOT-PHMSA Project No. DTPH56-08-T-000014

Submitted by

Colorado School of Mines
Luke jain, Brajendra Mishra, David L. Olson
John R. Spear, Chase Williamson
National Institute of Standards and Technology
Timothy Weeks, Jeff Sowards
iCorrosion, LLC
Russell D. Kane

Submitted to

US Department of Transportation
Pipeline Damage Prevention, Detection and Characterization, Defect Remediation and Repair and New Fuels Transportation

[Performance Period: May 15, 2008 – October 14, 2011]

CENTER FOR WELDING, JOINING & COATINGS RESEARCH

DEPARTMENT OF METALLURGICAL & MATERIALS ENGINEERING

FEBRUARY 2012

EXECUTIVE SUMMARY

Localized environments in fuel grade ethanol (FGE) transportation systems, where conditions are suitable for growth, may allow for microbiologically influenced corrosion (MIC) of steel components. Interstate pipeline transportation of ethanol fuels increases the potential impact of a MIC related failure. A laboratory MIC investigation is presented to evaluate the potential for increased susceptibility of linepipe steels to MIC when low concentrations of ethanol are present. This research is supported by a microbiological field survey of FGE infrastructure. Acetic acid producing bacteria (APB) and a sulfate-reducing bacterial (SRB) consortium are isolated from a failed storage tank used to capture ethanol spillage and runoff water at a fueling terminal. Electrochemical corrosion testing and electron microscopy is applied to study MIC of API X52 and API X70 linepipe steels by these isolated bacteria. Electrochemical techniques including open circuit potential (OCP), polarization resistance (PR), and electrochemical impedance spectroscopy (EIS) evaluate corrosion kinetics and electrochemical properties of the steel-solution interface. Scanning electron microscopy (SEM), and energy-dispersive X-ray spectroscopy (EDS) are applied to study corrosion products and morphology. Qualitative MIC models are presented to explain corrosion mechanisms operating in the experimental systems. A multi-specimen four-point bend testing (MSBT) method is developed to screen for crack initiation and reductions in mechanical properties due to microbially influenced embrittlement. Electrochemical corrosion data indicate acceleration of steel corrosion rates due to SRB in ethanol and acetic acid environments. Localized corrosion is identified on API X52 and X70 steels exposed to APB and on API X70 exposed to SRB. Neither cracking nor reduction of mechanical properties was identified on either steel in either environment.

TABLE OF CONTENTS

CHAPTER 1 STATEMENT OF PURPOSE

Materials Compatibility in Fuel Transportation

This investigation arises in response to material compatibility challenges posed by the introduction of new fuels to existing transportation infrastructure. New steel/environment combinations are continually being presented in the energy sector due to the evolution of energy technology and changes in political and market forces governing the supply of and demand for different fuel types. Regardless of the driving force for these changes, the dynamic state of the industry presents both challenges and opportunities for materials scientists to characterize material compatibility in these new environments. Effective understanding of these compatibility issues is essential to warn of potential dangers, optimize performance, and develop new technologies.

This research is concerned with promoting the safe, reliable transportation of ethanol fuels in interstate pipeline systems. Often, metallurgical failure and corrosion research is directed toward a material compatibility problem only after that problem presents itself in the form of a costly and sometimes devastating failure. This program reflects an effort to evaluate the potential for a material compatibility problem before it is encountered in field operations.

Domestic Fuel-Grade Ethanol Production and Distribution

Recent interest in fuel grade ethanol (FGE) and ethanol fuel blends (EFB) has resulted from domestic energy public policy and the increasing production of FGE in the United States within the last few decades. As of November of 2008, thirty years of subsidies for the U.S. corn based ethanol industry totaled $30.4 billon (Carlson 2008). Executive and legislative agendas, including those laid out in the Energy Policy Act of 2005, the President's 2006 State of the Union Address, and Executive Order 13432, present strategies to displace the use of gasoline refined from mostly foreign oil sources with renewable fuels including ethanol (Ethanol Road Mapping Workshop 2007). The 2007 Energy Independence and Security Act mandated the annual production of 36 billion gallons of ethanol and other biofuels by 2022 (Carlson 2008). A total of $5 billion dollars was anticipated to be spent in 2008 alone in the form of a 51 –cent tax refund on each gallon blended with gasoline (Carlson 2008). Inspiration for ethanol use has in part come from Brazil who achieved energy independence in 2006 with the help of its domestic ethanol industry. Brazil has since become a net exporter of energy.

The increase in FGE production, shown in

Figure 1.1, has been accompanied by several ethanol stress corrosion cracking (eSCC) failures in tanks and piping lines. Government funds have since been allocated for material compatibility research and development of new and existing fuel transportation systems. The U.S. Department of Transportation Pipeline and Hazardous Materials Safety Administration (DOT-PHMSA) was tasked with removing any transportation barriers to an ethanol-fuel economy (Ethanol Road Mapping Workshop 2007).

The majority of ethanol is manufactured at corn-based production facilities in the northern Midwest while

the majority of demand is located in population centers distributed along coastal regions (
Figure 1.2).

Domestic FGE is primarily shipped by truck, rail, and barge. Disadvantages of trucking include higher cost and the danger associated with carrying large volumes of fuel on the interstate system. Transportation by truck, rail, and barge is much more expensive than transportation by pipeline as shown in Table 1.1. With current FGE production costs, foreign FGE could be imported if financial incentives to domestic ethanol producers were eliminated. The FGE imports, presumably from South America, would likely require additional means of transportation.

There are approximately 100,000 miles of refined products pipelines in the United States, which transport around 6 billion barrels of fuels annually (Zamarin 2007). These lines are relatively safe and cost effective. Most of these pipelines primarily operate as multi-product lines and function as batch delivery systems. Unfortunately, existing infrastructure is not designed to deliver refined product from the Midwest to the eastern and western coastal population centers. Overland shipping needs for imported ethanol would also have to be addressed to facilitate transportation from ports to population centers. Solutions to ethanol transportation issues would likely involve constructing new fuel pipelines or establishing a combined pipeline and barge system routing ethanol through the Gulf Region.

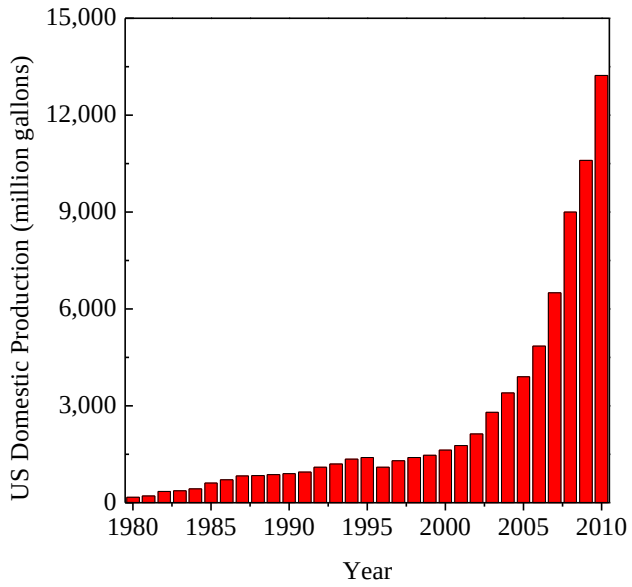

Figure 1.1 Estimated Historic U.S. Fuel Ethanol Production (RFA 2011)

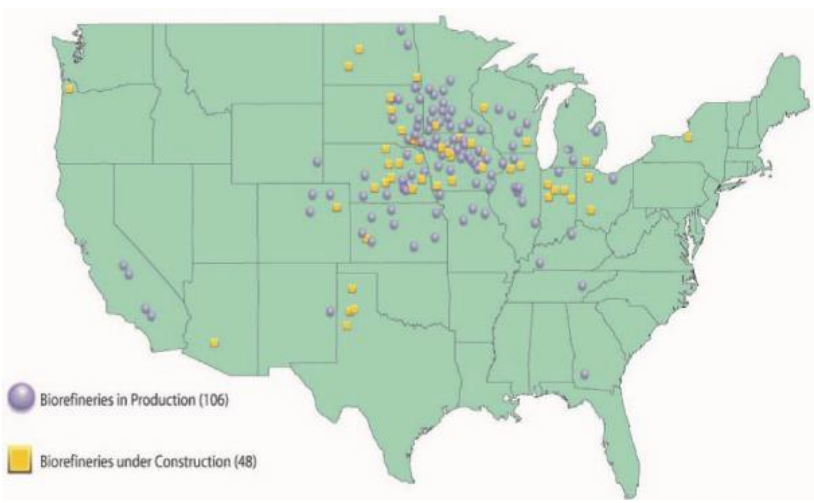

Figure 1.2 Ethanol Producers (Renewable Fuels Association 2008)

Table 1.1 Gasoline Transportation Costs (Curley 2008)

Transportation Method	**Approximate cents/gal (per 1000 mile)**
Pipeline	1.5-2.5
Barge	4-5
Train	7.5-12.5
Truck	30-40

Considerations for Microbially Influenced Corrosion in FGE Systems

The introduction of FGE and EFBs to pipeline infrastructure is likely to pose additional corrosion problems. A newly characterized environmental cracking phenomenon, affecting tank and linepipe steels, eSCC, was recently discovered (Kane and Eden 2007). Ethanol would also likely dissolve and incorporate residual compounds present inside multi-product pipeline systems. As water is completely miscible in ethanol,

pipeline transport may leave behind residual quantities of ethanol, water, and organic compounds in the lines. These compounds are apt to supply all of the necessary nutrients for microbial communities. Ethanol is known to serve as a carbon source at low concentrations for both aerobic and anaerobic microbial communities. Localized environments in FGE and EFB transportation systems and auxiliary equipment (including pipeline, tanks, piping, and filters) where conditions are suitable for growth, especially during system upsets, may allow for susceptibility to microbiologically influenced corrosion (MIC) of steel components. MIC has been found in aqueous environments, oil wells, fuel transmission lines, and fuel storage facilities. MIC is estimated to be responsible for up to 20 percent of all corrosion costs and is a multi-billion dollar per year problem in the United States alone (Heitz, Flemming and Sand 1996).

MIC should be evaluated for bio-derived fuels as these contain a host of nutrients. Microbiological enhancement of corrosion pitting and cracking is also well established. The potential for MIC of steels has not been investigated in systems exposed to ethanol. The aim of this study is to evaluate the potential for MIC of tank and linepipe steels in environments containing ethanol. The work in this thesis includes detailed corrosion investigation, incorporating electrochemical testing and microscopy of steel corrosion caused by microbes metabolizing ethanol, and application of a new screening method for cracking initiation and embrittlement of steels in corrosive environments.

Fundamental Query

The fundamental line of inquiry guiding this investigation will evaluate the propensity for microbes to accelerate corrosion of steels in environments containing ethanol. The work in this thesis is directed by the following set of governing questions.

Can environments containing ethanol enhance susceptibility of steels to MIC?

1. What forms of corrosion are likely?
2. What corrosion mechanisms are operating?
3. Can microbes influence ethanol stress corrosion cracking (eSCC)?
4. How can a mechanical testing system be developed to analyze the effect of cyclic elastic stress on corrosion and environmental crack initiation?
5. Can cyclic elastic stresses affect MIC in the systems being studied?

CHAPTER 2 LITERATURE REVIEW

The study of microbiologically influenced corrosion (MIC) has developed into an interdisciplinary field encompassing electrochemistry, biochemistry, organic chemistry, interface chemistries, in addition to physical metallurgy, mechanical metallurgy and microbiology. MIC describes the initiation and acceleration of materials deterioration due to microbiologically mediated processes. These processes are varied and can be related to a variety of microbial species including bacteria, archaea, microalgae, and fungi. Naturally occurring MIC generally involves multiple organisms, as pure cultures are not found in the environment. MIC does not result in a single type of corrosion attack. MIC has been implicated in general corrosion, localized corrosion, de-alloying, erosion-corrosion, and environmental cracking processes including stress corrosion cracking (SCC), hydrogen assisted cracking (HAC), and corrosion fatigue (CF). Materials have shown susceptibility to MIC in air, soil, seawater, freshwater, fuel, petroleum reservoir, and other environments. MIC is known to affect a variety of materials, including metals, composites, polymers, concrete, and wood (Little and Lee 2007). Corrosion costs in the USA were estimated at 3.1 pct. of GDP in 1998, approximating $276 billion (not adjusted for inflation) (Kock 2002). MIC has been said to account for 20 pct. of the total cost of corrosion (Heitz, Flemming and Sand 1996). It was estimated that as much as 50 pct. of all corrosion failures in pipelines involved MIC (Booth 1964).

MIC in Fuel Systems

The hydrocarbon fuels that humans use to produce power are also a desirable energy sources for microbial species. This competition for energy locked in these fuels leads to deleterious circumstances for materials incorporated in fuel-carrying systems. MIC has been documented in oil and gas wells, oil and gas pipeline, fuel storage systems, and fuel transmission lines. Bacterial and fungal contamination and growth in distillate fuels has been described for over seventy years (Zobell 1946). Consequences have included fouling of filters and injectors, engine malfunction and damage, fuel gauge malfunctions and increased corrosion of engines, fuel tanks, equipment and facilities, and pipeline. *Cladosporium resinae* is one of the most common hydrocarbon-utilizing fungi. In the 1960's, fungal spoilage of kerosene and corrosion of aircraft tanks, reported for Fury, Boeing and Lockheed aircraft, was attributed predominantly to *C. resinae* (Hill and Hill 2008). Sulphate-reducing bacteria (SRB) have also been isolated from laboratory diesel and water mixtures (Bentoa and Gaylardeb 2001). Ethanol is a commonly utilized carbon source for fermentative bacteria, sulfate-reducing bacteria, acetic acid producing bacteria (APB), and other microbial species.

Microbial Biofilm Development

Although metabolic processes affecting bulk solution chemistry can influence corrosion, MIC has been particularly linked to the action of sessile microbes on the material surface. The colonization of solid surfaces by bacteria has generated substantial interest in MIC engineering and research communities. The process by which bacteria colonize a surface has been broken down into three major stages.

The initial stage in this process is adhesion of microbial cells. Organic conditioning of the substrate encourages this process. Organic macromolecules including proteins, polysaccharides, humic acids as well as smaller molecules including fatty acids and lipids, adsorb to the surface (Little and Lee 2007). Adsorption of these compounds modifies the physical properties of the interface, thereby decreasing the energy required for cellular adsorption. Substrate characteristics that influence adhesion thermodynamics include surface roughness, electrical charge, hydrophobicity, and chemical composition. Cellular characteristics that influence adhesion thermodynamics include cell membrane structure and surface properties such as hydrophobicity and surface charge. Transport of microbes to the substrate also controls cellular deposition. This transport may occur via diffusion, convection, and/or active motion by motile bacteria. It has also been suggested that bulk solution parameters such as electrolyte concentrations, pH, and the concentration of ions in solutions can affect microbial colonization.

Once cells have been immobilized on the surface, biofilm develops. Biofilm growth is governed by factors including nutrient accessibility, hydrodynamics, and the production of extracellular polymeric substances (EPS). EPS is known to encourage colonization and biofilm growth by conditioning the surface, increasing surface irregularity, providing shelter from shear forces in the surrounding fluid, and increasing the surface area available for attachment. Quorum sensing is also believed to coordinate biofilm formation as in the case of *Pseudomonas aeruginosa* (Sauer, et al. 2002).

Biofilms provide conditions in which corrosive bacteria flourish. Biofilms may form in minutes after microbes are introduced into a system (Videla and Herrera 2005). A biofilm thickness of only 12 μm can create anaerobic conditions suitable for SRB activity (Al Hashem and Crew 2004). Organic material associated with the biofilm will impede transport of chemical species toward and away from the substrate. This can produce chemical concentration profiles between the bulk solution and the substrate surface. Areas of the surface not covered by biofilm remain exposed to the bulk solution. Heterogeneities can produce variations in local chemical compositions, including pH and oxygen concentration. Microbial metabolites trapped by the biofilm, such as hydrogen peroxide, can also serve as additional cathodic reactants. These processes are known to induce localized anodes on the surface, subjecting the material to localized corrosion processes. This circumstance is akin to the differential aeration cell, well documented in corrosion literature (Jones 1996). Once initiated, localized corrosion processes, such as pitting, are autocatalytic in nature (Fontana and Greene 1967). Classic autocatalytic pitting mechanisms include film rupture, dissolution, hydrolysis, acidification, and chloride migration.

Ennoblement of steels is also commonly observed in correlation with biofilm development. Suggested reasons for ennoblement under biofilm include lowered pH, the production of oxidizing metabolites, and iron and manganese cycling under the biofilm (H. A. Videla 1996). It should also be noted that in some cases EPS and biofilm have been attributed to corrosion protection (Zuo, et al. 2004).

The third stage in biofilm development is detachment and dispersal. Cells, colonies, and EPS break away from an established biofilm and disperse into the solution. As these cells and polymers approach new surfaces, the cycle repeats.

Microbes Implicated in MIC

All microbes have certain basic environmental requirements necessary for life; water, an electron acceptor, an electron donor, and other nutrients (R. Javaherdashti 2008). Other critical nutrients commonly include suitable forms of nitrogen and phosphorous. Macroscopic quantities of free liquid water are also required for all life.

Naturally occurring microbial organisms exist in micro-ecosystems composed of many different species. One problem with laboratory MIC testing is that much of the research is focused on evaluating one or two isolated cultures. Only a small fraction of microbial species have been cultured in laboratory environments. While laboratory MIC research has produced great insight into MIC processes, it should be noted that laboratory studies of isolated cultures do not provide an inclusive picture of MIC as it occurs in field environments.

Despite limitations to laboratory MIC research, several categories of microbes have been implicated in MIC. The foremost of these are the SRB. While it is commonly thought that the majority of MIC is attributed to SRB, many researchers caution against this generalization (Little and Wagner 1997). Categories of microbes proposed to influence corrosion include acid producing bacteria (APB), sulphur-oxidizing bacteria (SOB), nitrate-reducing bacteria (NRB), iron-oxidizing bacteria (IOB), manganese-oxidizing bacteria (MOB), and magnetic bacteria. Microbes, such as iron-reducing bacteria (IRB) have been demonstrated to retard corrosion by SRB (Lee, Buehler and Newman 2006). In many circumstances, more than one type of microbe was thought to be contributing to corrosive processes. Localized corrosion of buried API X65 linepipe steel was attributed to a combination of anaerobic SRB and APB (Li, et al. 2000). A combination of formative, acetogenic, and SRB have been hypothesized to reside in pipeline facilities and influence carbon dioxide corrosion via microbial production of carbon dioxide and acetic acid (Suflita, Phelps and Little 2008). Microbiological analyses of failed 316L stainless steel service water piping demonstrated the presence of both *Clostridium sp.*, an (APB), and *Leptothrix sp.*, an (IOB) (Gibbon and Zamanzadeh 2008).

Acid Producing Bacteria

Strains of APB are known to manufacture organic and inorganic acids as metabolites. *Acetobacter aceti* have been shown to accelerate corrosion of stainless steels by formation of acetic acid, which destabilized a protective calcareous film formed during cathodic polarization (Little, Wagner and Duquette 1988). Acetic acid production by *Clostridium acetitum* has been documented to promote corrosion (Gibbon and Zamanazadeh 2008). *E. coli* has been shown to influence corrosion by production of organic acids including acetic acid (Little, Wagner and Manfield 1991). The bacterium *Thiobacillus* can produce environments of up to 10 pct. sulfuric acid (S. C. Dexter 2003). Anaerobic spore-formers *Clostridia* and *Butyribacteria* were implicated in internal corrosion of an API X 42 steel natural gas pipeline (Dias and Bromel 1990). The spore-forming SRB *Desulfotomaculum orientis* was also discovered at this site. Pitting initiating at manganese

sulfide inclusions was documented when a microbial consortium containing *Clostridium acetobutylicum*, *C. bifermentans*, *C. butyricum*, and *C. sporogenes* was applied to linepipe steel (Pope, et al. 1988).

Bulk pH can be substantially lowered in solutions containing active APB cultures. Biofilms containing these microbes can lead to even lower pH adjacent to the substrate surface. Microprobes have demonstrated pH values at different locations on the same steel surface ranging from 5 to 9 when exposed to APB (Beech and Gaylarde 1999). Organic acids have been hypothesized to increase corrosion by providing additional cathodic reactants and by chelating metal ions thereby further driving metal dissolution (Wolfgang 1997). Microbially produced organic acids are also thought to compromise the integrity of oxide films and prevent repassivation by oxide formation.

Acetic acid is a commonly produced organic acid. It is one of the simplest carboxylic acids, containing one carboxyl group. The molecule is a polar and miscible in water. Acetic acid is a weak acid, with a pKa of 4.76. A 1 M solution of acetic acid processes a pH of 2.4. The molecular mass of acetic acid is 60.05 g mol^{-1}. Acetic acid dissociation constants in ethanol and water solution can also be found (Grunwald and Berkowitz 1951).

Corrosion behavior of steels in acetic acid has not been thoroughly covered in the literature. Carbon not generally preferred for containments of acetic acid (NACE 1960). Acetic acid corrosion data availability is much more prevalent for stainless steels and other aluminum alloys specified for use with acetic acid. (Craig 1989). Much of the existing published research involving acetic acid and corrosion of carbon steel relates to carbon dioxide corrosion (Crolet, Thevenot and Dugstad, Role of Free Acetic Acid on the CO2 Corrosion of Steels 1999) (Dougherty 2004) (Gulbrandsen and Bilkova 2006). Recent corrosion studies focusing on "top of the line corrosion" also indicate the effects of acetic acid on carbon dioxide and hydrogen sulfide contested acetic acid solutions. For corrosion in acetic acid solutions of less than 5 vol. pct., Table 2.1 may be (Singer, Nesic and Gunaltun, Top of the Line Corrosion in Presence of Acetic acid and Carbon Dioxide 2004) (Mendez, et al. 2005) ew studies have also been dedicated to si) (S. and Mukherjee 2010). The data in

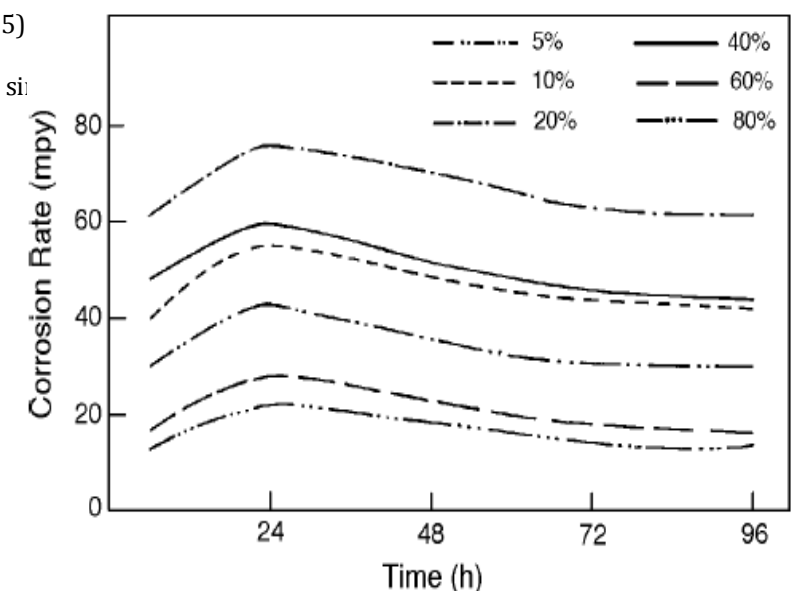

Figure 2.1 Corrosion rate of mild (0.12 pct. C) steel in varying (v/v) concentrations of acetic acid (balance water) with time at 25°C (Singh and Guta 2000)

Table 2.1 Corrosion rates for pure iron and steels in 0.05 M acetic acid solutions with steel 1: 0.10 wt. pct. C, steel 2: 0.25 wt. pct. C, steel 3: 0.50 wt. pct. C, steel 4: 0.65 pct. C, steel 5 0.75 wt. pct. C (Abdel Aal, Wahdan and Gomma 1995)

Specimen	Fe^{2+} ion conc. (M)	$-E_{corr}$ (mV)	i_{corr} (μA cm^{-2})	Trans. coeff. α	η * (mV)	P.I. (%)	b_c (mV)	$i_0 \times 10^{-6}$ (μA cm^{-2})
Pure iron	0	657	43	0.41	0	–	144	1.54
	10^{-6}	650	39	0.41	−1	9.3	144	1.58
	10^{-5}	646	36	0.41	−2	16.3	144	1.73
	10^{-4}	640	36	0.41	−4	16.3	144	1.90
	10^{-3}	641	39	0.41	+12	9.3	144	2.04
Steel 1	0	660	96	0.42	0	–	140	3.31
	10^{-6}	654	94	0.42	−4	2	140	3.46
	10^{-5}	652	99	0.42	−5	–	140	3.63
	10^{-4}	650	100	0.42	−6	–	140	3.80
	10^{-3}	650	107	0.42	−2	–	140	4.07
Steel 2	0	640	209	0.50	0	–	120	3.16
	10^{-6}	638	210	0.50	−3	–	120	3.16
	10^{-5}	636	210	0.50	0	–	118	3.71
	10^{-4}	638	229	0.50	+4	–	116	3.89
	10^{-3}	642	263	0.50	+13	–	114	4.36
Steel 3	0	672	295	0.48	0	–	124	4.68
	10^{-6}	666	289	0.46	−4	2	130	5.24
	10^{-5}	663	288	0.46	+8	2.4	128	5.88
	10^{-4}	660	299	0.46	+7	–	128	6.76
	10^{-3}	655	316	0.46	+9	–	128	7.58
Steel 4	0	633	125	0.50	0	–	120	3.57
	10^{-6}	632	123	0.50	+3	1.6	120	3.63
	10^{-5}	630	125	0.49	+4	–	122	3.63
	10^{-4}	626	123	0.49	+3	1.6	122	3.89
	10^{-3}	629	134	0.48	+2	–	123	4.16
Steel 5	0	614	144	0.46	0	–	120	5.88
	10^{-6}	612	154	0.49	+6	–	122	6.60
	10^{-5}	608	154	0.50	+3	–	120	7.07
	10^{-4}	604	151	0.48	+4	–	123	7.58
	10^{-3}	606	177	0.50	+6	–	120	8.51

* At 0.4 mA.

Acetic acid provides protons for cathodic reduction and may directly reduce on the steel surface (George and Nesic 2007). The acetate anion has also been hypothesized to inhibit anodic dissolution by adsorption to the metal surface (Moussa, et al. 1990). Acetate passivation of carbon steel has been noted in other recent studies (George and Nesic 2007) (De Marco, et al. 2007). The chemical and electrochemical reactions for corrosion by acetic acid are given below:

Dissociation of acetic acid in water (pKa 4.8):

$$CH_3COOH + H_2O \leftrightarrow CH_3COO^- + H^+ \tag{2.1}$$

Anodic corrosion reaction:

$$Fe \rightarrow Fe^{2+} + 2e^- \tag{2.2}$$

Cathodic corrosion reactions:

$$H^+ + e^- \rightarrow \mathrm{H} \tag{2.3}$$

$$CH_3COOH + e^- \rightarrow CH_3COO^- + \mathrm{H} \tag{2.4}$$

Hydrogen recombination:

$$H_{ads} + H_{ads} \rightarrow H_2 \tag{2.5}$$

Acetate adsorption:

$$CH_3COO^-{}_{aq} \leftrightarrow CH_3COO^-{}_{ads} \tag{2.6}$$

Sulfate-Reducing Bacteria

SRB are commonly used to describe those microbes, both bacteria and archaea, which acquire energy by oxidizing organic compounds or hydrogen while reducing sulfates. Many species are also capable of reducing other oxidized sulfur species, including sulfite, thiosulfate, and elemental sulfur. These microbes are associated with the production of sulfides, especially hydrogen sulfide. SRB generally grow in the pH range

4.0 to 9.5 (Barton and Tomei 1995). The organisms do not require oxygen and are generally only active in anaerobic environments. They are also commonly found in association with other microorganisms that provide the nutrients and chemical environment in which they need to survive (Edyvean 1991). SRB are commonly observed in salt marshes and mud flats. This is evidenced by the "rotten-egg" smell from the metabolic production of hydrogen sulfide and a black color commonly exhibited by metal sulfides such as ferrous sulfide.

Many common SRB are classified in the delta subgroup of the Proteobacteria. SRB orders in this subgroup include *Desulfobacterales*, *Desulfovibrionales*, and *Syntrophobacterales*. Other SRB are classified in the phylum Thermodesulfobacteria and Nitrospirae. Organisms in the phylum Nitrospirae include *Desulfotomaculum* sp (Pfennig and Biebel 1986).

A rich tradition of corrosion literature has been dedicated to the study of MIC by SRB (Booth and Wormwell 1961) (Miller 1981) (Tiller 1982) (Hamilton 1985). The "cathodic depolarization theory" put forward in 1934 was the first effort to provide a mechanism for corrosion of metals by SRB (von Wolzgogen and van der Klught 1934). This theory suggested that SRB consume cathodic hydrogen with the hydrogenase enzyme. The removal of the cathodic reaction product from the surface of the electrode was postulated to catalyze the reversible activation of molecular hydrogen. Corrosion acceleration by cathodic depolarization was proposed to proceed according to the following reactions:

Microbial (depolarization):

$$SO_4^{2-} + 8H_{ads} \rightarrow S^{2-} + 4H_2O \tag{2.7}$$

Water dissociation:

$$8H_20 \leftrightarrow 8H^+ + 8OH^- \tag{2.8}$$

Anodic corrosion reaction:

$$4Fe \rightarrow 4Fe^{2+} + 8e^- \tag{2.9}$$

Cathodic corrosion reaction:

$$8H^+ + 8e^- \rightarrow 8H_{ads} \tag{2.10}$$

Corrosion product formation:

$$\mathrm{Fe}^{2+} + \mathrm{S}^{2-} \rightarrow \mathrm{FeS} \tag{2.11}$$

$$3Fe^{2+} + 6OH^- \rightarrow 3Fe(OH)_2 \tag{2.12}$$

Overall:

$$4Fe + 4H_2O + SO_4^{2-} \rightarrow 3Fe(OH)_2 + FeS + 2OH^- \tag{2.13}$$

Since the 1930s, several problems have been discovered with this mechanism (R. Javaherdashti 2008). Hydrogenase is not believed to be able to act on atomic hydrogen. Cathodic depolarization theory suggests that the ratio of corrode iron to iron sulphide is 4:1, however, it varies from 0.09 to 1 experimentally.

Since the formulation of the classic theory for MIC by SRB, several other mechanisms have been suggested. One of these is the production of hydrogen sulfide, which serves as a cathodic reactant. Another is galvanic corrosion between iron and iron sulfide (King and Miller 1971). Some researchers have proposed the reversible deprotonation of hydrogenated phosphate species accelerated by microbial consumption of cathodic hydrogen (Munoz, Alain and Basseguy 2007). Others have suggested that cathodic reduction of ferrous sulfide precipitated over the steel surface may contribute to cathodic depolarization (Starosvetsky, et al. 2010).

Microbial production of hydrogen sulfide generates cathodic reactants and anions to form corrosion product. Extensive literature on hydrogen sulfide corrosion of steels has been published (Kane and Cayard 1998). Hydrogen sulfide corrosion proceeds according to the following reactions:

Hydrogen sulfide dissociation (pK_a 6.9):

$$H_2S \leftrightarrow HS^- + H^+ \tag{2.14}$$

Hydrosulfide dissociation (pK_a 11.96):

$$HS^- \leftrightarrow S^{2-} + H^+ \tag{2.15}$$

Anodic corrosion reaction:

$$Fe \rightarrow Fe^{2+} + 2e^- \tag{2.16}$$

Cathodic corrosion reactions:

$$2H_2S + 2e^- \rightarrow 2HS^- + H_2 \tag{2.17}$$

$$HS^- + e^- \rightarrow S^{2-} + H \quad (2.18)$$
$$H^+ + e^- \rightarrow H \quad (2.19)$$

Direct heterogeneous reaction at the steel surface (Sun and Nesic 2009):

$$Fe_s + H_2S \rightarrow FeS_s + H_2 \quad (2.20)$$

Hydrogen recombination:

$$H + H \rightarrow H_2 \quad (2.21)$$

Corrosion product formation:

$$Fe^{2+} + S^{2-} \rightarrow FeS \quad (2.22)$$
$$Fe^{2+} + HS^- \rightarrow FeS + H^+ \quad (2.23)$$

Anodic corrosion of iron by galvanic coupling with iron sulfide has also been proposed (Stott 1993). Galvanic corrosion attacks the iron matrix adjacent to an iron sulfide deposits. The mineral forms of iron (II) sulfide including mackinawite, greigite, and pyrrhotite, have been suggested as indicator minerals for MIC by SRB (Jack, Wilmott and Sutherby Nov 1995).

Thin adherent pyrite and mackinawite films can be protective. Thin protective iron sulfide films are associated with low ferrous ion concentration rates while active films are believed to form in the presence of high ferrous ion concentrations. These protective films have been proposed to fail due to disruption by microbial action, bulky growth, and oxidation (Edyvean 1991). Corrosion product morphology has been found to be dependent on nutrient supplies in SRB cultures (Sherar, et al. 2010). It has been proposed that the corrosion rate for steel can be defined by the rates of iron sulfide layer formation and breakdown (Sun and Nesic 2009).

Hydrogen sulfide corrosion by SRB has been suggested to be governed by similar parameters. Three stages were described (de Romero 2005). The first stage of the process is the initiation of corrosion by microbial produced hydrogen sulfide. The second stage is passivation by formation of adherent iron sulfide corrosion product. The third stage is the onset of localized anodic dissolution at sites where the protective film has broken down due to chemical and biological action.

Microbial Influenced Environmental Cracking

As discussed, microbial colonization can cause lateral heterogeneity in electrochemical properties across a substrate. Diffusional restrictions through the thickness of the biofilm can produce concentration gradients. These concentration gradients can include dissolved oxygen, aggressive anions, and oxidizing species. In some circumstances, the biofilm itself can act as a physical coating, passivating regions of the surface. Concentration cells produced by bacterial colonization and biofilm development can initiate autocatalytic pitting processes. Pitting has been referred to as the predominate form of MIC (Pope and Morris III 1995). If external stresses are applied to materials suffering localized corrosion, stress concentrations will develop near pits and crevices. These sites of stress concentration can promote the initiation of cracks. In the case of static loading, these cracks could be identified as stress corrosion cracks (SCC). If cyclic loading was applied, the cracks could be classified as corrosion fatigue cracks. In either case, cracking may be attributed to HAC.

In addition to facilitating localized corrosion and pitting, SRB encourages anodic dissolution and retards hydrogen recombination by the production of hydrogen sulfide. Accelerated crack growth rates have been observed for fatigue crack growth rate (FCGR) testing of carbon steel in environments containing SRB (Thomas, Edyvean and Brook 1988). Accelerated crack growth rates were also observed FCGR testing of martensitic steel exposed to SRB in seawater (Gangloff and Kelly 1994). The preferred fracture mode was observed to be intergranular in the abiotic condition but transgranular in the inoculated condition. A study incorporating double-cantilever testing and hydrogen permeation measurements demonstrated increased hydrogen absorption and decreased threshold stress intensities for crack growth of high-strength low-alloy (HSLA) steels (Robinson and Kilgallon 1994). Javaherdashi *et al.* studied environmental cracking of carbon steel by SRB in synthetic seawater (Javaherdashi 2010). Crack propagation was observed to shift from a transgranular to an intergranular mode (Javaherdashti, et al. 2006).

Environmental Cracking in Ethanol Solutions

Slow strain rate testing (SSRT) was performed to evaluate the effect of solution composition on ethanol stress corrosion cracking (eSCC) (Lou, Yang and Singh 2009). Compositional variations were made to a synthetic fuel grade ethanol (SFGE) with a baseline composition of 98.5 vol. pct. ethanol, 0.5 vol. pct. methanol, 1.0 vol.

pct. water, 32 mg/L chloride, and 56 mg/L acetic acid. Higher concentrations of chlorides were observed to increase susceptibility to SCC initiation and growth and result in a higher crack density and velocity. Water concentration had a strong effect on the passivity of the metal surface. A water concentration of 1 vol. pct. gave the highest cracking density and crack velocity. A transition from cracking to pitting was observed with around 2.5 to 5 vol. pct. water. Cracks were observed to initiate from pits at 2.5 vol. pct. water but by 5 vol. pct. water, only pitting was observed. Increasing the alkalinity of the solution was observed to inhibit SCC. Purging the solution with nitrogen eliminated SCC. Slower strain rates yielded larger crack lengths and a higher crack density but a lower crack velocity. Inclusions were thought to serve as crack initiators by producing local plastic deformation.

An electrochemical evaluation of eSCC was also undertaken (Lou, Yang and Singh 2010). Potentiodynamic polarization, electrochemical impedance spectroscopy (EIS), open-circuit potential (OCP), and potentiostatic current monitoring were performed. SSRT specimens were evaluated in a SFGE solution containing 98.5 vol. pct. ethanol, 0.5 vol. pct. methanol, 1.0 vol. pct. water, 32 mg/L chloride, and 56 mg/L acetic acid. These studies indicated that SCC crack initiation in steel was dependent on film rupture associated with plastic deformation. Crack initiation was primarily observed from yielding until UTS, while crack growth dominated from UTS until failure. Crack growth was determined by the competition between anodic dissolution and repassivation ahead of the crack tip. Cathodic polarization was observed to stop SCC.

The influence of solution variables including water, acetic acid, and chloride on corrosion and pitting of carbon steel was also evaluated (Lou and Singh 2010). Water was again closely associated with the stability of the passive film on the steel surface. Increasing water concentrations generally resulted in increased pitting and weight loss, however, pitting corrosion was reduced above 10 vol. pct. water. Chlorides and lower pH (pHe) was observed to increase susceptibility to pit initiation and growth. The presence of chloride was necessary for pitting to occur. Increasing solution alkalinity promoted passive film growth and reduced both pitting and general corrosion.

Investigating Microbiologically Influenced Corrosion

Correctly diagnosing MIC requires a multidisciplinary investigation. Three steps for a MIC investigation are generally to (1) sample the systems experiencing corrosion (2) isolate microbes capable of causing corrosion (3) demonstrate the association between the microbes and corrosion in the laboratory.

Culturing techniques have been used to isolate corrosion causing microbes. Important culturing criteria include the type of media selected, the temperature, and the incubation duration. Planktonic cell counting, turbidity, and chemical reaction can be used to evaluate growth. Other microbial techniques used to determine biota at a specific location include biochemical assays measuring constituents such as adenosine triphosphate (ATP), anti-bodies, and hydrogenase.

Traditional culturing has several disadvantages. It is virtually impossible to replicate a specific field environment in laboratory conditions. The practice relies on the ability of the researcher to produce an environment suitable for growth by the sampled microbes. Culture media known to grow the desired type (SRB, APB, etc.) of organism may preclude growth of other microbes participating in the corrosion process.

Modern genetic techniques involving DNA analysis have proven to be very powerful at assessing microbial diversity and behavior. These studies involve DNA extraction and polymerase chain reaction (PCR) amplification of the small sub-unit ribosomal RNA genes (16S rRNA for Bacteria and Archaea). Extraction and amplification is followed by cloning into *E. coli* with subsequent restriction fragment length polymorphism (RFLP). RFLP patterns are then sequenced by gel electrophoresis on a capillary sequencer. Obtained DNA sequences can then be processed with phylogenetic software using comparative statistical analyses to determine the microbiota present. Organisms known only through their DNA sequence can then be related to organisms in culture. These relations can allow for inferences on the varieties of metabolisms that dominate the *in situ* community. Microbes of interest in the community can be fluorescently tagged with the use of fluorescent *in situ* hybridization (FISH) and visualized for location in the corrosion process. Subsequent cultivation attempts of organisms can be used to understand morphology and physiology of the organisms responsible for corrosion processes. These kinds of phylogenetic studies have recently shown a direct link between community composition and underlying chemistry (Spear, et al. 2005) (Walker, Spear and Pace 2005).

Electrochemical MIC Investigation
Microbial action is known to affect electrochemical conditions on the metal interface. These interactions include changing the open circuit potential (OCP) of the surface, increasing or decreasing corrosion reaction kinetics, or modification of passive films. Changes in the electrochemical properties of a system experiencing MIC can be carefully measured using electrochemical techniques. Common electrochemical corrosion measurements include OCP, polarization resistance (PR), potentiodynamic polarization, pitting potential, split-cell current, electrochemical impedance spectroscopy (EIS), and electrochemical noise. A recent review has been published regarding the use of these techniques for corrosion investigations (Frankel 2008). Comprehensive literature reviews are also available on electrochemical MIC studies (Mansfeld and Little 1991) (Dexter, et al. 1991). Several electrochemical testing methods are often combined (Miranda, et al. 2006).

Open Circuit Potential OCP is measured as the potential of the working electrode relative to the reference electrode in the absence of an applied potential, that is, the the equilibrium potential assumed by the metal. The corrosion current at this potential determines the corrosion rate of the freely corroding metal. Ennoblement indicates a shift in the OCP to more positive or noble potentials. Microbial colonization and biofilm formation on steel surfaces is known to cause ennoblement.

Polarization resistance The PR method is a very common and efficient tool used to approximate corrosion rates. The technique has a long history of application for determining corrosion rates (Prazak and Barton 1967). A more recent review of the method is also available (Scully 2000). Instantaneous corrosion rates can be measured for a system within minutes. Numerous nondestructive measurements can be taken over time to evaluate changes in the same corroding system. The technique is also sensitive enough to measure very low corrosion rates, removing the need for laboratory acceleration of corrosion processes. Measurements are acquired by applying an overvoltage and measuring the resulting current. The approximately linear slope of current to overvoltage is proportional to the corrosion rate. This linearity is only assumed within a few mV of the OCP. A derivation for determining corrosion rate from the polarization resistance technique is presented in Appendix III – Polarization Resistance Method.

Electrochemical Impedance Spectroscopy Electrochemical impedance spectroscopy applies an alternating voltage to a corroding system. This AC impedance technique is modern compared to other corrosion testing methods (F. Mansfeld 1981) (Manfield, Kendig and Tsai 1982). Basic relations for AC impedance are given in Appendix IV – Electrochemical Impedance Spectroscopy. Like the PR method, a voltage signal is applied and current is generated. Voltage-time and current-time data are recorded and reported as electrical impedance of a predetermined frequency range. Experimental data plots can be generated for real and imaginary components of the impedance. Corrosion parameters, including solution resistance, polarization resistance, charge-transfer resistance, and electric double layer capacitance, can be easily extracted from systems exhibiting simple corrosion behavior. These parameters can then be used to realize mechanistic behavior. To evaluate more subtle corrosion parameters, equivalent circuit models can be assembled using defined circuit elements. In some cases, EIS data are fitted to multiple equivalent circuit models to compare relative fitting qualities (Gonzalez, Santana and Mirza-Rosca 1998).
EIS was used extensively in the last several decades to evaluate MIC of steels and stainless steels by SRB. Castaneda *et al.* used EIS to study the evolution of interfacial structures on carbon steel exposed to SRB in artificial seawater (Castaneda and Benetton 2007). Dowling *et al.* investigated the influence of SRB and iron-sulfide film formation on linepipe steel corrosion rates with EIS in combination with SEM (Dowling, et al. 1992). Microbial and solution chemistry measurements were taken in conjunction with EIS to correlated microbial and corrosion processes (Kuang, et al. 2007). Interactions of biofilm and EPS on carbon steel during corrosion by SRB were studied (Perez, et al. 2007). Corrosion product and biofilm formation by different strains of SRB were compared (Sheng, Ting and Pehkonen 2007). Electrochemical impedance has also been applied to study corrosion under conditions of simulated coating disbondment (Xu, et al. 2011).

Microscopy
Field emission scanning electron microscopy (FESEM) is used to generate an image using a high-energy electron beam. Standard electron imaging (SEI) uses secondary electrons to generate high-resolution images.

Backscatter electrons can also be used to generate images using contrast to indicate compositional differences near the surface of the material.

Energy dispersive X-ray spectroscopy (EDS or EDX) is used for chemical characterization. An electron beam is used to eject an electron from an electron shell around an atom. An electron from an outer, higher energy shell drops down to the lower energy to fill the hole. The difference in energy between the electrons is ejected as an X-ray. The energy of the generated X-rays is characteristic for the elements present.

A laboratory corrosion investigation was conducted to evaluate microbiologically influenced corrosion (MIC) of steels in media containing ethanol. The three steels selected for this study were API X52 grade linepipe steel, API X70 grade linepipe steel, and ASTM A36 grade structural steel. The two linepipe steels were recovered from sections of natural gas pipeline recently removed from service. The ASTM A36 structural steel was received from a fuel storage-tank fabricator. Metallography and mechanical properties for the steels are discussed in Appendix I – Steel Materials. Microbes used in MIC testing were collected from a field survey of industrial FGE systems. An anaerobic sulfate-reducing consortium including *Clostridium sp.* and *Desulfosporosinus sp.*, as well as *Acetobacter aceti*, an aerobic acid producing species, was cultured from this survey. Additional information about the microbial field survey, microbial identification and culturing was recorded in Appendix II – Microbial Field Survey. The API X52 and API X70 linepipe steels were used for the electrochemical corrosion experiments. These steels were of primary interest to the project sponsor and most relevant to pipeline transportation. The API X70 steel and ASTM A36 steel were selected for the multi-specimen bend testing (MSBT). These steel were selected as they offered the greatest contrast in mechanical microstructure and mechanical properties of the three. This variety enabled a boarder evaluation of the MSBT method.

Electrochemical Corrosion Evaluation

All electrochemical corrosion experiments were conducted in a common electrochemical corrosion-testing cell. The corrosion flasks, graphite counter electrode rods, purge tubes (when required), reference electrode bridge tubes, saturated calomel reference electrodes (SCE), and Vycor frits were purchased from Princeton Applied Research. Corrosion cells were assembled using standard microbiological and metallurgical guidelines and practices to ensure reliable and repeatable results. Cultured bacteria were introduced into the corrosion cells in the case of positive inoculated experiments while the system was kept sterile for negative control experiments. Open circuit potential (OCP), polarization resistance (PR), and electrochemical impedance measurements were recorded at regular intervals throughout the testing durations. OCP and PR measurements yielded quantitative data to characterize the system. Electrochemical impedance spectroscopy (EIS) data were modeled to give additional quantitative corrosion parameters and gain insight on corrosion mechanisms. At the conclusion of each test, working electrodes were carefully removed from the system and stored in a dessicator. Electron microscopy, using environmental scanning electron microscopy (ESEM) and/or field emission electron microscopy (FESEM), was conducted on the working electrodes to evaluate corrosion morphology. Information given by electron microscopy was combined with electrochemical corrosion data to form the qualitative models presented in Chapter 5.

Testing Plan

The goal of the electrochemical corrosion analysis was to evaluate the influence of acetic acid bacteria (APB) using ethanol as a carbon source and sulfate-reducing bacteria (SRB) using ethanol or acetic acid (a biological metabolite of ethanol) as a carbon source on the corrosion of linepipe steels. Major variables included the presence or absence of isolated APB or SRB and the type of linepipe steel. Two different types of system containment were used for the SRB experiments. The first method of containment relied only on a nitrogen headspace contained by the electrochemical cell and Parafilm coated joints. The Table 3.1.

second method included the application of a 1-inch layer of vegetable oil on top of the testing media. The

Sterilization Procedures

Systems with oil were also affected by elevated temperature and pressure by the sterilization cycle within a Sorvall MT 3781L autoclave at 121°C and 34.8 psi for 27 minutes. The graphite counter electrodes, polymer counter electrode holders, and the complete testing matrix for the electrodes and Vycor frits were autoclaved prior to test

Parafilm coated joints. The complete testing matrix for the electrodes and Vycor frits were autoclaved prior to test

in

24 hrs in a solution of 70 vol. pct. denatured ethanol and 30 vol. pct. deionized (DI) water (30/70 solution). Working electrodes were soaked in 100 pct. 200-proof absolute ethanol for at least 20 minutes prior to assembly. The 200-proof ethanol was used instead of the 30/70 solution to avoid pitting and corrosion of the polished electrode surface. Corrosion cell assembly was performed in a sterile laminar flow cabinet. Cell accessories soaked in ethanol were dried in the cabinet on aluminum foil under ultraviolet light. A supply of 30/70 solution was applied regularly to gloves and other surfaces to ensure maintenance of sterile conditions during the assembly period.

Table 3.1 Electrochemical Corrosion Evaluation Testing Matrix

Test ID	Specimen ID	Media	Bacteria	Containment	Steel
20211	1	APB growth media	ARB	static air	API X52
20211	2	APB growth media	-	static air	API X52
110328	1	APB growth media	ARB	static air	API X70
110328	2	APB growth media	-	static air	API X70
110311	1	Post. B & 2 vol. % EtOH	SRB	N_2	API X52
110311	2	Post. B & 2 vol. % EtOH	SRB	N_2	API X70
110311	3	Post. B & 2 vol. % EtOH	-	N_2	API X52
110311	4	Post. B & 2 vol. % EtOH	-	N_2	API X70
110606	1	Post. B & 1g/liter Hac	SRB	N_2	API X52
110606	2	Post. B & 1g/liter Hac	SRB	N_2	API X70
110606	3	Post. B & 1g/liter Hac	-	N_2	API X52
110606	4	Post. B & 1g/liter Hac	-	N_2	API X70
110523	1	Post. B & 2 vol. % EtOH	SRB	oil & N_2	API X52
110523	2	Post. B & 2 vol. % EtOH	SRB	oil & N_2	API X70
110523	3	Post. B & 1g/liter Hac	-	oil & N_2	API X52
110523	4	Post. B & 1g/liter Hac	-	oil & N_2	API X70

Assembly Procedures

Modified Postgate B media was prepared for the sulfate-reducing MIC experiments. Appropriate amounts of the constituents listed in Working electrodes were prepared in advance of the general assembly of the corrosion cell. Several 1 cm by 1 cm by 0.5 cm steel coupons were cut from the sections of API X52 and API X70 steel pipe. The coupons were cut so that the 1-cm^2 faces were originally facing towards and away from the center axis of the pipe. A 14-gauge insulated solid copper electrical wire was adhered to the coupons with silver conductive epoxy. The coupons were then mounted in two-component LECO cold mounting epoxy with one 1-cm^2 face exposed. After full hardening, the exposed 1-cm^2 surfaces were manually polished on a linear polisher with 120, 240, 300, and 600 grit polishing paper.

Table 3.2 were combined in one-liter jars to make 750 ml of growth media. Each jar was filled with 750 ml of deionized water. Sodium hydroxide solution was added to bring the pH to 7 to 7.5. The aerated solution exhibited a pink color due to the resazurin. With the caps loosely screwed on, jars and media were placed in a Sanyo MLS 3781L autoclave and sterilized at 121°C and 34.8 psi for 27 minutes. The jars were then removed from the autoclave. 200-proof ethanol was sterilized by filtering through a 0.2-micron filter. The filtered ethanol was added to the previously prepared and sterile Postgate B growth media to make the 2 vol. pct. ethanol modified Postgate B growth media. Acetic acid was passed through a 0.2-micron filter and added to

the previously prepared and sterile Postgate B growth media to make the 1 gram per liter acetic acid modified Postgate B growth media. A similar procedure was used to make the acetic acid producing bacteria (APB) growth media. The acetic APB growth media was composed of 0.5 g/L yeast extract, 0.3g/L peptone, 1 g/L sodium chloride, and 5 vol. pct. ethanol. These reagents were also added into DI water. Vegetable oil was sterilized by baking for four hours at 350°F.

Working electrodes were prepared in advance of the general assembly of the corrosion cell. Several 1 cm by 1 cm by 0.5 cm steel coupons were cut from the sections of API X52 and API X70 steel pipe. The coupons were cut so that the 1-cm^2 faces were originally facing towards and away from the center axis of the pipe. A 14-gauge insulated solid copper electrical wire was adhered to the coupons with silver conductive epoxy. The coupons were then mounted in two-component LECO cold mounting epoxy with one 1-cm^2 face exposed. After full hardening, the exposed 1-cm^2 surfaces were manually polished on a linear polisher with 120, 240, 300, and 600 grit polishing paper.

Table 3.2 Modified Postgate B Growth Media

Compound	Concentration [g/L]
KH_2PO_4	0.5
NH_4Cl	1
$CaSO_4$-$2H_2O$	1.26
$MgSO_4$-$7H_2O$	2
Yeast Extract	1
Ascorbic Acid	0.1
Thioglycollic Acid	76 **[uL]**
$FeSO_4$-$7H_2O$	0.5
raszurin (0.1 vol %)	1 **[mL]**

Sterilized corrosion accessories and electrodes were assembled into electrochemical corrosion cells sterile laminar flow cabinet. The polished working electrode was oriented facing upwards in the electrochemical corrosion cell. The tip of the reference electrode bridge tube was placed within 5 mm of the Figure 3.1. Accessories and stoppers were placed in all but one port of the corrosion flask and all working electrode surface as shown in

joints were sealed by wrapping with multiple layers of Parafilm. One stopper contained a small hole (for introduction of bacteria) over which vacuum grease was applied. One allotment (750 ml) of growth media was poured into the last open port, which was subsequently closed and sealed with Parafilm. The corrosion cells were removed from the cabinet and placed in water baths maintained at 30°C with hotplates. The cells were then purged with industrial grade compressed nitrogen through Tygon tubing for two hours. Plastic splitters and regulators were used to distribute equivalent amounts of nitrogen to each corrosion cell. Erlenmeyer flasks were used to make simple water traps. These traps were integrated to ensure that ambient air could not enter the cells if the nitrogen flow was interrupted or discontinued. Approximately 1

vol. pct. household bleach (3-6 pct. aqueous sodium hypochlorite solution) was added to the water baths and water traps to discourage auxiliary microbial growth. A picture was taken of four purging corrosion cells containing aerated modified Postgate B growth media [

Figure 3.2]. Around 12 hours after purging, the solution color changed from pink to colorless, indicating anaerobic conditions. Inoculation was then performed via a sterilized needle and syringe through a small hole in one of the stoppers.

The APB electrochemical corrosion cell assembly varied from the SRB electrochemical corrosion experimental procedure in a few important ways. An autoclaved foam stopper was placed in one the ports of the corrosion flask and loosely covered with sterilized aluminum foil. This arrangement was necessary to allowed oxygen transport into the cell to maintain aerobic conditions. The cell was not purged. As the Figure 3.3.

corrosion cell was maintained at room temperature, a water bath was not required. An assembled APB

Corrosion Cell Media Sampling

Several corrosion cell media samples were removed from experiments "110328-1", "110311-1", and "110311-2" [

Little variation was observed for mechanical properties measured for the tensile specimens tested in liquid nitrogen. Elongation for the API X70 steels, when tested in liquid nitrogen, regardless of any other conditions, varied from 2.4 to 8.6 pct. It should be noted that most specimens failed outside the measured gauge length. UTS for all API X70 tensile specimen was around 160-164 ksi, regardless of any experimental variable. The Ys was not measured for the tensile specimens submerged in liquid nitrogen.

Table 4.1] to measure planktonic cell densities and pH throughout the testing duration. These samples were removed through 10-inch stainless steels needles fitted through the needle port carefully drilled into one of the stoppers. The needles were autoclaved and inserted into the cells during assembly in the sterile laminar flow cabinet under sterile conditions. Parafilm was applied over the syringe adaptor when the needle was not in use. The needle was lifted out of the testing media during electrochemical testing to prevent any possible interference. Media removed through this needle was drawn into a sterile syringe and injected into a sterile tube for storage. Cells were counted in a Petroff-Hausser counting chamber. The pH was measured with a Mettler Toledo pH meter. Both cell density and pH measurements were conducted immediately after removal from the corrosion cell.

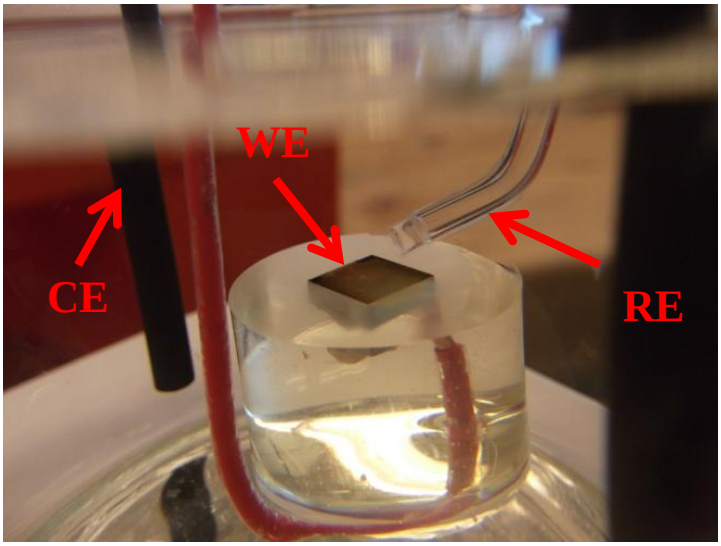

Figure 3.1 API X70 steel working electrode (WE) positioned in an electrochemical corrosion cell adjacent to the counter electrode (CE) and reference electrode (RE) bridge tube

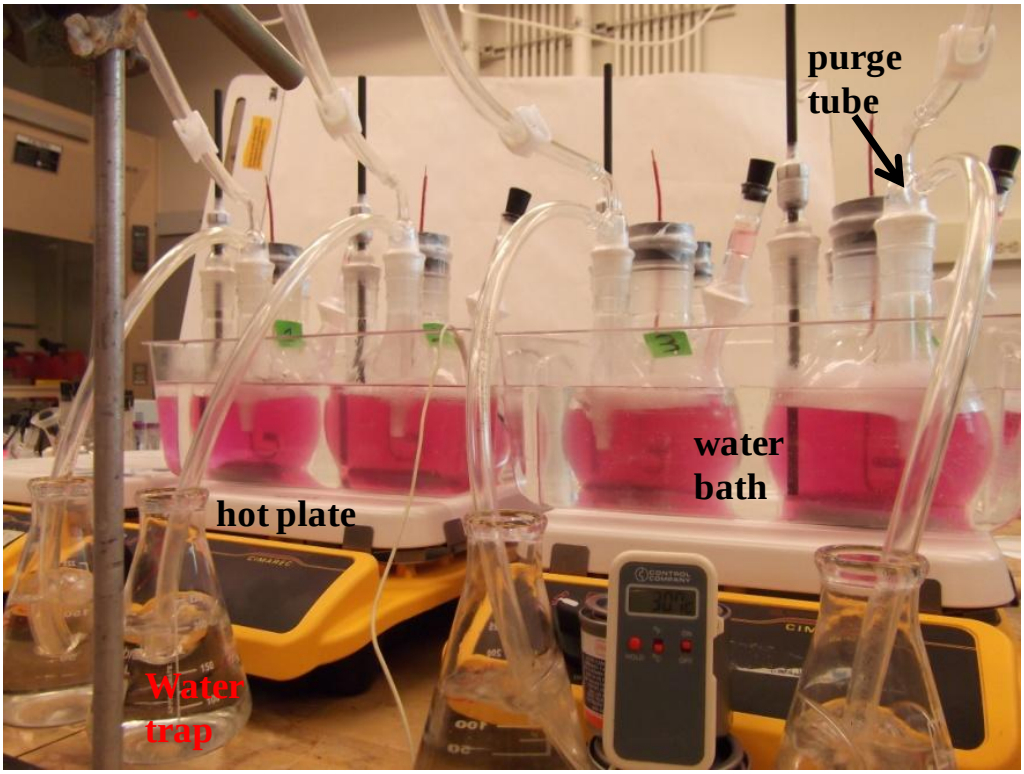

Figure 3.2 Assembled electrochemical corrosion cells containing modified Postgate B growth media purging at 30°C with purge tubing, hotplates, water bath, and water traps

Figure 3.3 Assembled electrochemical corrosion cell containing sterile modified acetic acid producing bacteria growth media

In the case of the API X52 steel with APB experiment, several 50 ml volumes of media were removed from the corrosion cell over the testing duration. The media was replaced with 50 ml of sterile APB growth media to

replenish nutrient levels in the cell. This was performed nine times over the course of the experiment at 1, 3, 5, 8, 12, 14, 21, 26, and 46 days after immersion. The 50 ml aliquots were removed via a 50 ml pipette inserted through one of the ports. Several precautions were taken to discourage microbial migration into the corrosion cell through the open port. All surfaces, gloves and the surrounding areas were thoroughly sprayed with 30/70 solution. A portable burner was lit and positioned under the port to produce a positive pressure to push airborne microbes away from the opening. The insertion and removal of the pipette was performed as quickly as possible while keeping the port partially covered with the stopper to minimize exposure. Cells were counted in a Petroff-Hausser counting chamber. The pH was measured with a Mettler Toledo pH meter. Both cell density and pH measurements were conducted immediately after removal from the corrosion cell.

Electrochemical Testing

Electrochemical testing included OCP and PR measurements as well as EIS. These measurements were conducted at the beginning of the tests and at regular intervals throughout the testing duration. For the first tests, measurements were initially conducted every eight hours until little change was observed in the collected data. Testing frequency was decreased to 12-hour intervals and then to 24-hours intervals. Based on experience from the first several tests, it was observed that there was little change for the first 24 hours and therefore testing at 8-hour increments was begun 24 hours after immersion. Based on the incremental change between consecutively recorded nyquist and bode plots, some EIS data was not modeled (and presented in this thesis) if there did not appear to be significant variations in corrosion behavior.

Due to equipment availability, an EG&G Princeton Applied Research Potentiostat/Galvanostat Model 373A in conjunction with a Schlumberger SI 1255 HF Frequency Response Analyzer was used to conduct electrochemical measurements for the inoculated Postgate B with ethanol experiments. The EIS data from these experiments were modeled using Z-View Version 2.9c software. Electrochemical measurements on all other electrochemical corrosion experiments were performed with a Gamry Instruments Reference 600 Potentiostat/Galvanostat/ZRA. Gamry Echem Analyst ©2009 by Gamry Instruments was applied to model the raw EIS spectra using equivalent electrical circuit models. Fitting was performed using the Levenberg-Marquardt method in the Gamry software. Simple equivalent circuit models were selected that had been applied to similar corroding systems. Circuit models were chosen based on observation of the experimental impedance spectra, knowledge of the corrosion system, and investigation of the surface structure by SEM. Additional time-constants were not added unless these criteria were met. Confidence in the extracted corrosion parameters was based on goodness of fit, modeling error values, and correlation to observed physical structures.

Multi-Specimen Bend Testing

A new methodology was developed to screen steels for susceptibility to environmental cracking. In method, steel specimens were elastically loaded in a four-point bending fixture with a fixed number of loading cycles. The specimens were then removed and the surface was inspected for crack initiation with electron microscopy. After inspection, the bend specimens were split and machined into two tensile specimens that were then pulled to failure to assess mechanical properties. An appraisal of the capabilities and limitations associated with this method was made. A four-point bend configuration was selected to produce a zone of uniform tensile stress on the surface of the specimen. To increase the testing capacity of the study, the special multi-specimen four-point loading fixture shown in Figure 3.4 was designed. Engineering drawings for fixture components can be found in **Error! Reference source not found.**. A set of experiments was conducted to compare steel bend specimens statically immersed in APB and SRB medias with steel specimens immersed in APB and SRB medias while undergoing cyclic elastic loading.

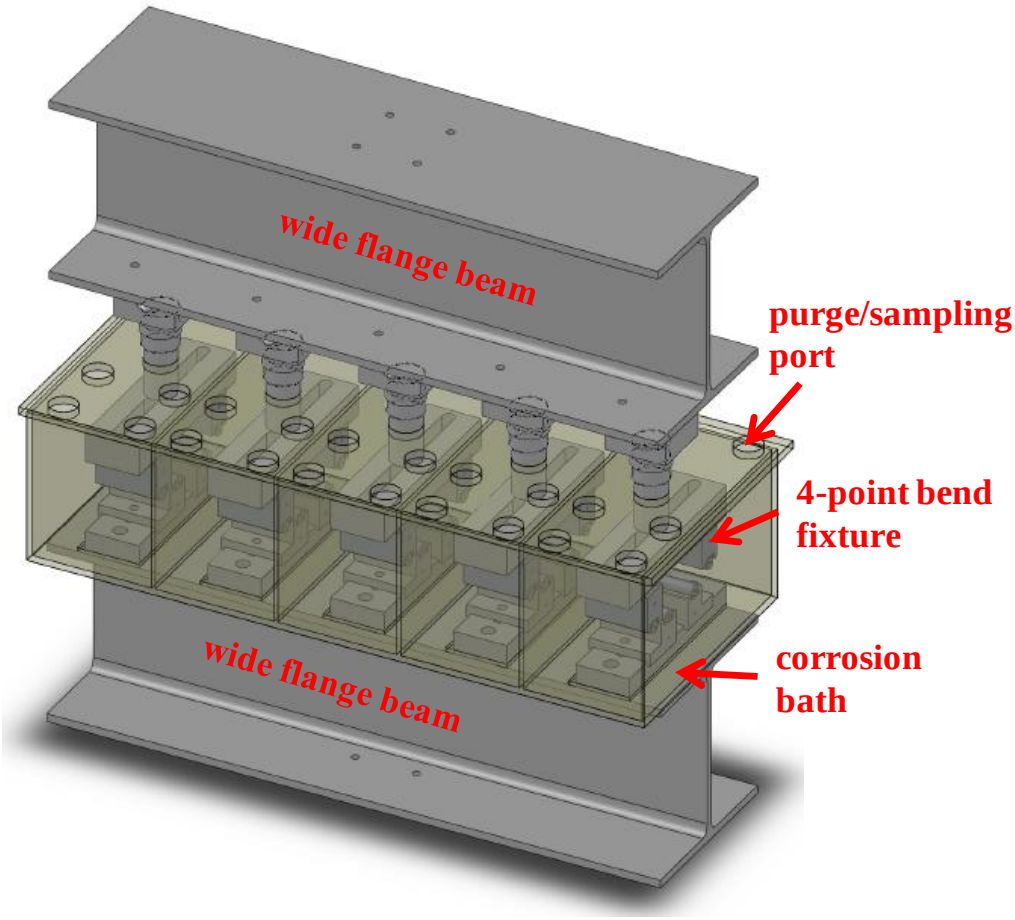

Figure 3.4 Isometric representation of the design for the multi-specimen bend testing (MSBT) fixture

Four-Point Bending

The points of contact on the upper surface of the bend specimen were placed with a greater spacing

contact points on the lower surface of the sample as shown in
Figure 3.5. This arrangement placed the upper half of the specimen in tension and the lower half of the specimen in compression. The outer fibers of the specimen experienced the greatest stresses, tensile and compressive. A neutral axis existed along the center of the beam. A more complete four-point bending analysis is presented in **Error! Reference source not found.**.

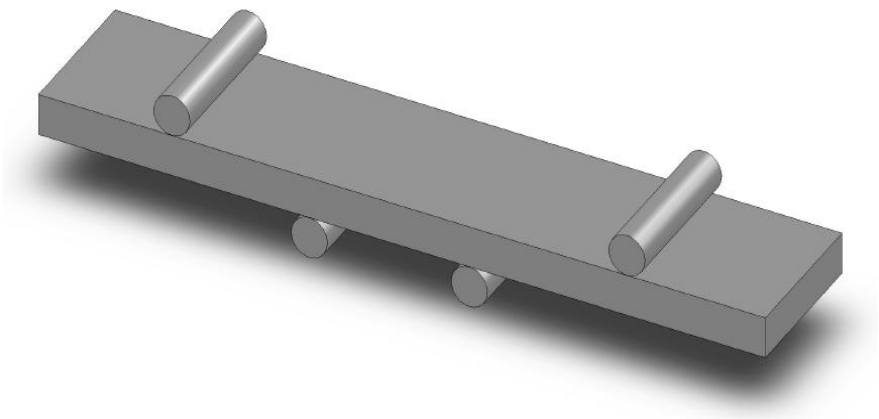

Figure 3.5 Four-point bending configuration (not to scale)

The fixture was mounted on a servo-hydraulic MTS 55-kip loading frame with a MTS 55-kip load cell. TestStar® IIS Controller was used along with MTS MultiPurpose TestWare® software. Loading operated using a repeated deflection cycle with an ideal sinusoidal waveform. Both minimum and maximum stresses

Figure 3.6 Three ASTM A36 steel beam specimens described in Appendix D loaded in the Loading during a series of experiments to assess loading capabilities [Evaluation.

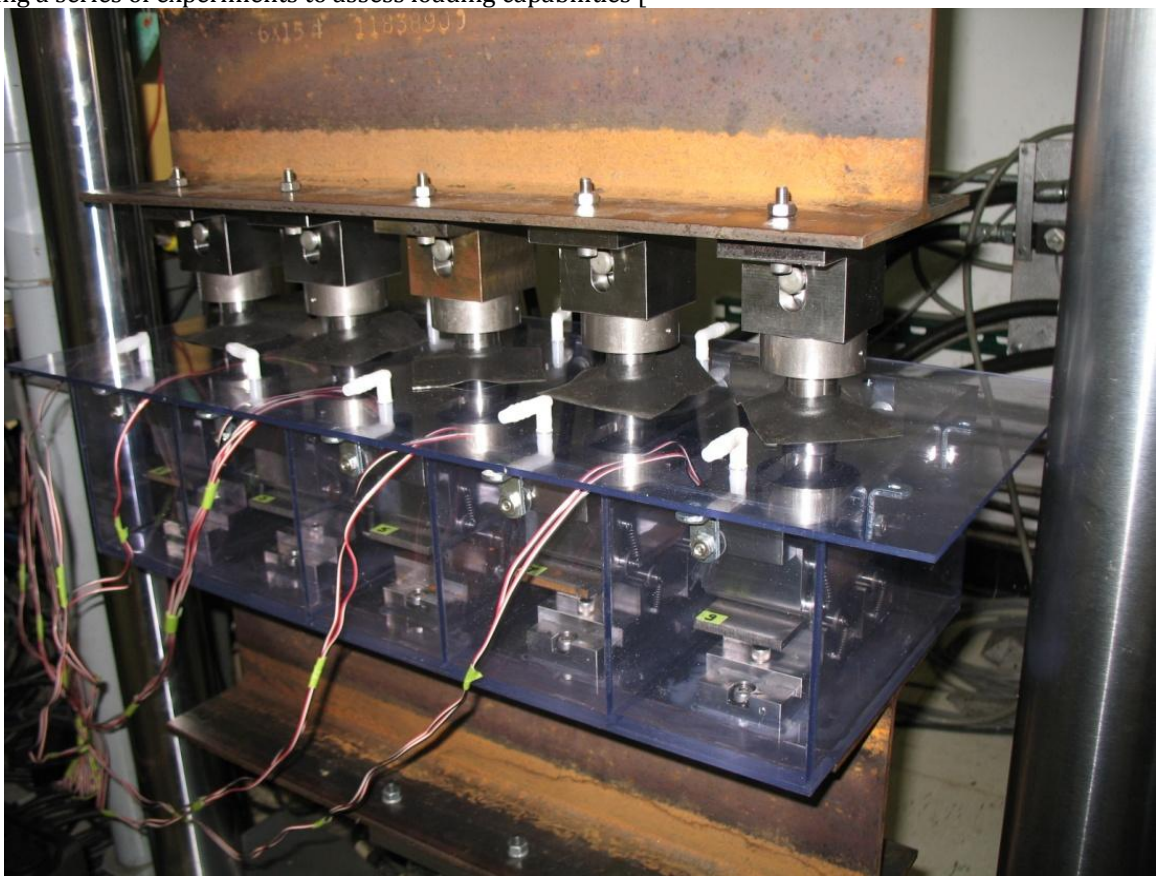

Figure 3.6 MSBT loading trials with strain-gauged ASTM A36 steel bend-testing specimens

Multi-Specimen Bend Testing Plan

The objective of the mechanical testing study was to screen the ASTM A36 steel and API X70 steel for susceptibility to environmental cracking in the selected microbial environments. The specimens were loaded to 500,000 cycles at a frequency of 0.5 Hz. Testing operated in the elastic region of the material from 600 to 1400 microstrain.

The first study (Test ID 0602) in Table 3.3 evaluated ASTM A36 steel immersed in modified Postgate B growth media with 2 vol. pct. ethanol. Two coupons, designated "1" and "3" were set in the bottom of the bend-testing chamber near the base of the four-point bending fixture. The second two coupons, designated "2" and "4" were placed in the four-point bending fixture and cyclically stress for the duration of the test.

The second study (Test ID 0602) in Table 3.3 evaluated ASTM A36 steel immersed in modified acetic APB growth media with 5 vol. pct. ethanol. Two of the coupons, designated "1" and "2" were placed in the four-point bending fixture and cyclically stress while immersed in acetic APB culture media. The third coupon, designated "3" was loaded into an adjacent fixture and loaded in air.

The third test series (Test ID 0602) in Table 3.3 evaluated API X70 steel immersed in modified Postgate B growth media with 2 vol. pct. ethanol. Two of the coupons, designated "3" and "6" were set in the bottom of the bend-testing chamber near the base of the four-point bending fixture. The second two coupons, designated "1" and "2" were placed in the four-point bending fixture and cyclically stress for the duration of the test.

All coupons were removed from the MSBT testing chambers after loading to 500,000 cycles. Several of the bars were inspected with SEM. Each bend specimen was then split and machined into two subscale tensile specimens. One of the tensile specimens from each coupon was pulled to failure at room temperature. The remaining tensile specimen was submerged in liquid nitrogen and pulled to failure. The low-temperature testing was intended to amplify the effect of cracks that may have initiated during immersion.

Sterilization

Sterilization techniques for MSBT were less precise than those employed for the electrochemical corrosion testing, as the set-up was not as conducive to typical sterilization practices such as autoclaving and assembly in a laminar flow cabinet. Prior to immersion, each chamber was filled with 30/70 solution. The bottom side of the lid was also sprayed with 30/70 solution. The upper assembly of the fixture was lowered into the solution, the lid was placed over the chamber, and the chamber was allowed to soak for several hours. The lid was raised just enough to siphon the solution out of the chamber and then set loosely back on the chamber while any residual ethanol and DI water was allowed to evaporate. The steel specimens were sprayed with 200-proof absolute ethanol and immediately placed in the four-point bend fixture and allowed to dry in the clean chamber.

All coupons were removed from the MSBT testing chambers after loading to 500,000 cycles. Several of the bars were inspected with SEM. Each bend specimen was then split and machined into two subscale tensile specimens. One of the tensile specimens from each coupon was pulled to failure at room temperature. The remaining tensile specimen was submerged in liquid nitrogen and pulled to failure. The low-temperature testing was intended to amplify the effect of cracks that may have initiated during immersion.

Assembly

Steel specimens were prepared in advance of the general assembly of the corrosion cells. Specimens dimensions 1 inch (2.54 cm) by 6 (15.24 cm) inch by 0.1875 (0.47625 cm) inch were removed from a plate of ASTM A36 grade steel or sections of API X70 pipe. The 6-inch length was oriented in the rolling direction of the plate for the ASTM A36 steel. The 6-inch direction was oriented in the longitudinal direction of the pipe for the API X70 steel. The coupons were polished to a roughness average of 4.5 microinches perpendicular to the polishing direction. The coupons were washed with dish soap and water, rinsed with DI water and ethanol, dried under forced air, and then placed in an ultrasonic cleaner filled with 200 proof absolute ethanol. The specimens were cleaned in the ethanol ultrasonic bath for 20 minutes, allowed to air dry, and stored in a clean, dry location. Strain gauges were applied to ensure equivalent and consistent loading between bend specimens. Vishay uniaxial strain gauges were applied in quarter bridge configuration to the

epoxy would not be recommended for tests involving high strain levels and plastic deformation, as the epoxy could crack.) Several polished, stamped, cleaned, and gauged ASTM A-36 steel specimens are shown below in Figure 3.7.

Table 3.3 Multi-Specimen bend testing test matrix

Test ID	Bend ID	Media (type)	Innoc. (type)	Stress (Y/N)	Steel (type)	Tensile ID	Cond. (type)
0602	1	SRB_2 % Eth.	SRB	N	A36	0602-1a	room
0602	1	SRB_2 % Eth.	SRB	N	A36	0602-1b	liq. N_2
0602	2	SRB_2 % Eth.	SRB	Y	A36	0602-2a	room
0602	2	SRB_2 % Eth.	SRB	Y	A36	0602-2b	liq. N_2
0602	3	SRB_2 % Eth.	SRB	N	A36	0602-3a	room
0602	3	SRB_2 % Eth.	SRB	N	A36	0602-3b	liq. N_2
0602	4	SRB_2 % Eth.	SRB	Y	A36	0602-4a	room
0602	4	SRB_2 % Eth.	SRB	Y	A36	0602-4b	liq. N_2
0505	1	APB_5 % Eth.	APB	Y	A36	0505-1a	room
0505	1	APB_5 % Eth.	APB	Y	A36	0505-1b	liq. N_2
0505	2	APB_5 % Eth.	APB	Y	A36	0505-2a	room
0505	2	APB_5 % Eth.	APB	Y	A36	0505-2b	liq. N_2
0505	3	Air	---	Y	A36	0505-3a	room
0505	3	Air	---	Y	A36	0505-3b	liq. N_2
0715	1	SRB_2 % Eth.	SRB	Y	X70	0715-1a	room
0715	1	SRB_2 % Eth.	SRB	Y	X70	0715-1b	liq. N_2
0715	2	SRB_2 % Eth.	SRB	Y	X70	0715-2a	room
0715	2	SRB_2 % Eth.	SRB	Y	X70	0715-2b	liq. N_2
0715	3	SRB_2 % Eth.	SRB	N	X70	0715-3a	room
0715	3	SRB_2 % Eth.	SRB	N	X70	0715-3b	liq. N_2
0715	6	SRB_2 % Eth.	SRB	N	X70	0715-6a	room
0715	6	SRB_2 % Eth.	SRB	N	X70	0715-6b	liq. N_2

The APB and SRB growth media were prepared according to the same procedure as for the electrochemical testing. Sulfate-reducing culture was prepared by inoculating a 1 L bottle of modified Postgate B growth media with 5 to 10 ml of the isolated sulfate-reducing culture. The bottle was placed overnight in an anaerobic chamber with the lid loosened. After 24 hours, the solution color changed from pink to clear indicating deaeration of the solution. The lid was tightened and the jar was removed from the chamber. Depending on the microbial activity of the culture, the media generally turned black within 48 hours indicating high sulfate-reducing activity.

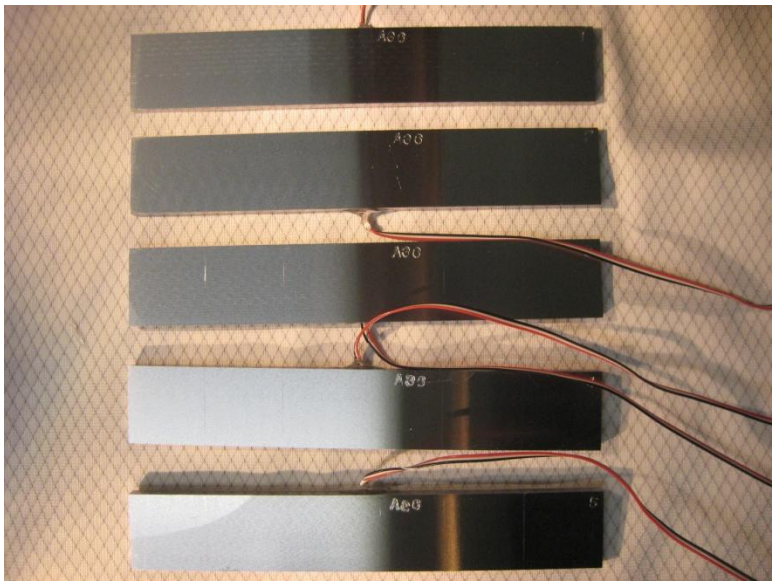

Figure 3.7 ASTM A36 steel multi-specimen bend testing specimens after polishing, cleaning, and strain gauging

After the bend coupons were placed into the fixture, the wire leads from the strain gauges were the Model 3800 Vishay Wide Range Strain Indicator. The 1 L of sulfate-reducing culture was poured into the cell. An additional 400 ml of sterile growth media was also added to the chamber. This nutrient addition was intended to maintain elevated microbial activity over the 12-day testing duration. An allotment of 400 ml of the previously sterilized vegetable oil was then poured onto the media to form a barrier between the growth media and the ambient air over the chamber. The lid was placed over the corrosion cells to form a leaky seal. Figure 3.8.

Tygon tubes immersed in the solution were used to purge the media for a few hours to aid in the deaerated of the solution. The specimens were removed from the bend specimens were machined to the MSBT system, assembled with an

Tensile Testing

Tensile specimens were machined to standard geometry, shown in Figure 3.9. A hydraulic MTS 55-kip loading frame, MTS Model 458 Controller was used along with MTS MultiPurpose TestWare® software. Gauge lengths of 1.35 (3.429 cm) inches were marked on the reduced sections of the specimens to measure total elongation. An Epsilon 1.000 (2.540 cm) inch gauge length extensometer was applied to the reduced section of the specimen. A 50 lb (22.7 kg) preload was applied to the system prior to testing. A stroke displacement rate of 0.05 inches per minute (0.127 cm/sec) was used for all tests. The image in

Figure 3.10 was taken during a room temperature tensile test.

In addition to the experiments using tensile specimens machined from bend specimens, a set of six experiments was run to investigate if a reduction in mechanical properties could be measured for tensile

specimens statically immersed in the MSBT chamber during MSBT testing. During the "0715" MSBT, four API

X70 steel tensile specimens, machined according to

Figure 3.9, were placed in the bottom of one of the testing chambers near to the unstressed MSBT bend specimen. Two specimens were not immersed as un-corroded controls. Immediately after 500,000 cycles had been reached for the bend testing, two of the four immersed specimens were removed and loaded until failure using the previously described loading conditions. One tensile specimen was loaded to failure at room temperature and one tensile specimen was loaded to failure while submerged in liquid nitrogen. Testing performed in liquid nitrogen was conducted to magnify the effect of cracks nucleated on the specimen surface during four-point bending. The remaining two tensile bars were set aside and tested 12 days later. This 12-day delay was to simulate the time (machining turn-around time) from when the bend specimens were removed from the MSBT chamber until when the tensile specimens machining from the bend specimens were tested. The testing matrix for these tensile tests is presented in Table 3.4.

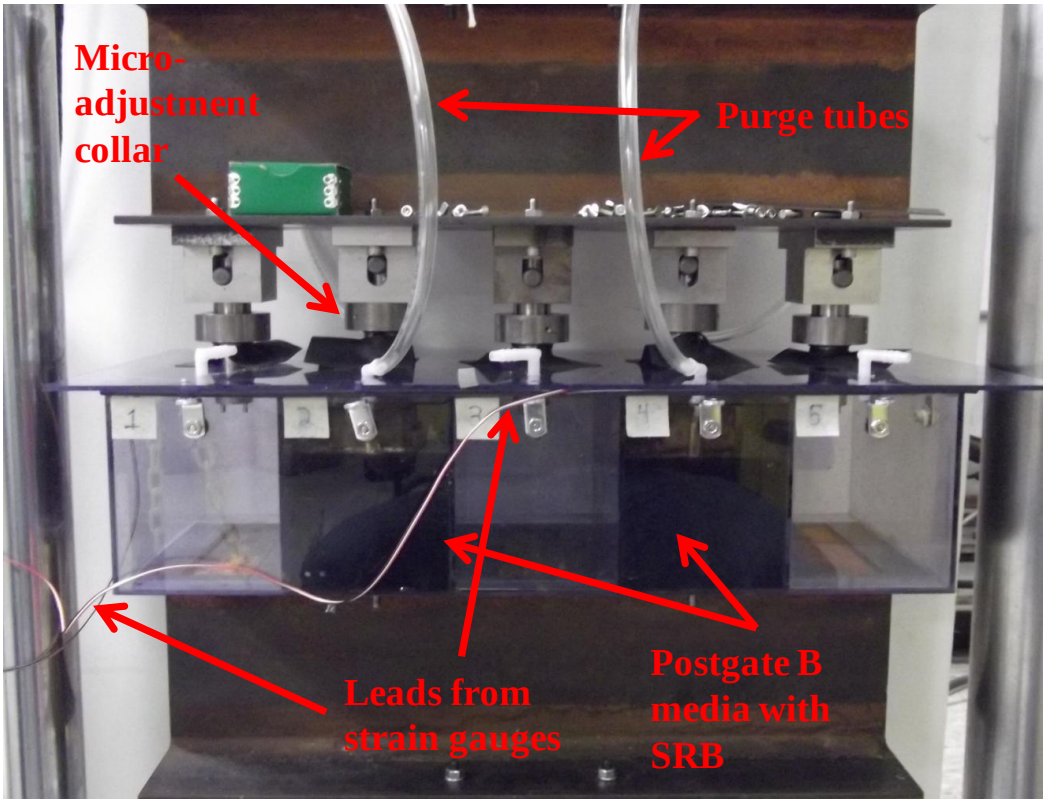

Figure 3.8 Multi-specimen bend testing fixture with chambers two and four containing active sulfate-reducing culture in modified Postgate B growth media covered by vegetable oil with purge tubing, and strain gage wire leads and micro-adjustment collars.

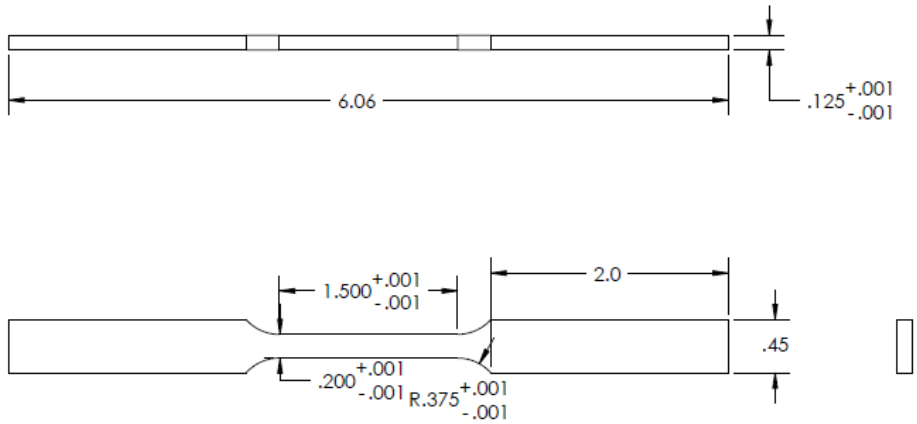

Figure 3.9 Engineering drawing for sub-scale tensile specimens machined from bend specimen with all dimensions and tolerances in inches

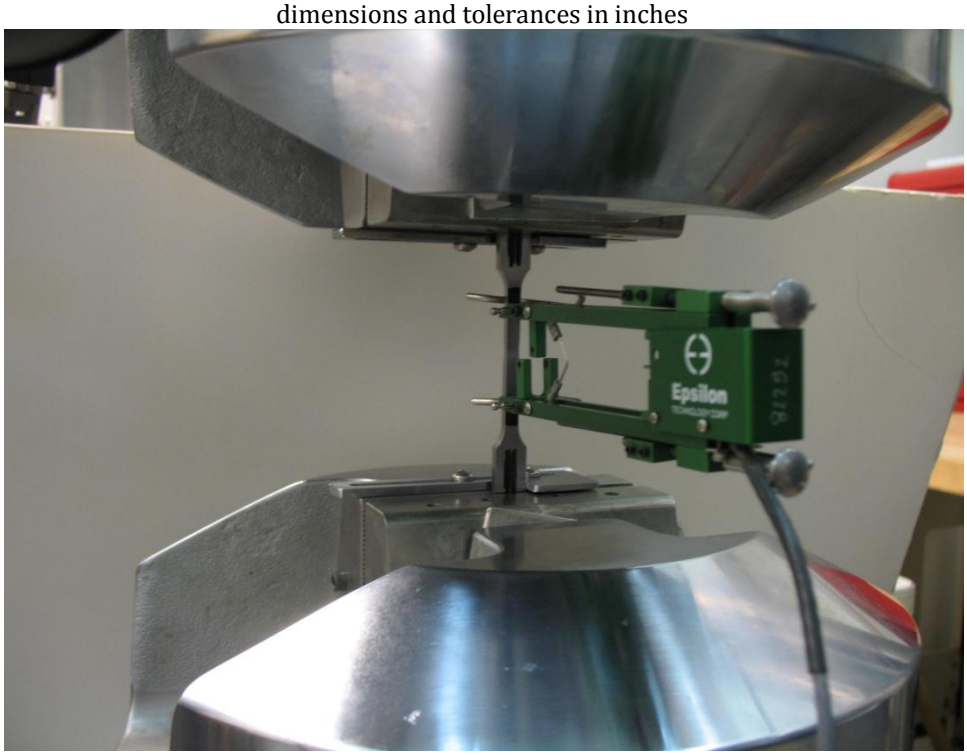

Figure 3.10 Room temperature tensile testing showing wedge grips, extensometer, and tensile specimen

A simple system was designed to conduct the liquid nitrogen tests. A rectangular hole (0.45 in X (1.14 cm X 0.317 cm) was cut in the bottom of a polystyrene cup. The cup was then slipped around the specimen and glued to the specimen with a quick setting two-component epoxy just outside the reduced section of the specimen. The cup extended far enough to submerge the entire gauge length of the specimen in liquid nitrogen. The specimen was then positioned in the grips of the testing fixture. The cup was filled with Figure 3.11 show the liquid nitrogen tensile testing.

liquid nitrogen. The tensile specimen was allowed to soak in the liquid nitrogen for one minute prior to the

Table 3.4 Tensile Testing Matrix

start of the test. Liquid nitrogen was added throughout the testing duration to keep the cup full. The images

in

Test ID	Tensile ID	Immers. (Y/N)	Delay (days)	Cond. (type)
0715	T1	Y	0	room
0715	T2	Y	0	liq. N_2
0715	T3	Y	12	room
0715	T4	Y	12	liq. N_2
0715	T5	N	0	room
0715	T6	N	0	liq. N_2

Scanning Electron Microscopy and Energy Dispersive X-Ray Spectroscopy

Scanning electron microscopy (SEM) can be applied to generate magnified images of the steel surface as well as any biofilm and/or corrosion product associate with it. Energy dispersive x-ray spectroscopy (EDS or EDX) is often used in conjunction with SEM to acquire the chemical composition of features of interest identified by SEM. Information from these tools can be used to investigate corrosion mechanisms.

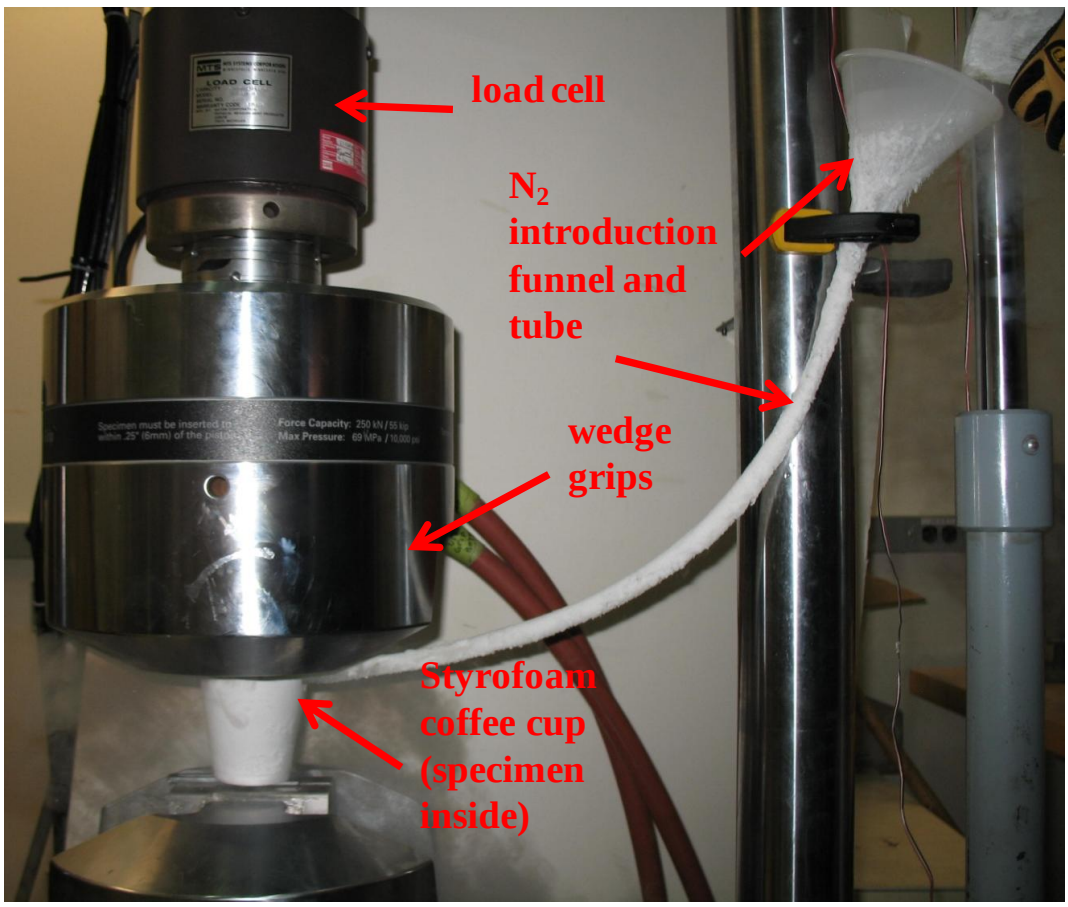

Figure 3.11 Liquid nitrogen tensile testing showing MTS loading frame, wedge grips, polystyrene coffee cup and introduction of liquid nitrogen

Scanning Electron Microscopy

SEM is used to generate an image using a high-energy electron beam. Standard electron imaging (SEI) uses secondary electrons to generate high-resolution images. Backscatter electrons can also be used to generate images using contrast to indicate compositional differences near the surface of the material.

Two scanning electron microscopes (SEM) were used to inspect biofilm, corrosion product, and metallurgical attack on corroded steel specimens. A FEI Quanta 600 Environmental Scanning Microscope with Princeton Gamma-Tech Prism Energy Dispersive X-Ray Spectrometer was used for high-level and lower-magnification microscopy. This instrument was better suited to bring out depth in images and therefore was preferable for capturing pitting morphology and distribution. A JEOL JSM-7000F Field Emission Scanning Electron Microscope with EDAX Genesis Energy Dispersive X-Ray Spectrometer was used to capture small features at very high resolution. Morphological details of approximately 10 to 100 nanometers were captured with this instrument. Pitting, however, was not always readily discernable in this microscope. In general, the environmental scanning electron microscope (ESEM) produced images that brought out differences in depth of surface features while the field emission scanning electron microscope (FESEM) had much higher resolution but yielded a flatter impression.

Energy dispersive x-ray spectroscopy

(EDS or EDX) is used for chemical characterization. An electron beam is used to eject an electron from an electron shell around an atom. An electron from an outer, higher energy shell drops down to the lower energy to fill the hole. The difference in energy between the electrons is ejected as an x-ray. The energies of the generated x-rays are characteristic for the elements present.

CHAPTER 4 RESULTS OF MIC INVESTIGATION

Experimental data from laboratory corrosion testing, conducted according to procedures described in Chapter 3, has been analyzed, modeled and presented. Information presented includes solution properties, electrochemical corrosion parameters, electron microscopy, and mechanical testing data. Observations are made on the presented data. Measurements and observations recorded in this Chapter serve as a basis for the qualitative models and conclusions in Chapter 5. Efforts will be made to correlate microbial behavior, electrochemical properties, and corrosion morphology to explain changes occurring in the system and to develop a mechanistic understanding of the corrosion process.

Electrochemical MIC Investigation

This section covers electrochemical corrosion investigations of API X52 and API X70 steels exposed to the isolated acetic acid-producing bacteria (APB) and sulfate-reducing bacterial (SRB) cultures. Corrosion media samples are taken during some APB and SRB electrochemical corrosion experiments to record the evolution of bacterial activity and solution pH. Electrochemical corrosion analysis includes open circuit potential (OCP) measurements, polarization resistance (PR) measurements, and electrochemical impedance spectroscopy (EIS). Methodologies for applying these techniques to investigate corrosion have been described in detail in corrosion literature (Kelly, et al. 2003).

Experimental EIS data are displayed as nyquist (Z' vs. Z"), modulus (Frequency vs. |Z|), and phase vs. Phase) plots. The high and low frequency limits of the nyquist and modulus plots are commonly interpreted to correspond to the solution and polarization resistances in a corrosion cell. Each peak in the phase plot is commonly interpreted to represent a separate time-constant corresponding to a reactive circuit element such as a capacitor or an inductor. All experimentally acquired EIS data is simulated using one or more of the equivalent circuit models depicted in Figure 4.1.

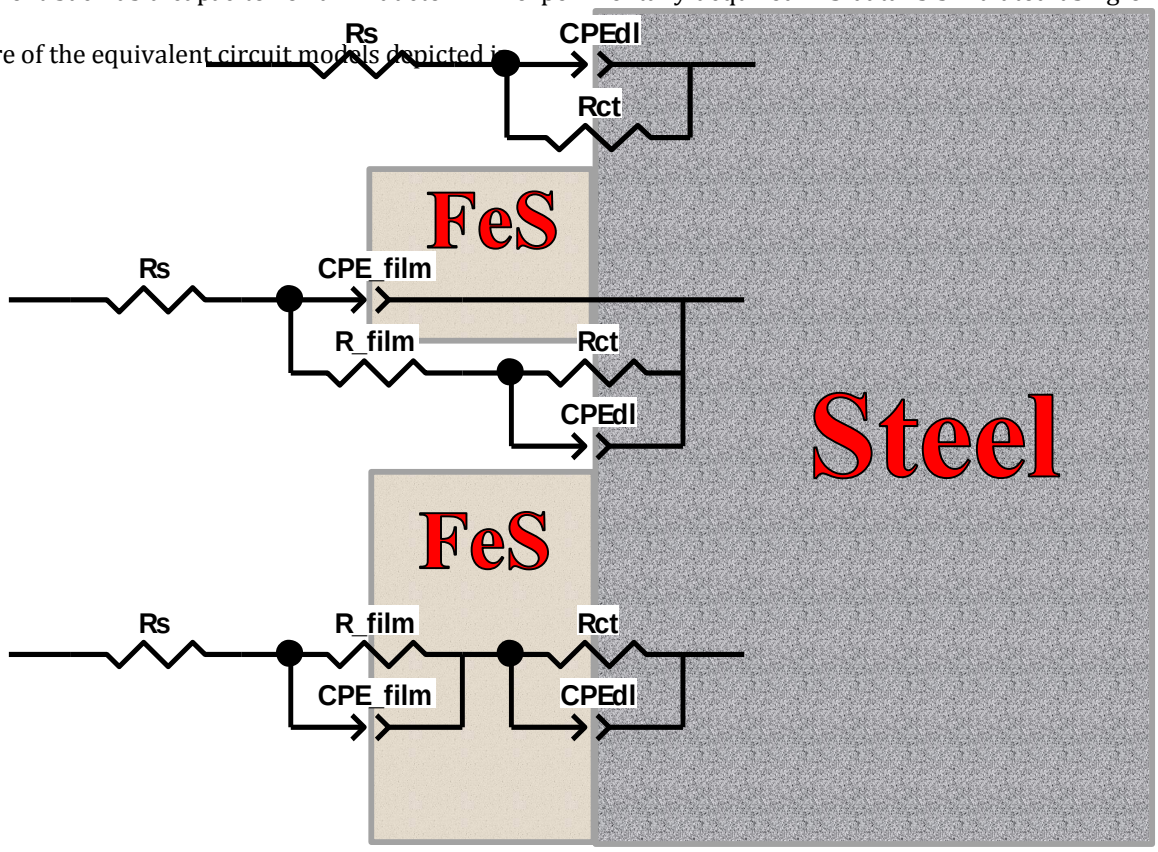

Figure 4.1 Physical relevance of selected equivalent circuit models with circuit elements including R_{ct}, the charge transfer resistance (CTR), R_s or the solution resistance, $CPE_{double\ layer}$ or the constant phase element (CPE) assigned to the metal-solution double layer, R_{film}, the iron sulfide film resistance, and CPE_{film}, the CPE assigned to the iron sulfide film

Corrosion parameters extracted by simulation with equivalent circuit models include:

1. Charge transfer resistance (CTR) labeled on the following Figures as $R_{charge\ transfer}$
2. Solution resistance labeled on the following Figures as $R_{solution}$
3. Double layer capacitance (DLC) labeled on the following Figures as $C_{double\ layer}$
4. The exponential for the constant phase element (CPE), eta, labeled on the following Figures as $\eta_{double\ layer}$
5. Iron sulfide film resistance labeled on the following Figures as $R_{FeS\ film}$
6. Iron sulfide film capacitance (DLC) labeled on the following Figures as $C_{FeS\ film}$

Further information on acquiring, interpreting, and modeling EIS data of corroding systems can be found (Cottis and Turgoose 1991).

Linepipe Steels Exposed to APB with Ethanol

Two experiments were conducted with API X52 steel working electrodes; a positive test inoculated with the APB culture and a negative control test assembled according to the same procedure but without the introduction of the APB culture. Two experiments were also conducted with API X70 steel working electrodes; a positive test inoculated with the APB culture and a negative control test assembled according to the same procedure but without the introduction of the APB culture. The corrosion study, consisting of four experiments, was performed to evaluate the influence of the isolated APB cultures containing the species *Acetobacter aceti* on corrosion of two linepipe steels while consuming ethanol as a carbon source.

EIS data, presented as nyquist, modulus, and phase plots, are displayed in Figure 4.2 (a), (b), and (c), respectively. These data were acquired from the API X52 corrosion cell inoculate with APB at 1, 3, 5, 10, 30, and 60 days after immersion. Several observations can be made directly from the raw EIS data. It can be observed from the modulus plot in that, with the exception of day 1 and 3, the low-frequency limit of the modulus plot remained on the order of 10^4 ohms*cm2 for the duration of the test. The phase spectra exhibit little change over time. This may indicate that the DLC for the system does not significantly change. Additional time-constants are not evident at any testing interval. All three plots in Figure 4.2 demonstrate a peculiar low-frequency decrease in the modulus plot for 1 and 3 days after immersion. This "pseudo-inductive" behavior can be dismissed as it is often attributed to either transient behavior in the system or an undesired surface modification such as adsorption due to extended electrode polarization at low frequencies. To minimize the incorporation of experimental error, the lowest frequency decade was removed for these data sets when equivalent circuit models were applied to extract corrosion parameters.

EIS data, presented as nyquist, modulus, and phase plots, are displayed in Figure 4.3 (a), (b), and (c), respectively. These data were acquired from the sterile API X52 corrosion cell at 1, 3, 10, 25, and 45 days after immersion. The low-frequency limit of the modulus plot remains approximately 10^3 ohms*cm2 for the entirety of the test. The phase spectra exhibit little change over time. This may indicate that the DLC for the system does not significantly change. Additional time-constants are not evident at any testing interval. Some "pseudo-inductive" behavior is observed in the data, particularly at 25 and 45 days after immersion. The lowest frequency decade was removed for the 45-day data set when equivalent circuit models were applied to extract corrosion parameters. The solution resistance can also be observed to increase modestly.

EIS data, presented as nyquist, modulus, and phase plots, are displayed in Figure 4.4 (a), (b), and (c), respectively. These data were acquired from the API X70 corrosion cell inoculate with APB at 4h, 12h, 2, 4, 15, 30 and 60 days after immersion. The low-frequency limit of the modulus plot remained on the order of 10^3 ohms*cm^2 for the duration of the test. The peak in the phase spectra exhibits a slight shift to higher frequencies over time. This may indicate that the DLC for the system slightly increases over time. Depression of the phase peak is apparent. This may suggest increasing irregularity of the metal-solution interface. Additional time-constants are not evident at any testing interval.

EIS data, presented as nyquist, modulus, and phase plots, are displayed in Figure 4.5 (a), (b), and (c), respectively. These data were acquired from the API X70 corrosion cell inoculate with APB at 4 h, 12 h, 2, 4, 15, and 30 days after immersion. The low-frequency limit of the modulus plot remains on the order of 10^3 ohms*cm^2 for the entirety of the test. The peak in the phase spectra exhibits a shift to higher frequencies over time. This may indicate that the DLC for the system slightly increases over time. Depression of the phase

peak is also apparent. This may suggest increasing irregularity of the metal-solution interface. Additional time-constants are not evident at any testing interval. The solution resistance can also be observed to increase modestly.

Planktonic cell densities were intermittently recorded throughout the testing duration for the inoculated corrosion cells. These data are displayed in Figure 4.6 (a). Cell density for the API X52 APB inoculated cell increased an order of magnitude from 1.0 X 10^7 cells per ml to 1.3 X 10^8 cells per ml by the end of the testing duration. Cell density for the API X70 APB inoculated cell increased nearly an order of magnitude from 9 X 10^6 cells per ml to 8.2 X 10^7 cells per ml. Differences in initial cell density values can be attributed to differences in APB culture activities. The initial, faster bacterial growth rate for the API X52 cell may be attributed to growth media replacement as described in Chapter 3. As the frequency of growth media additions decreases, cell density can be seen to decline. After the growth media addition at 46 days after immersion, planktonic cells densities dramatically rise in the inoculated API X52 corrosion cell. Over all, growth media additions do seem to have a positive influence on planktonic cell densities.

The pH was measured and recorded for the inoculated corrosion cells as well as the API X70 control cell. These data are displayed in Figure 4.6 (b). It was assumed that the pH should not change significantly for the negative control tests. This assumption was verified as the negative control pH remained near 6.5. The pH for the API X52 corrosion cell decreased to 3.27 by the end of the test. The pH for the API X70 corrosion cell decreased to 2.65 by the end of the testing duration. Initially, the pH of the API X52 cell decreased at a greater rate than was observed in the API X70 cell. By around day 15, however, the API X52 cell was more acidic than the API X70 cell and remained at a lower pH for the remainder of the testing duration. The greater acidity observed in the API X70 cell indicates that more corrosive bulk solution conditions are not necessarily achieved by nutrient additions.

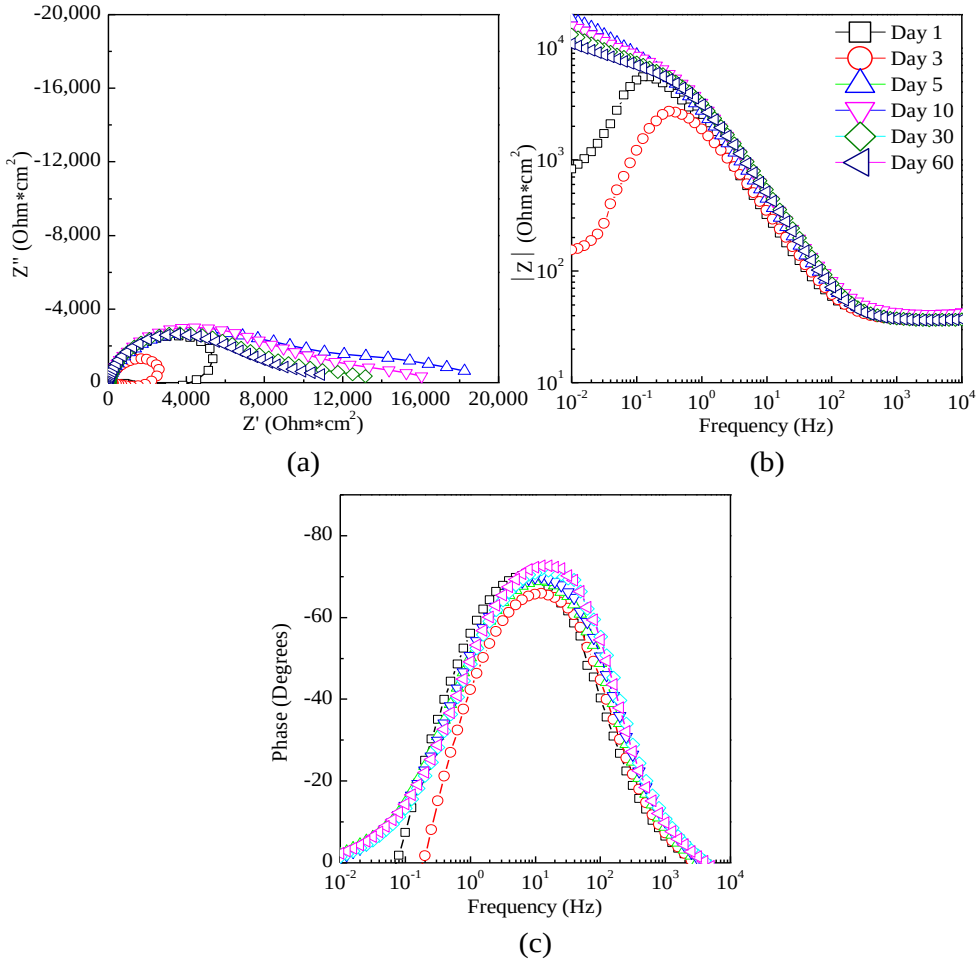

Figure 4.2 Electrochemical impedance data for API X52 steel immersed in modified growth media with five vol. pct. ethanol and inoculated with A*cetobacter aceti* showing (a) nyquist, (b) modulus, and (c) phase plots

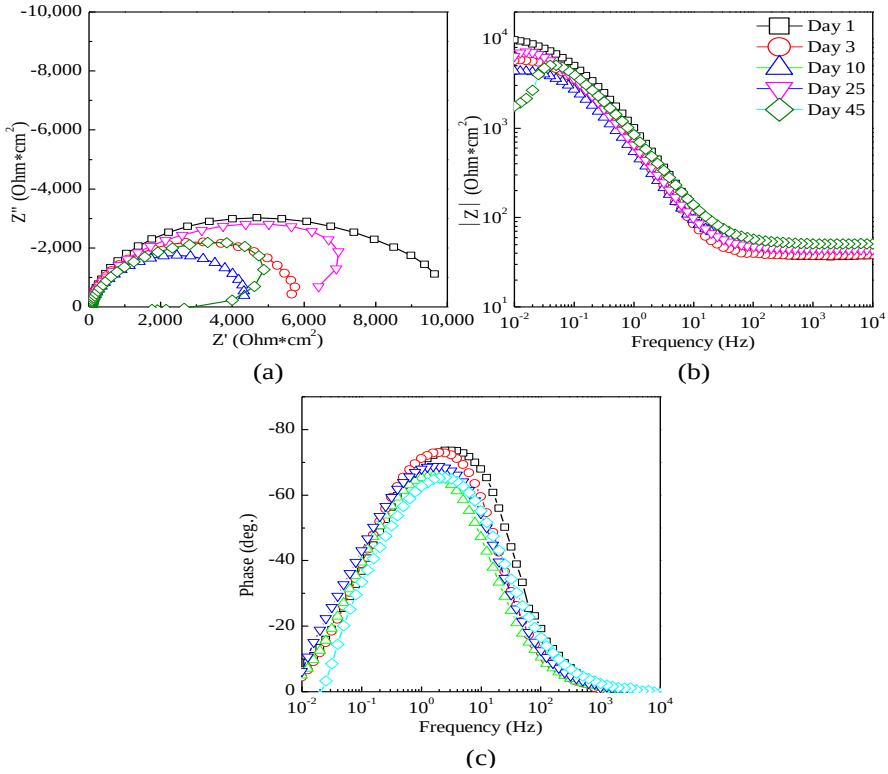

Figure 4.3 Electrochemical impedance data for API X52 steel immersed in sterile modified growth media with five vol. pct. ethanol showing (a) nyquist, (b) modulus, and (c) phase plots

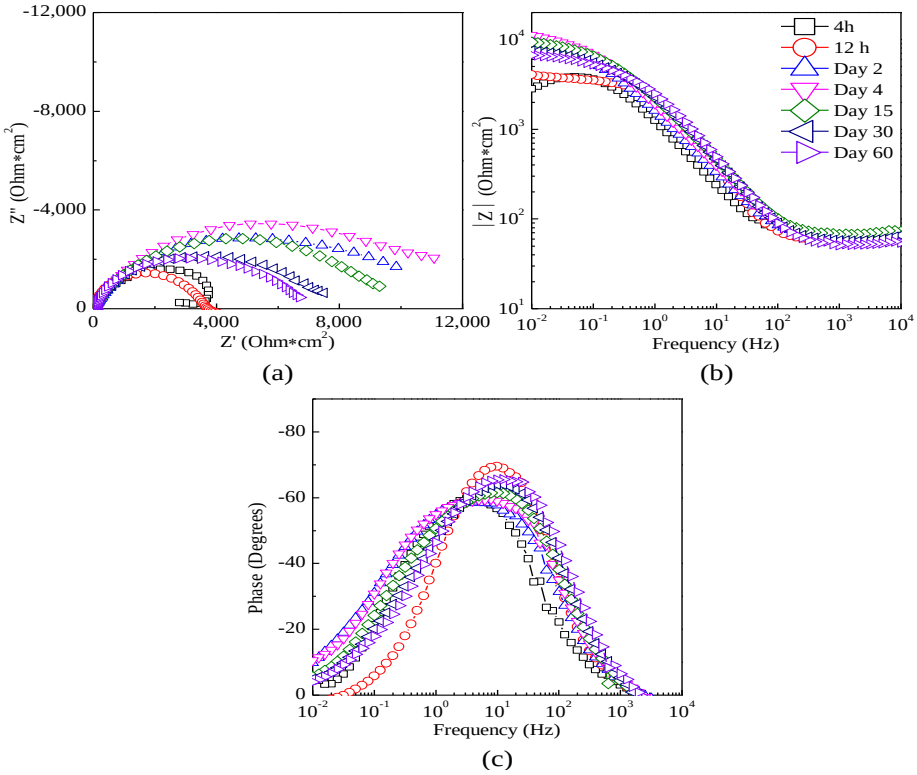

Figure 4.4 Electrochemical impedance data for API X70 steel immersed in modified growth media with five vol. pct. ethanol and inoculated with *Acetobacter aceti* showing (a) nyquist, (b) modulus, and (c) phase plots

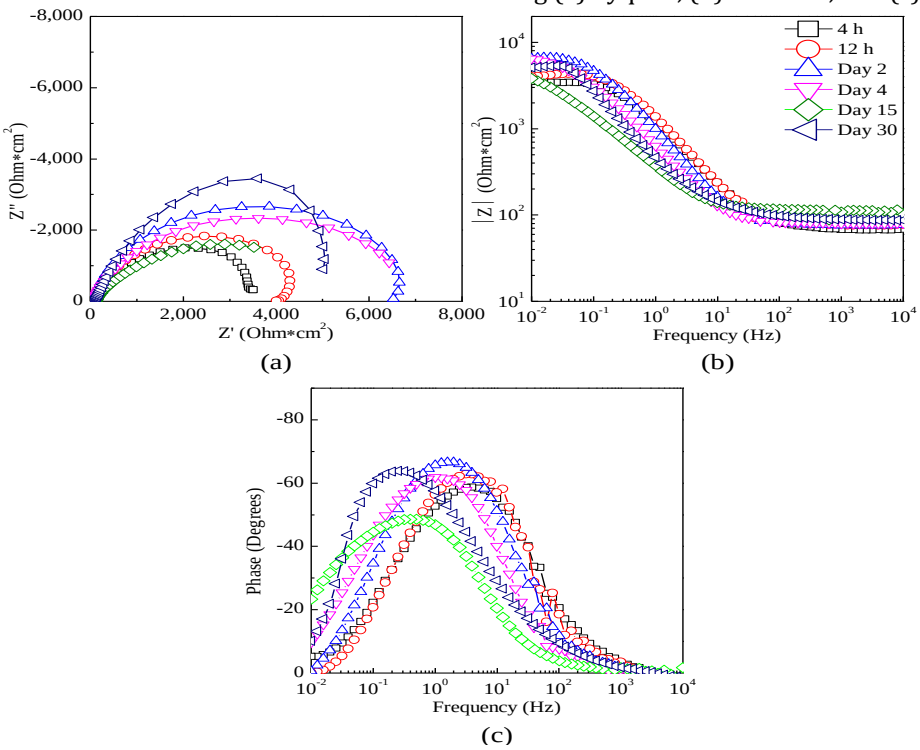

Figure 4.5 Electrochemical impedance data for API X70 steel immersed in sterile modified growth media with five vol. pct. ethanol showing (a) nyquist, (b) modulus, and (c) phase plots

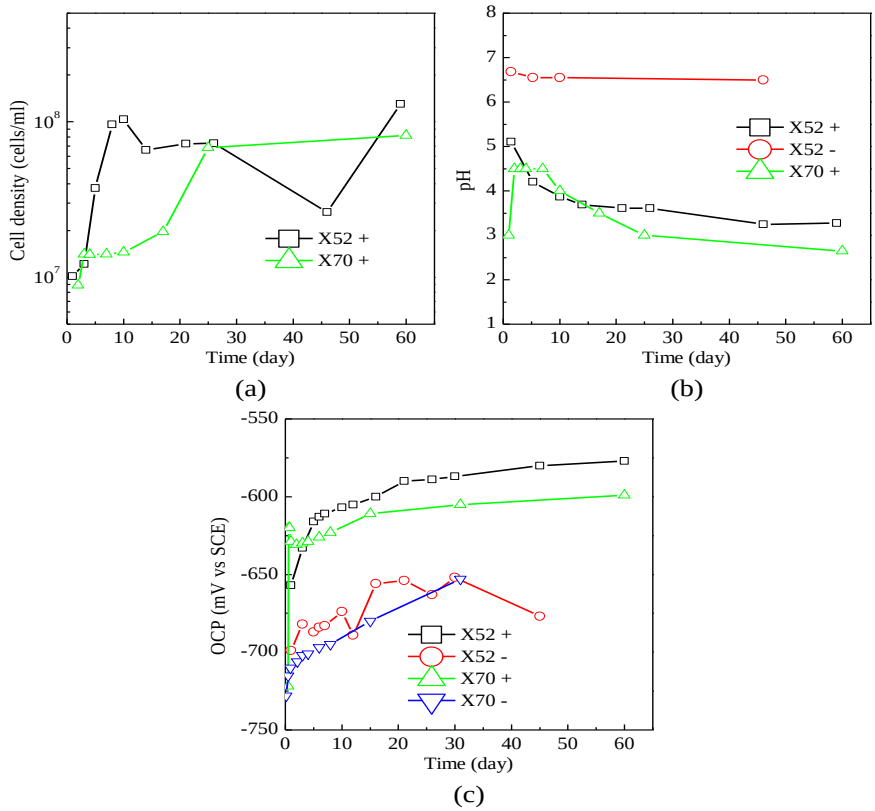

Figure 4.6 Microbial corrosion parameters from corrosion testing of API X52 and API X70 in growth media with five vol. pct. ethanol and inoculated with *Acetobacter aceti* including (a) cell counts, (b) pH, and (c) open circuit potential.

OCP measurements were recorded for all four cells. These data are displayed in Figure 4.6 (a). The OCP for the inoculated API X52 cell was observed to increase from -657 mV vs. SCE to -577 mV vs. SCE. The OCP for the inoculated API X70 cell was observed to increase from -724 mV vs. SCE to -599 mV vs. SCE. The API X52 and API X70 control cells increased from -699 mV vs. SCE to -677 mV vs. SCE and from -728 mV vs. SCE to -614 mV vs. SCE, respectively. The much greater ennoblement observed for the corrosion cells inoculated with acetic APB is consistent with observations in MIC literature (Little and Lee 2007).

The EIS analysis was performed by fitting experimentally recorded data to commonly used equivalent circuit models. The simplest equivalent circuit model commonly fit to corrosion cells is the Randles Circuit shown in Figure 4.7(a). This model was selected because only one time constant was apparent in the raw EIS data. The circuit models the system as a solution resistance in series with an "RC" (resistor and capacitor in parallel) component. The resistor in this component is referred to as the "charge transfer resistance" (CTR). This resistance is the sum of the resistances for all anodic and cathodic corrosion reactions that transfer charge across the metal-solution interface in parallel. The capacitor in the RC component is known as the "electric double-layer capacitance" or more simply the "double-layer capacitance" (DLC). This double-layer is composed by parallel "plates" of excess surface charge on the metal side of the interface and charged species in solution on the solution side of the interface. The charge stored across this capacitor is proportional to the change in voltage across the interface and the distance of charge separation. In this case, an imperfect capacitor known as a constant phase element (CPE) is used. The CPE is defined by a capacitance value as well as the CPE exponent (**η**). Eta can range from zero to one. As Eta approaches one, the CPE acts as an ideal capacitor and as eta approaches zero, the CPE acts as an ideal resistor.

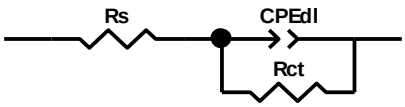

(a)

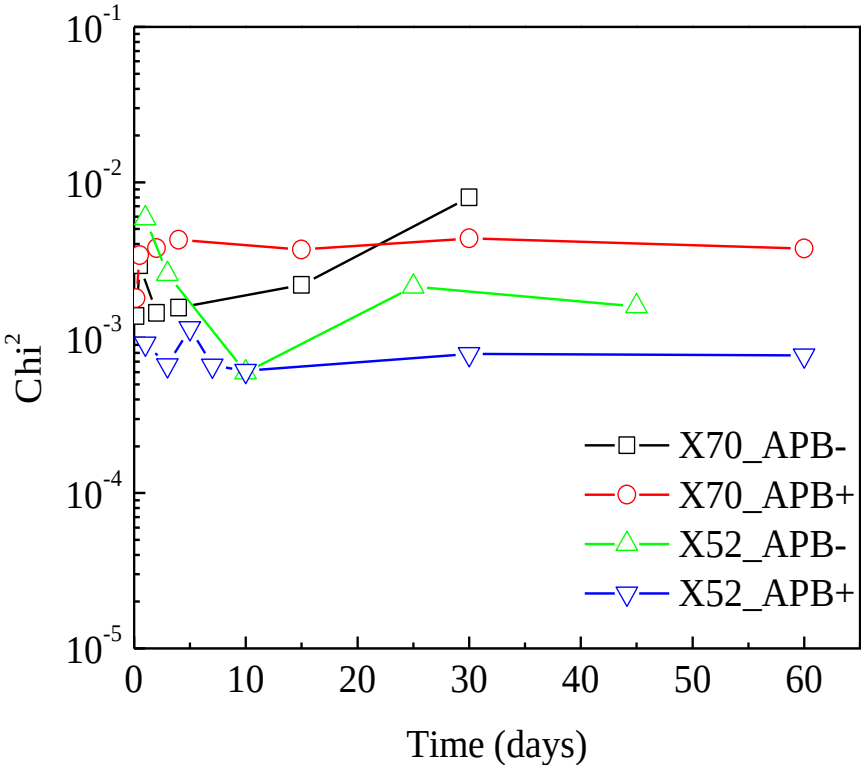

(b)

Figure 4.7 (a) Representation of the Randle equivalent circuit model (b) Goodness of fit of the applied equivalent circuit models to the experimental electrochemical impedance data from the *Acetobacter aceti* tests

When fitting experimental EIS data to equivalent circuit models, it is important to record and show a quantitative measure of quality of fit. This is achieved with the chi-squared distribution (Chi^2). The Chi^2 gives a quantitative indication of the "goodness of fit" of an experimental distribution to a theoretical one. In this case, the experimental distributions are the recorded EIS data and the theoretical distributions are characteristic of the applied equivalent circuit model.

The data presented in Figure 4.7 (b) demonstrate the quality of fit achieved when data recorded from the four corrosion systems during the tests was modeled using the Randles Circuit shown in Figure 4.7 (a). As seen above, Chi^2 values generally remain within 10^{-2} to 10^{-3}, indicating a reasonable fit. Consistent fitting quality over time suggests that the selected equivalent circuit model is appropriate for the entire testing duration.

Corrosion parameters extracted from EIS modeling of the four tests cells are depicted in Figure 4.8. These parameters include the CTR given as $R_{\text{charge transfer}}$, solution resistance given as R_{solution}, and the DLC described by $C_{\text{double layer}}$ and $\eta_{\text{double layer}}$ in Figure 4.8 (a), (b), (c) and (d), respectively. The legend in the lower-right corner of the Figure applies to all four graphs.

The CTR is shown in Figure 4.8 (a). Initially, there appears to be significant variability in the extracted value. The variability is greatest for the inoculated cells. This variability may be due to transient processes involving microbial metabolism and colonization. The most significant finding is that there is no significant difference in CTR between the inoculated and control cells. This finding indicates that general corrosion rates are not measurably accelerated due to the presence of acetic APB despite the acidity of the inoculated systems.

Solution resistance is shown in Figure 4.8 (b). It can be observed that for all four corrosion cells, the solution resistance is one the order of 10^1 ohms*cm^2. The two inoculated corrosion cells, given as "X52_APB+" and "X70_APB+," show a slight decrease in resistance. This decrease is likely due to the production of acetic acid and the resulting increase in acidity. The control cells, given as "X52_APB-" and "X70_APB-," show more erratic changes in solution resistance but contrast with the inoculated cells in that over the course of the tests an overall increase in solution resistance is observed. While the reason for the erratic increase in solution

resistance is not readily apparent, the controls suggest that the decrease in solution resistance observed in the inoculated cells is due to the presence of the acetic APB.
The DLC is given in Figure 4.8 (c). A clear difference in behavior can be observed for the inoculated cells compared to the control cells. The DLC clearly decreases in the case of the inoculated systems and increases in the case of the control systems. Eta values [Figure 4.8 (d)] for the tests can be seen to be relatively lower for the "X70" tests and relatively higher for the "X52" tests. Decreasing eta values can sometimes be attributed to increasing surface irregularity or pitting.

Linepipe Steels Exposed to SRB with Ethanol

Two experiments were conducted with API X52 steel working electrodes; a positive test inoculated with the SRB culture and a negative control test assembled according to the same procedure but without the introduction of the SRB culture. Two experiments were also conducted with API X70 steel working electrodes; a positive test inoculated with the SRB culture and a negative control test assembled according to the same procedure but without the introduction of the SRB culture. The corrosion study, consisting of four experiments, was performed to evaluate the influence of the isolated SRB cultures containing the species grouping with *Clostridium sp.* and *Desulfosporosinus sp.* on corrosion of two linepipe steels while consuming ethanol as a carbon source.

The OCP, measured for the four experiments, is presented in

Figure 4.9 (a). The Figure shows that OCP for the inoculated test cells followed very similar trends. Both potentials increased for the first 24 hrs, decreased from around 24 hours to around 48 hours, and then increased dramatically for the following two to four days. The API X70 inoculated test initially ennobled at a greater rate than the API X52 inoculated test, however, by the end of the testing duration, both were approximately -620 mV verses SCE. The OCP values for the negative controls remained around -680 mV verses SCE for the API X70 test and around -700 mV verses SCE for the API X52 test.

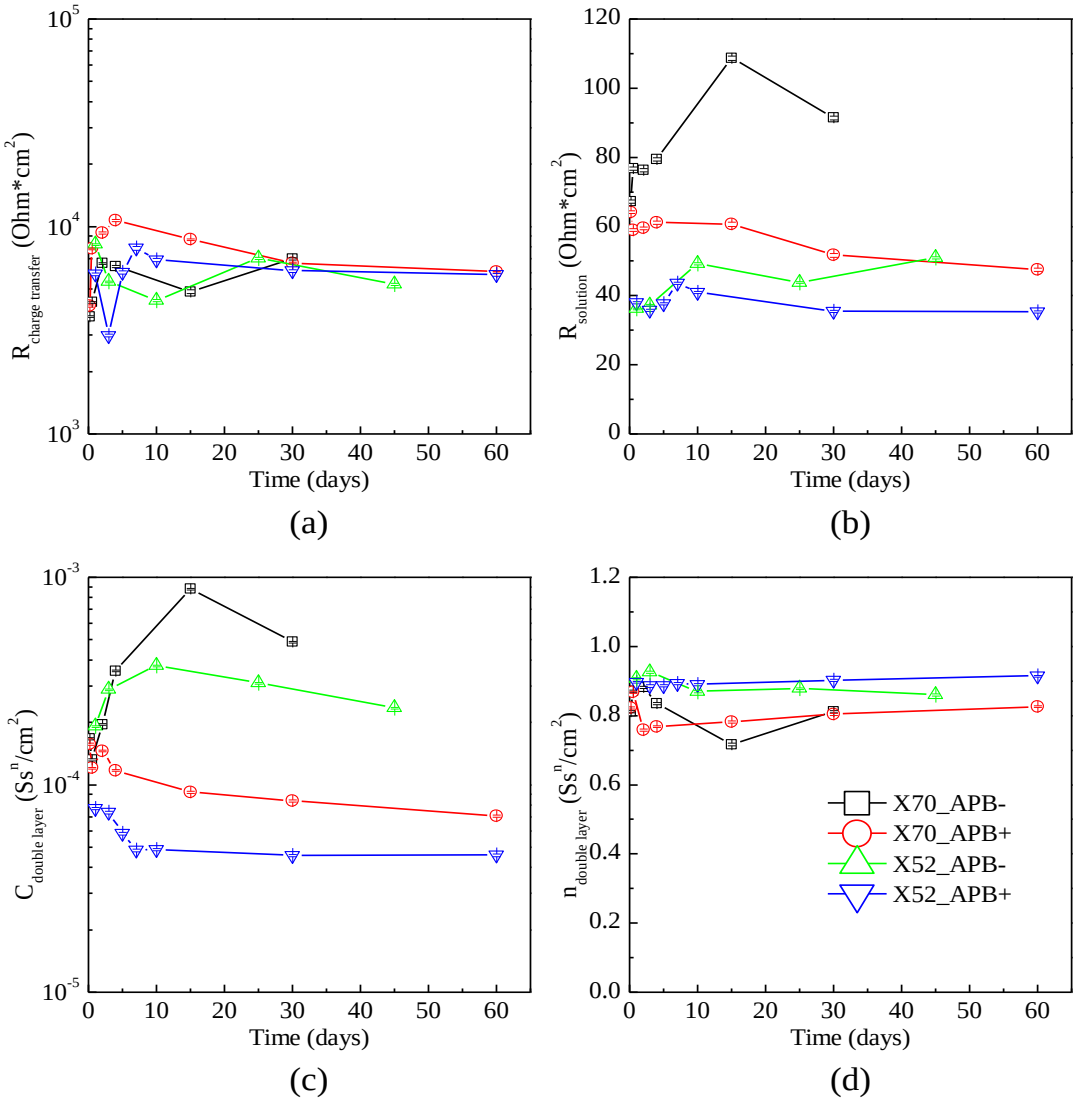

Figure 4.8 Corrosion parameters for API X52 and X70 steels immersed in modified growth media with five vol. pct. ethanol and inoculated with *Acetobacter aceti* showing (a) charge-transfer resistance, (b) solution resistance, (c) double-layer capacitance, and (d) constant phase element exponent, **η**

Planktonic *Desulfosporosinus sp.* cell densities were also recorded for the four experiments and presented in

Figure 4.9 (b). Exponential bacterial growth occurred for the first day, however, planktonic bacterial levels quickly declined and were lower than initial levels by 35 hours after immersion. The exponential growth phase for the planktonic bacteria can be observed to coincide generally with the initial ennoblement of the electrodes.

EIS data, presented as nyquist, modulus, high-frequency nyquist, and phase plots, are displayed in Figure 4.10 (a), (b), (c) and (d), respectively. These data are acquired from the API X52 corrosion cell inoculated with SRB at 0.5, 24, 32, 40, 48, 72, 96, 120, and 144 hours after immersion. The nyquist and modulus plots exhibit a significant decrease in the low-frequency limit of the impedance for the system. This decrease indicates dramatically increasing corrosion rates. The most obvious behavior exhibited by the phase plot is the dramatic increase in DLC indicated by the shift in the primary peak from around 10 Hz to around 10^{-2} Hz. Less apparent, but discernable, is the inflection in the phase curve around 10 Hz, which is most notable at 48 and 72 hours after immersion. This inflection corresponds to curvature in the high frequency nyquist plot,

also most prominent at 48 and 72 hours after immersion. This evidence of a second time-constant in the data suggests the presence of an additional layer or film near the metal-solution interface.

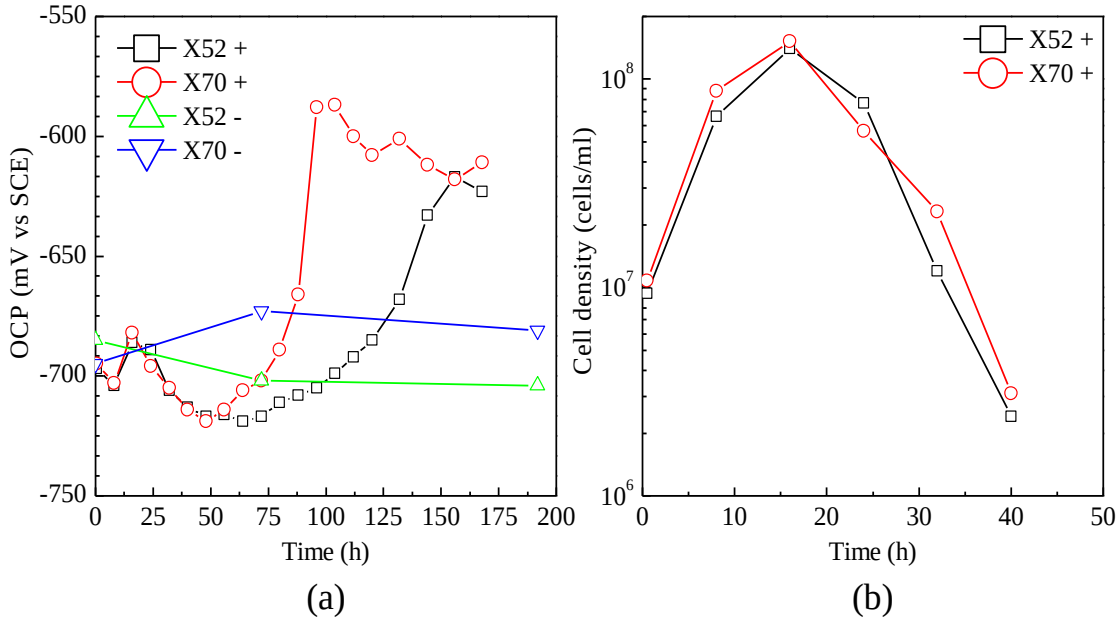

Figure 4.9 Experimental data from the sulfate-reducing consortium with two vol. pct. ethanol tests series including (a) open circuit potential and (b) cell counts

The behavior observed in the data gives justification for the application of equivalent circuit models incorporating two time-constants rather than the lone time-constant in the Randles Circuit. Other necessary justification for adding additional time-constants include expectation of film formation based on current scientific knowledge of the system and confirmation of the development of a film via microscopic investigation.

EIS data, presented as nyquist, modulus, high-frequency nyquist, and phase plots, are displayed in Figure 4.11 (a), (b), (c) and (d), respectively. These data were acquired from the API X70 corrosion cell inoculated with SRB at 0.5, 16, 24, 32, 40, 48, 72, 96, 120, and 144 hours after immersion. It is apparent from both the nyquist and modulus plots that there is a significant decrease in the low-frequency limit of the impedance for the system although it is not as pronounced as in the case of the inoculated API X52 system. While this decrease indicates increasing corrosion rates, it suggests that general corrosion is not as severe for the API X70 steel as for the API X52 steel in this system. As observed for the API X52 steel, a dramatic increase in DLC is indicated by the shift in the primary peak in the phase plot from around 10 Hz to around 10^{-2} Hz. The absence of an inflection in the phase curve around 10 Hz should be noted for the API X70 data. Correspondingly, the high frequency nyquist plot shows linearity. The absence of the appearance of a second time-constant in the data suggests that a Randles Circuit, with one tim-constant is sufficient to model the data. In this case, justification for the application of equivalent circuit models incorporating multiple time-constants is not found.

EIS data, presented as nyquist, modulus, and phase plots, are displayed in Figure 4.12 (a), (b), and (c), respectively. These data were acquired from the sterile API X52 corrosion cell at 0, 72, and 192 hours after immersion. In stark contrast to the impedance data for the inoculated cells, very little change is observed for any of the plots over the nearly 200-hour testing duration. The low-frequency limit of the impedance remains very constant at around 12,000 ohms*cm2. This value corresponds to a relatively low corrosion rate and provides a reference with which to compare the inoculated API X52 test. The DLC can be observed to increase slightly with the center of the phase peak shifting from around 10 Hz to around 1 Hz. This increase is much more modest than was demonstrated for the inoculated API X52 corrosion cell. A second time-constant is not observed in the phase plot. The high frequency nyquist is not separately plotted because an additional high frequency time-constant is not anticipated.

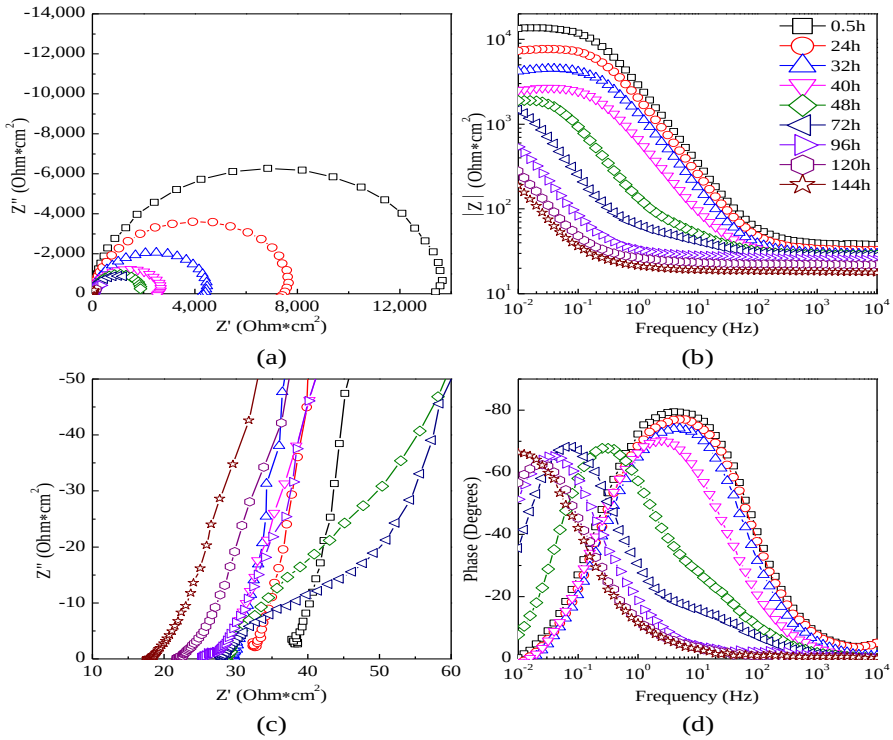

Figure 4.10 Electrochemical impedance data for API X52 steel immersed in modified Postage B growth media with 2 vol. pct. ethanol and inoculated with SRB showing (a) nyquist, (b) modulus, and (c) high frequency modulus and (d) phase plots

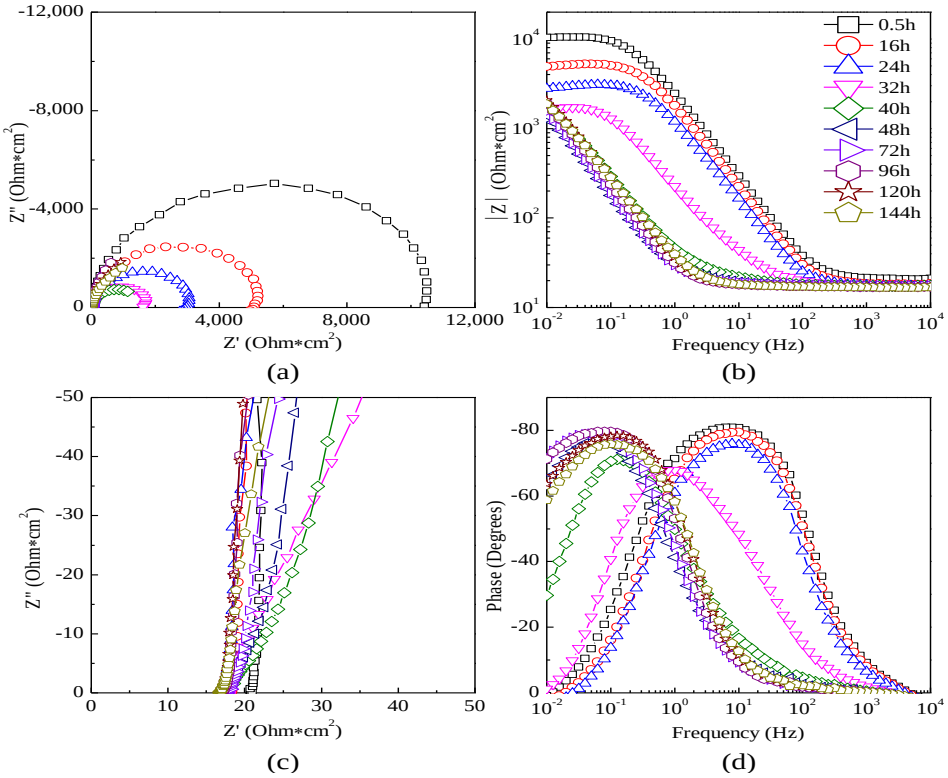

Figure 4.11 Electrochemical Impedance data for API X70 steel immersed in modified Postage B growth media with 2 vol. pct. ethanol and inoculated with SRB showing (a) nyquist, (b) modulus, and (c) high frequency modulus and (d) phase plots

EIS data, presented as nyquist, modulus, and phase plots, are displayed in Figure 4.13 (a), (b), and (c), respectively. These data were acquired from the sterile API X70 corrosion cell at 0, 72, and 192 hours after immersion. Very little change is observed for any of the plots over the nearly 200-hour testing duration. The low-frequency limit of the impedance averages around 15,000 ohms*cm2. The low-frequency limit of the impedance data increases slightly throughout the test indicating slight passivation. This low corrosion rate, as measured for the API X70 negative control, provides a reference with which to compare to the inoculated API X70 test. The DLC can be observed to increase slightly with the center of the phase peak shifting from around 10 Hz to around 1 Hz. This increase is again a much more modest increase than was demonstrated for the inoculated API X70 corrosion cell. A second time-constant is not observed in the phase plot. The high frequency nyquist is not separately plotted because an additional high frequency time-constant is not anticipated.

The raw impedance data from the four experiments were modeled using one or more of several equivalent circuits models based on the number of time-constants observed in the EIS plots in Figure 4.10 through Figure 4.13. Several equivalent circuit models are given in Figure 4.14(a-c). The first, labeled "Ran", is the Randles Circuit described previously in this Chapter and which is appropriate for impedance spectra displaying one time-constant. As Figure 4.11 through Figure 4.13 exhibit one time-constant, the data from these spectra was modeled only with the Randles Circuit. The circuit model labeled "Ran_RC" is commonly used for a porous coating or film on a metal surface. This model incorporates two time-constants that correspond to the two CPE elements in the model. One CPE corresponds to the capacitance of the coating or film while the other CPE corresponds to the DLC. The third circuit model, labeled "RC-RC" incorporates two time-constants that correspond to the two CPE elements in the model. Again, one CPE corresponds to the capacitance of the coating or film while the other CPE corresponds to the DLC. The spectra in Figure 4.10, showing two time-constants, have been modeled with all three equivalent circuit models.

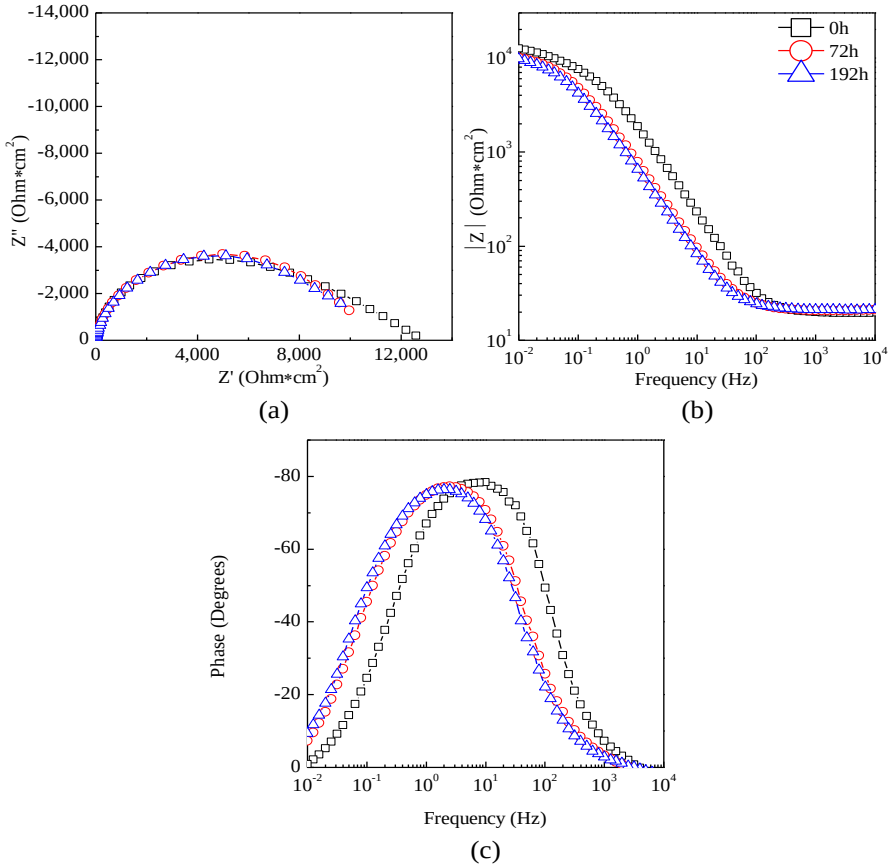

Figure 4.12 Electrochemical impedance data for API X52 steel immersed in sterile modified Postage B growth media with two vol. pct. ethanol showing (a) nyquist, (b) modulus, and (c) phase plots

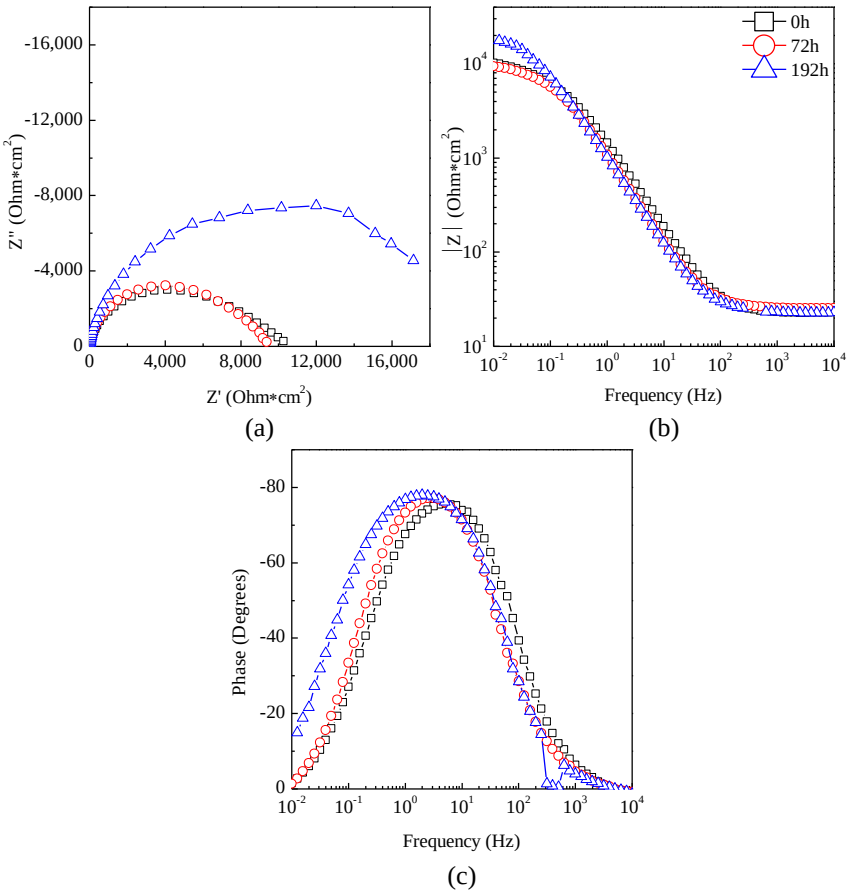

Figure 4.13 Electrochemical impedance data for API X70 steel immersed in sterile modified Postage B growth media with two vol. pct. ethanol showing (a) nyquist, (b) modulus, and (c) phase plots

The two time-constant impedance spectra were modeled with two different models to demonstrate the effect of applying different circuit models on the extracted corrosion parameters. The selection of the appropriate circuit model for a given situation can be subjective. A common criticism of EIS analysis is to the choice of the equivalent circuit model applied. The intent of applying multiple circuit models is to increase confidence in trends in the extracted corrosion parameters that persist, regardless of the equivalent circuit model applied.
Goodness of fit, plotted in Figure 4.14(d), demonstrates fitting quality for models applied to all four experiments. The plot labels in the legend "X52_EtOH+_Ran", "X52_EtOH+_RC-RC", and "X52_EtOH+_RC_Ran" refer to the inoculated API X52 impedance data modeled with the "Ran", "RC-RC", and "Ran_RC" circuit models, respectively. The plot labels "X52_EtOH-_Ran", "X70_EtOH+_Ran", and "X70_EtOH-_Ran" refer to the API X52 negative control, the API X70 inoculated, and the API X70 negative control, respectively. All three are modeled only with the Randles circuit.
It can be observed that the Chi^2 values generally remain on the order of 10^{-2} to 10^{-3}. An exception to this is the behavior is exhibited by the "X52_EtOH+_Ran" plot. The Chi^2 value diverges from the group to as high as 10^{-1}. This divergence occurs around 48 hours after immersion coinciding with the observation of the second time-constant in the experimental impedance spectra. From this time until the end of the experiment, the goodness of fit is superior for the circuit models incorporating two time-constants, indicating the greater appropriateness of applying these models. The best fit for the API X52 inoculated impedance data is given by the "RC-RC" circuit, suggesting a high degree of confidence.

Corrosion parameters extracted from modeling the impedance spectra from the four cells are displayed in

Figure 4.15 and Figure 4.16. Parameters describing the metal-solution interface include the CTR given as $R_{charge\ transfer}$, solution resistance given as $R_{solution}$, and the DLC described by $C_{double\ layer}$ and $\eta_{double\ layer}$ shown in

Figure 4.15 (a), (b), (c) and (d), respectively. Parameters describing the iron sulfide film include the iron sulfide film resistance given as $R_{FeS\ film}$ and the iron sulfide film capacitance described by $C_{FeS\ film}$ and $\eta_{FeS\ film}$ shown in Figure 4.16 (a), (b), and (c), respectively. The legend in the lower-right corner of the Figure applies to all four graphs.

The CTR is given in

Figure 4.15 (a). CTR decreases significantly in the case of both inoculated steels for the first 2 days after immersion. These values diverge around day 2, with the API X70 steel repassivating, while the corrosion rate for the API X52 steel continues to increase. This increase in corrosion rate is most pronounced for the RC-RC data, which gives the best fit. The CTR for both negative control experiments is observed to stay relatively constant compared to the larger changes observed in the inoculated experiments.

Solution resistance is given in

Figure 4.15 (b). Solution resistance for the four tests ranged from around 15 to 40 ohms*cm^2. Solution resistance values for the inoculated API X70 steel experiment and both negative control experiments remained around 15 to 25 ohms*cm2 and exhibit little change over the duration of the test. In contrast, the solution resistance for the API X52 steel inoculated cell begins at around 40 ohms*cm^2 and decreases to about 17 ohms*cm^2 by the end of the test.

The DLC and corresponding eta value is given in

Figure 4.15 (c) and (d), respectively. DLC is observed to increase several orders of magnitude for both inoculated experiments. The greatest increase is observed for the inoculated API X52 experiment. The increase in DLC appears to coincide with and be indirectly proportional to the decrease in CTR. Little distinction can be made between the eta values for the four tests regardless of circuit model applied.

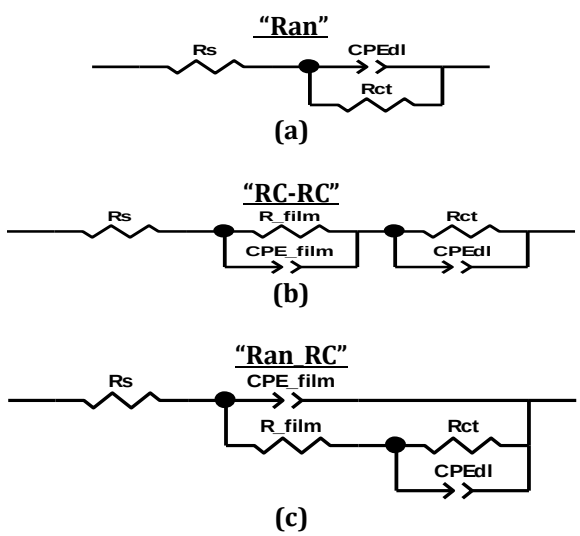

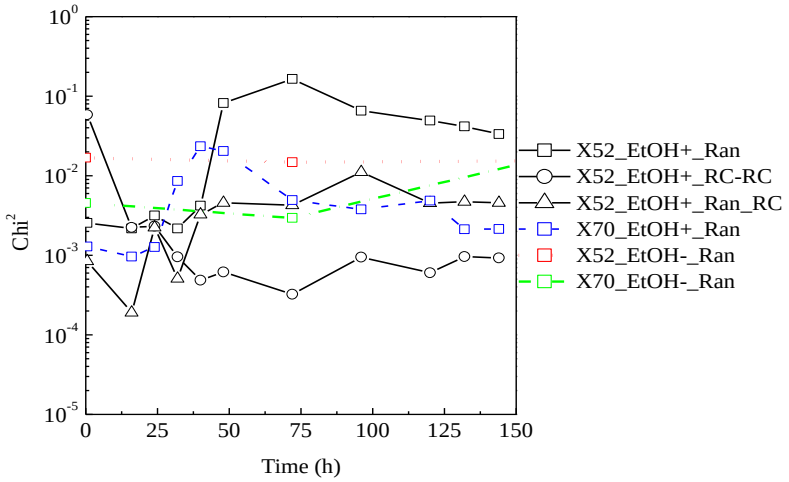

(d)

Figure 4.14 (a) Representations of the equivalent circuit models applied (b) Goodness of fit of the applied equivalent circuit models to the experimental electrochemical impedance data from the SRB with two vol. pct. ethanol tests.

The parameters given in Figure 4.16 describe circuit elements that correspond to the additional time-constant in the inoculated API X52 data. Given the nature of the system, the reasonable assumption is made that the second time-constant corresponds to the formation of an iron sulfide on the surface of the metal. Consistent with the inspection of the impedance spectra in Figure 4.10, the resistance, and therefore presence of the iron-sulfide film, is most pronounced around 48 to 72 hours after immersion. The capacitance of the film is observed to increase throughout the duration of the experiment. This increase may be due to increasing porosity. Mechanical strain due to film growth and diffusion of corrosion reactants and products has been suggested to compromise iron sulfide film integrity (Sun and Nesic 2009). Because general corrosion rates increase for most of the testing duration and then remain high, it can be assumed that the film is not very protective. Eta values for the iron-sulfide film are significantly closer to 1 when the data is fit using the "Ran_RC" model than when using the "RC-RC" model, suggesting that the configuration of the "Ran_RC" circuit model provides a more ideal representation of circuit elements.

Linepipe Steels Exposed to SRB with Acetic Acid

Two experiments were conducted with API X52 steel working electrodes; a positive test inoculated with the SRB culture and a negative control test assembled according to the same procedure but without the introduction of the SRB culture. Two experiments were also conducted with API X70 steel working electrodes; a positive test inoculated with the SRB culture and a negative control test assembled according to the same procedure but without the introduction of the SRB culture. A corrosion study consisting of the four experiments was performed to evaluate the influence of the isolated SRB cultures containing the species grouping with *Clostridium sp.* and *Desulfosporosinus sp.* on corrosion of two linepipe steels while consuming acetic acid as a carbon source.

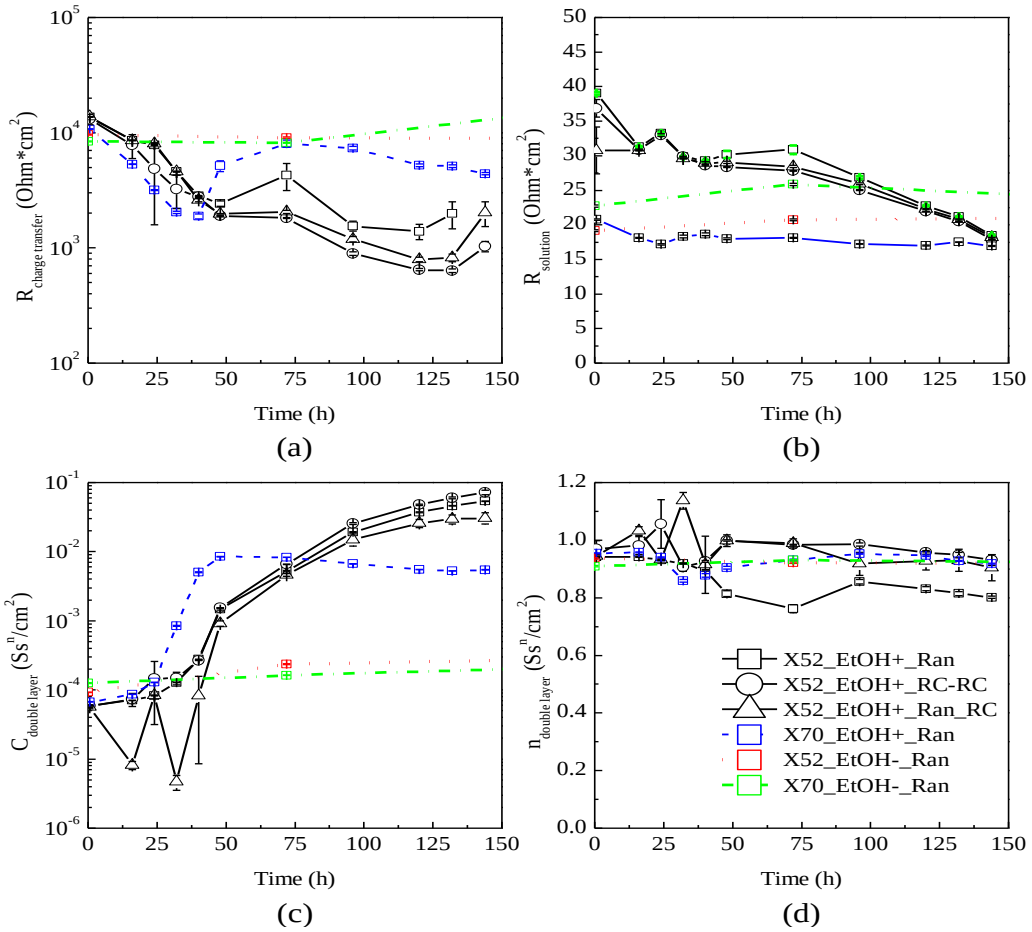

Figure 4.15 Corrosion parameters for API X52 and X70 steels immersed in modified Postage B growth media with two vol. pct. ethanol and inoculated with SRB showing (a) charge-transfer resistance, (b) solution resistance, (c), double-layer capacitance, and (d) constant phase element exponent, **η**

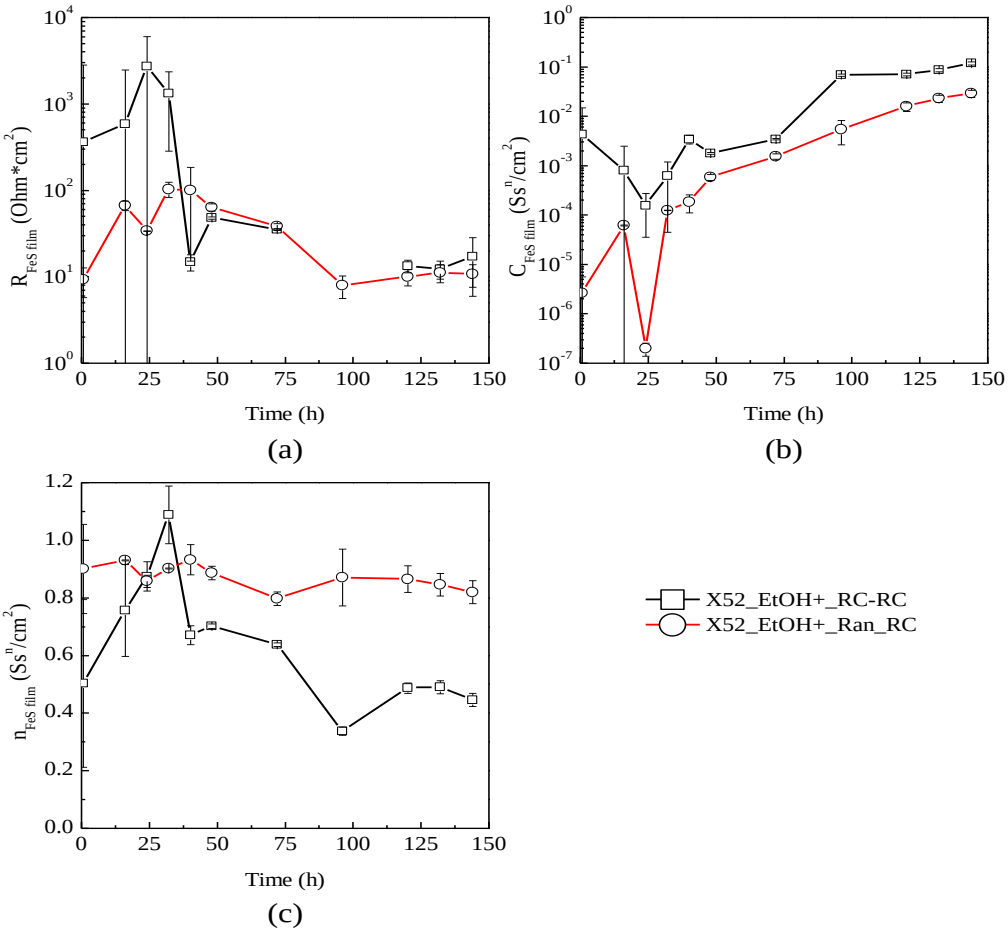

Figure 4.16 Corrosion parameters for API X52 and X70 steels immersed in modified Postage B growth media with two vol. pct. ethanol and inoculated with SRB showing (a) iron-sulfide film resistance, (b) iron-sulfide film capacitance, and (c) constant phase element exponent, **η**

The PR measurements taken from the four cells are presented in

Figure 4.17 (a). Corrosion rates (CR) calculated from the PR data are presented in

Figure 4.17 (b). It is evident from the PR and CR graphs in

Figure 4.17 that both inoculated cells experienced an initial increase in corrosion rate for the first 2 days after immersion. This coincides with the initial decrease in the OCP. For the next day, the increase in CR for the cells seems to arrest and even begins to reverse. At around three days after immersion, however, the CRs for both cells again begin to increase although the rate of increase slows for both cells. The inoculated API X70 steel electrode exhibits greater resistance to corrosion than the API X52 steel electrode. For the last four days of the test, the PR for the API X52 steel cell remains around 600 ohms*cm2 corresponding to a CR of around 17 mills per year (mpy) and the PR for the API X70 steel cell remains around 2000 ohms*cm2 corresponding to a CR of around 5 mpy.

The OCP, measured at regular intervals during all four experiments, is presented in

Figure 4.17 (c). The OCP for the inoculated experiments followed similar trends. Both potentials initially decreased from around -680 mV versus SCE to around -735 mV versus SCE by 56 hours after immersion. The OCP for both inoculated cells subsequently increased dramatically from 56 hours after immersion to 96 hours after immersion. The OCP for the inoculated API X52 cell increased to around -660 mV versus SCE. The OCP for the inoculated API X70 cell increased to around -630 mV versus SCE. The OCP for both inoculated cells

remained ennobled for the duration of the tests. The OCP values for the negative controls remained around -700 mV verses SCE for the API X70 test and around -690 mV verses SCE for the API X52 test.

EIS data, presented as nyquist, modulus, high-frequency nyquist, and phase plots, are displayed in Figure 4.18 (a), (b), (c) and (d), respectively. These data were acquired from the API X52 corrosion cell inoculated with SRB at 0, 24, 32, 40, 48, 56, 64, 72, 120, and 192 hours after immersion. It is apparent from both the nyquist and modulus plots that there is a significant decrease in the low-frequency limit of the impedance for the system. This observation fits well with the dramatically increasing corrosion rates observed in the PR data. The most obvious behavior exhibited by the phase plot is the dramatic increase in DLC indicated by the shift in the center of the primary peak from around 10 Hz to around 10^{-2} Hz. Less apparent, but able to be discerned, is the inflection in the phase curve around 10 Hz, which is most notable at 120 and 192 hours after immersion. This corresponds to a curvature in the high frequency nyquist plots, also most prominent at 120 and 192 hours after immersion. This evidence of a second time-constant in the data suggests the presence of an additional layer or film near the metal-solution interface. The behavior observed in the data gives justification for the application of equivalent circuit models incorporating two time-constants rather than the lone time-constant in the Randles Circuit.

EIS data, presented as nyquist, modulus, high-frequency nyquist, and phase plots, are displayed in Figure 4.19 (a), (b), (c) and (d), respectively. These data were acquired from the API X70 corrosion cell inoculated with SRB at 0, 24, 32, 40, 48, 56, 120, and 192 hours after immersion. It is apparent from both the nyquist and modulus plots that there is a significant decrease in the low-frequency limit of the impedance for the system although it is not as pronounced as in the case of the inoculated API X52 system. While this decrease indicates increasing corrosion rates, it suggests that general corrosion is not as severe for the API X70 steel than as for the API X52 steel in this system. As was observed for the API X52 steel, a dramatic increase in DLC is indicated by the shift in the primary peak in the phase plot from around 10 Hz to around 10^{-2} Hz. Slight inflection can be observed in the phase curve. Some degree of curvature is also observed in the high frequency nyquist plot. This evidence of a second time-constant in the data suggests the presence of an additional layer or film near the metal-solution interface. The behavior observed in the data gives justification for the application of equivalent circuit models incorporating two time-constants rather than the lone time-constant in the Randles Circuit

EIS data, presented as nyquist, modulus, and phase plots, are displayed in Figure 4.20 (a), (b), and (c), respectively. These data were acquired from the sterile API X52 corrosion cell inoculated with SRB at 0, 48, 96, 144, and 192 hours after immersion. In stark contrast to the impedance data for the inoculated cell, very little change is observed for any of the plots over the nearly 200-hour testing duration. The low-frequency limit of the impedance remains very constant at around 11,000 ohms*cm2. This value corresponds to a relatively low corrosion rate and provides a reference with which to compare the inoculated API X52 experiment. The DLC remains nearly constant with the center of the phase peaking around 3 Hz. Some irregularity exists in the degree of depression of the semi-circle observed in the nyquist plot. This irregularity may be due to modest changes in the configuration of species near the metal-solution interface. A second time-constant is not observed in the phase plot. The high frequency nyquist is not separately plotted, as an additional high frequency time-constant is not anticipated.

EIS data, presented as nyquist, modulus, and phase plots, are displayed in

Figure 4.21 (a), (b), and (c), respectively. These data were acquired from the sterile API X70 corrosion cell at 0, 48, 96, 144, and 192 hours after immersion. Once again, relative to the API X70 inoculated cell, very little change is observed for any of the plots over the nearly 200-hour testing duration. The low-frequency limit of the impedance generally remains around 10,000 ohms*cm2. This low corrosion rate measured for the API X70 negative control provides a reference with which to compare to the inoculated API X70 test. The DLC can be observed to increase slightly, with the center of the phase peak shifting from around 10 Hz to around 1 Hz. This is again a much more modest increase than demonstrated for the inoculated API X70 corrosion cell. A second time-constant is not observed in the phase plot. The high frequency nyquist is not separately plotted, as an additional high frequency time-constant is not anticipated.

The raw impedance data from the four experiments was modeled using one or more of several

circuits models based on the number of time-constants observed in the EIS plots in Figure 4.18 through

Figure 4.21. Several equivalent circuit models are given in Figure 4.22 (a-c). As Figure 4.20 and

Figure 4.21 exhibit one time-constant, the data from these spectra was modeled only with the Randles Circuit. The spectra in Figure 4.18 (from the inoculated API X52 experiment) clearly shows two time-constants and was therefore modeled with circuit model "Ran" as well as "Ran_RC". A solution could not be found by the modeling software to fit the "RC-RC" circuit model to the experimental data for the inoculated API X52 spectra at several intervals and as a result, it was not applied to this data. The spectra in Figure 4.19 from the inoculated API X70 experiment, which also indicated the presence of a second time-constant, was modeled with circuit models "Ran" as well "RC-RC".

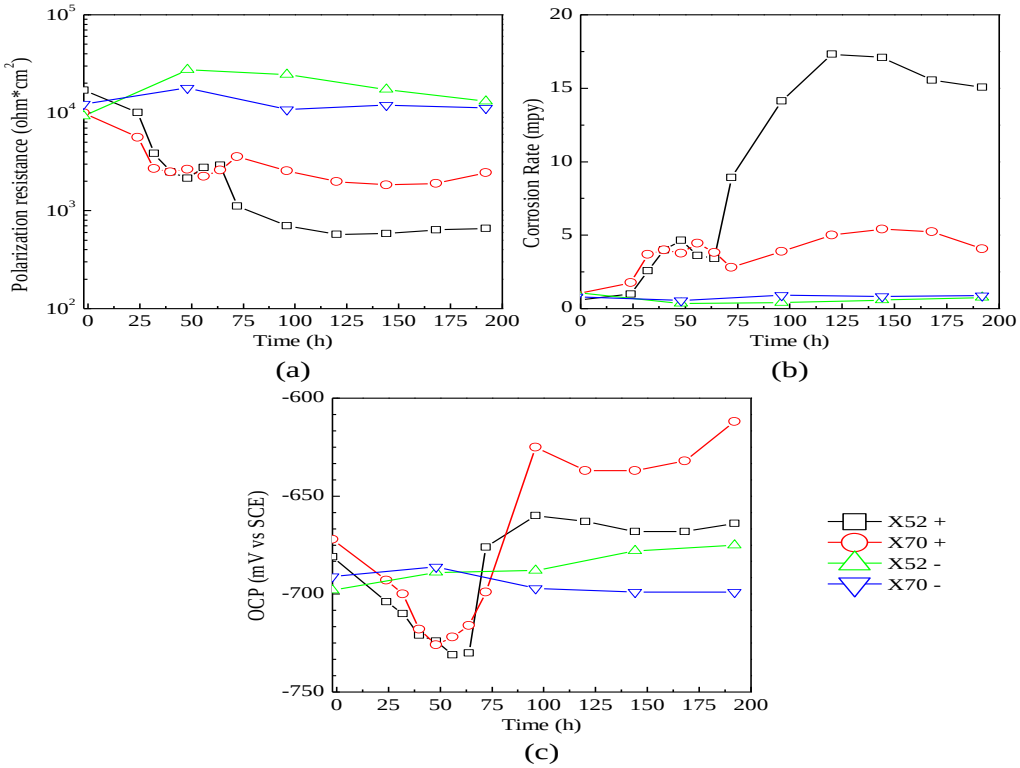

Figure 4.17 Experimental data from the SRB with one gram per liter acetic acid tests series including (a) polarization resistance, (b) corrosion rate, and (c) open circuit potential

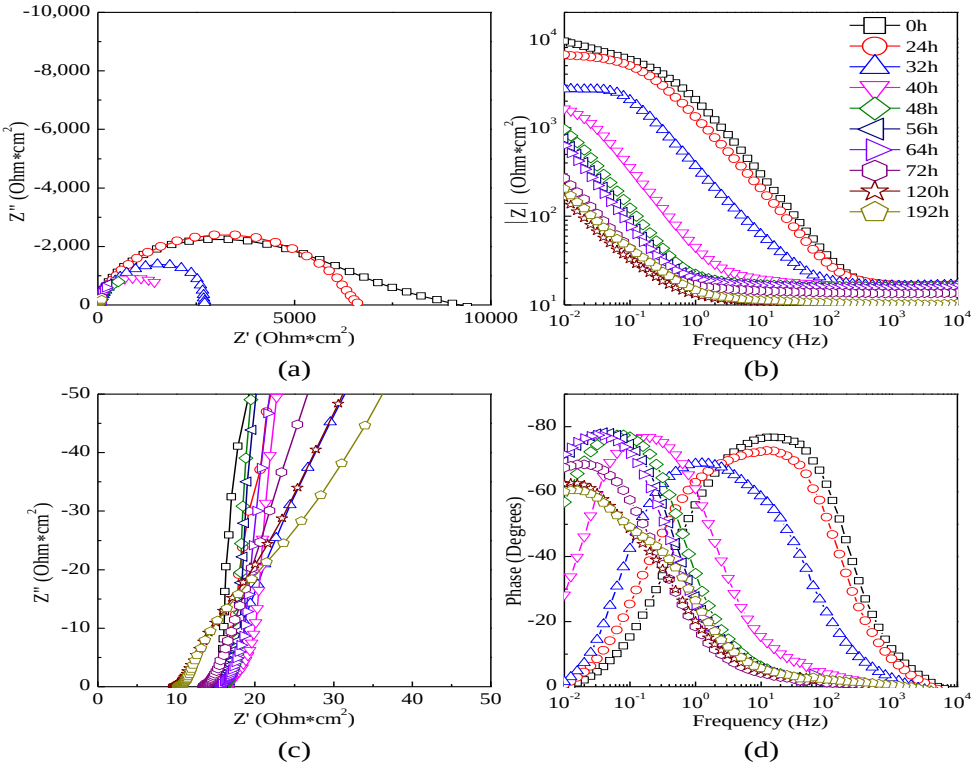

Figure 4.18 Electrochemical impedance data for API X52 steel immersed in modified Postage B growth media with one gram per liter acetic acid and inoculated with SRB showing (a) nyquist, (b) modulus, and (c) high frequency modulus and (d) phase plots

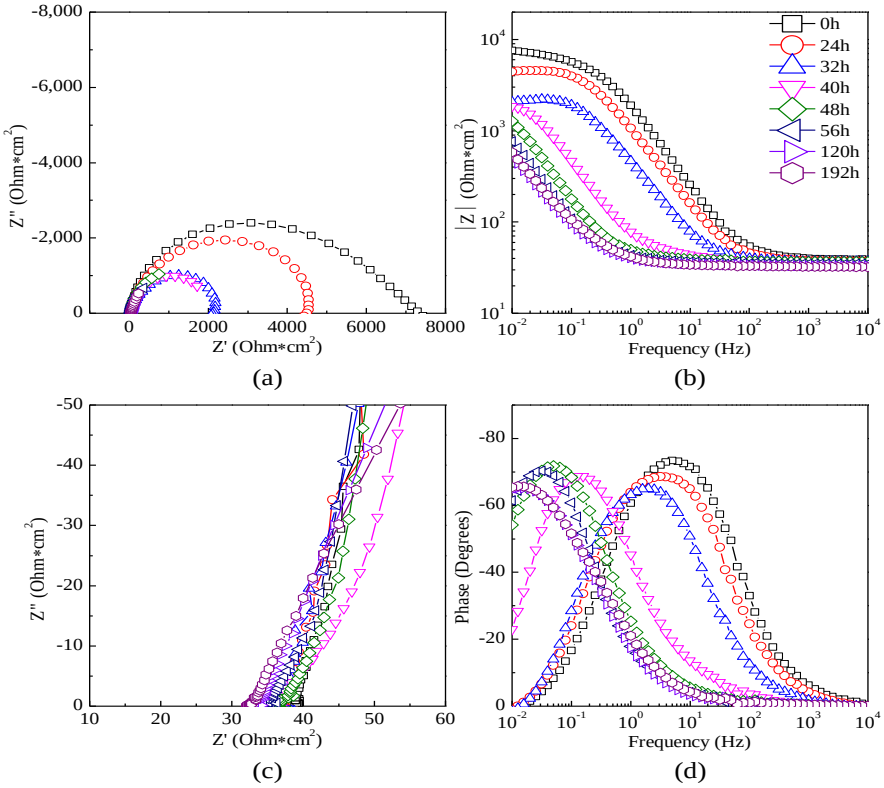

Figure 4.19 Electrochemical impedance data for API X70 steel immersed in modified Postage B growth media with one gram per liter acetic acid and inoculated with SRB showing (a) nyquist, (b) modulus, and (c) high frequency modulus and (d) phase plots

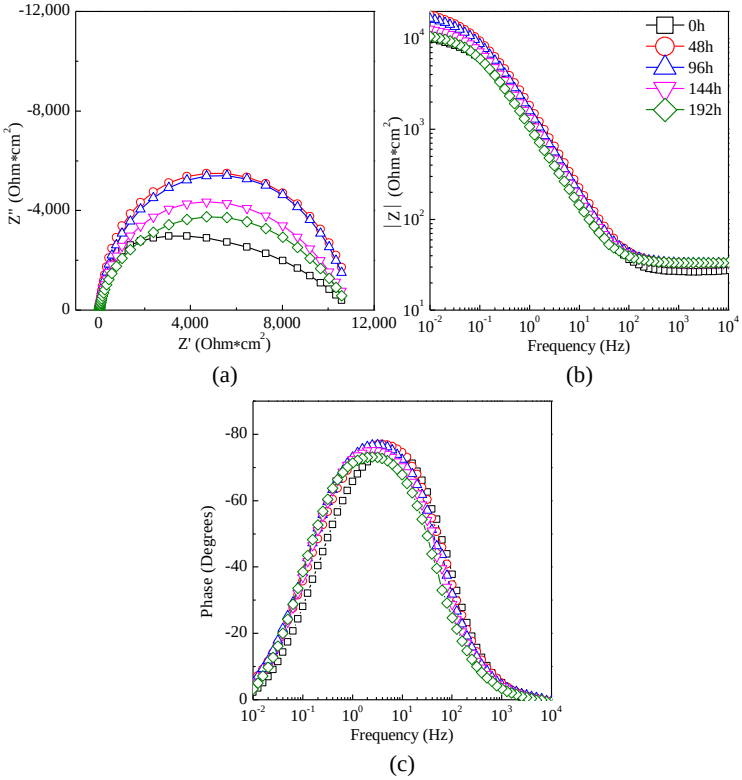

Figure 4.20 Experimental impedance data for API X52 steel immersed in sterile modified Postage B growth media with one gram per liter acetic acid (a) nyquist, (b) modulus, and (c) phase plots

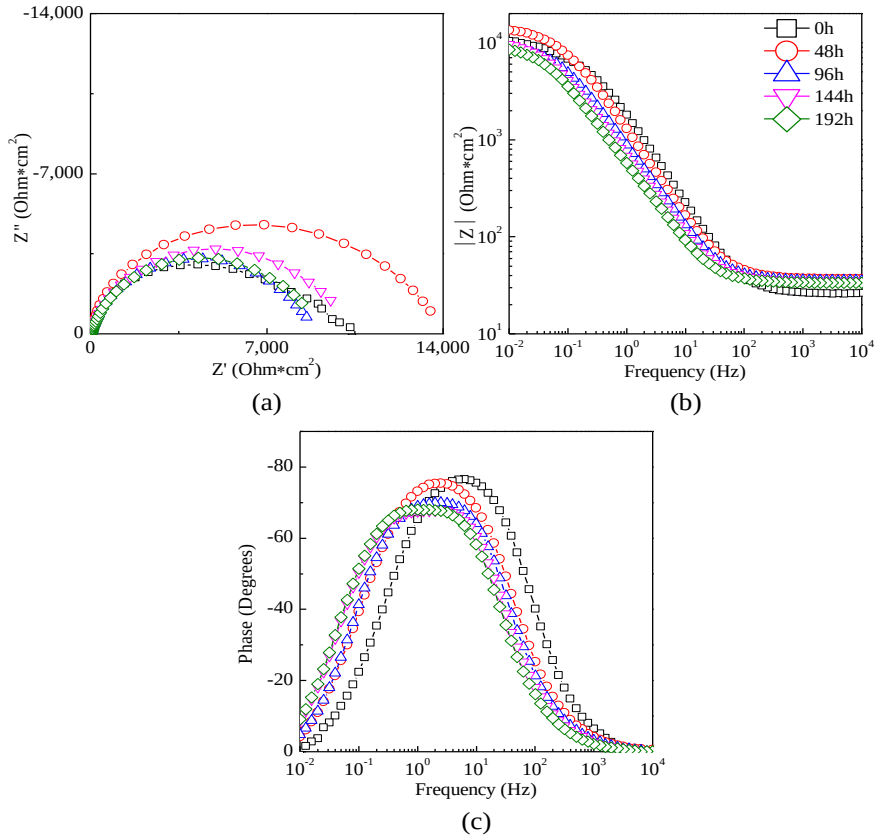

Figure 4.21 Experimental impedance data for API X70 steel immersed in sterile modified Postage B growth media with one gram per liter acetic acid (a) nyquist, (b) modulus, and (c) phase plots

Goodness of fit, plotted in Figure 4.22 (d), demonstrates fitting quality for models applied to all four experiments. The plot labels in the legend "X52_EtOH+_Ran" and "X52_EtOH+_RC_Ran" refer to the inoculated API X52 impedance data modeled with the "Ran" and "Ran_RC" circuit models, respectively. The plot labels in the legend "X70_EtOH+_Ran" and "X70_EtOH+_RC-RC" refer to the inoculated API X52 impedance data modeled with the "Ran" and "RC-RC" circuit models, respectively. The plot labels "X52_EtOH-_Ran" and "X70_EtOH-_Ran" refer to the API X52 negative control and the API X70 negative control, respectively. Both data are only modeled with the Randles circuit.

It can be observed that the Chi^2 values range from 10^{-2} to 10^{-4}. In the case of the data collected from the inoculated API X52 experiment, a better fit was achieved by the two time-constant model compared with the Randles Circuit. This difference in quality of fit becomes very pronounced at 120 and 192 hours after immersion. This behavior is with consistent with observations of a second time constant in Figure 4.18. A far better fit is achieved by the two time-constant model for the inoculated API X70 experimental data from 32 hours after immersion until the end of the testing duration. These observations about fitting quality for both inoculated experiments reinforce the validity of applying two time-constant circuit models.

Corrosion parameters extracted from modeling the impedance spectra from the four cells are displayed in Figure 4.23 Figure 4.24. Parameters describing the metal-solution interface include the CTR given as $R_{charge\ transfer}$, solution resistance given as $R_{solution}$, and the DLC described by $C_{double\ layer}$ and $\eta_{double\ layer}$ shown in Figure 4.23 (a), (b), (c) and (d), respectively. Parameters describing the iron sulfide film include the iron sulfide film resistance given as $R_{FeS\ film}$ and the iron sulfide film capacitance described by $C_{FeS\ film}$ and $\eta_{FeSe\ film}$ shown in Figure 4.24 (a), (b), and (c), respectively. The legend in the lower-right corner of the Figure applies to all four graphs.

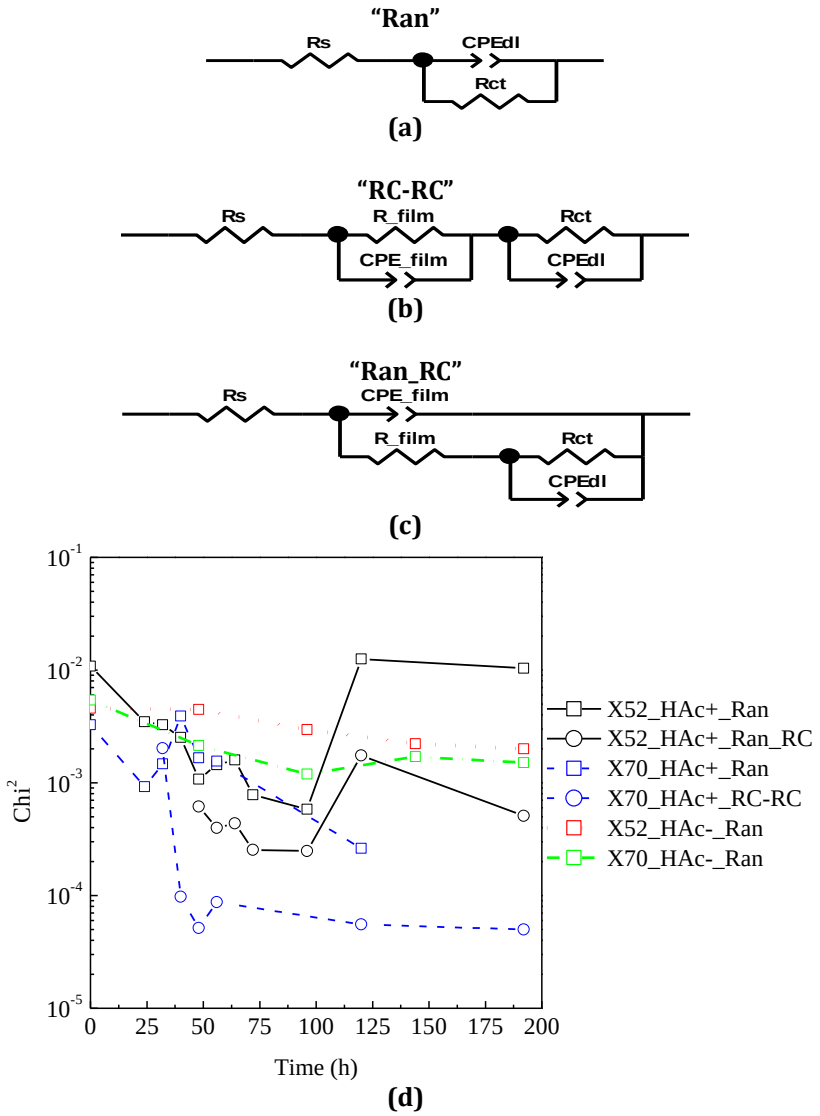

Figure 4.22 (a-c) Representations of applied equivalent circuit models and (d) goodness of fit of applied equivalent circuit models to the experimental electrochemical impedance data from the modified Postgate B growth media with one gram per liter study

The CTR is shown in Figure 4.23 (a). CTR decreases significantly for both inoculated steels for the first 2 days after immersion. The CTR then appears to increase for the next one to two days. The CTR for the inoculated API X52 cell then experiences another decline around 4 days after immersion, diverging from the CTR for the inoculated API 70 cell. At the end of the testing duration, the CTR is around 1000 ohms*cm2 in the case of the inoculated API X52 cell and 3000 ohms*cm2 in the case of the inoculated API X70 cell. The CTR for both negative control experiments is observed to stay relatively constant compared to the larger changes observed in the inoculated experiments.

Solution resistance is displayed in Figure 4.23 (b). Solution resistance for the four tests ranged from around 10 to 40 ohms*cm2. Solution resistance for the inoculated API X52 experiment begins at around 25 ohms*cm2 and then decreases to around 10 ohms*cm2. Solution resistance for the inoculated API X70 experiment begins at around 40 ohms*cm2 and then decreases to around 32 ohms*cm2. The solution resistance for the two negative control cells begins at around 25 ohms*cm2 and then increases to around 32 ohms*cm2. The reason for the variability in these values is not readily apparent but could be due to variations in the bioactivity of the added cultures.

The DLC and corresponding eta is given in Figure 4.23 (c) and (d), respectively. DLC is observed to increase several orders of magnitude for both inoculated experiments. The greatest increase is observed for the inoculated API X52 experiment. The increase in DLC appears to coincide with and be indirectly proportional to the decrease in CTR. Relatively lower eta values for the inoculated API X52 experiment are also indicated.
The parameters given in Figure 4.24 describe circuit elements that correspond to the additional time-constant in the inoculated API X52 data. Given the nature of the system, the reasonable assumption is made that the second time-constant corresponds to the formation of an iron sulfide layer on the surface of the metal. Consistent with the inspection of the impedance spectra in Figure 4.18 Figure 4.19, the resistance, and therefore presence of the iron-sulfide film, is most pronounced around 120 to 192 hours after immersion. The capacitance of the film is observed to increase throughout the duration of the experiment. This increase may be due to increasing porosity as mechanical strain and electrochemical diffusion compromise the film integrity. As general corrosion rates increase for most of the testing duration and then remain high, it can be assumed that the film is not very protective. Eta values for the iron-sulfide film are again significantly closer to one when the data is fit using the "Ran_RC" model than when using the "RC-RC" model. While the models are applied to two different systems, the repeat of this behavior may further suggest that the configuration of the "Ran_RC" circuit model provides a more ideal representation of circuit elements.

Linepipe Steels Exposed to a SRB in Ethanolic and Acetic Environments
To better compare the effects of ethanol and acetic acid on the corrosion of the steels, corrosion parameters have been plotted together for the four previously described SRB inoculated corrosion experiments.

Corrosion parameters extracted from modeling the impedance spectra from the four cells are displayed in

Figure 4.25 and

Figure 4.26. Parameters describing the metal-solution interface include the CTR given as $R_{charge\ transfer}$, solution resistance given as $R_{solution}$, and the DLC described by $C_{double\ layer}$ and $\eta_{double\ layer}$ shown in

Figure 4.25 (a), (b), (c) and (d), respectively. Parameters describing the iron sulfide film include the iron sulfide film resistance given as $R_{FeS\ film}$ and the iron sulfide film capacitance described by $C_{FeS\ film}$ and $\eta_{FeSe\ film}$ shown in

Figure 4.26 (a), (b), and (c), respectively. The legend in the lower-right corner of the Figure applies to all four graphs.

The CTR is shown in

Figure 4.25 (a). CTR significantly decreases for all systems for the first day after immersion. The decrease in CTR is followed by an approximately 3 to 4-day increase in CTR for both API X70 tests. The API X70 and ethanol experiment displays stronger passivation than the API X70 and acetic acid experiment. Although some slight passivation is observed in the case of the API X52 steel and acetic acid experiment, overall, the CTR continues to decline in both API X52 tests over this period. At the end of the testing duration, the CTR is lowest for the API X52 steel tests and highest for the API X70 steel tests.

The DLC and corresponding eta are displayed in

Figure 4.25 (c) and (d), respectively. DLC is observed to increase several orders of magnitude for all four experiments. DLC is observed to be roughly an order of magnitude less for the API X70-EtOH test compared to the API X70-HAc test. Little can be observed from the CPE double layer exponent. Most values remain around 0.7 to 1.

Solution resistance is given in

Figure 4.25 (a). Solution resistance for the four tests ranged from around 10 to 40 ohms*cm^2. Solution resistance begins at around 3 to 40 ohms*cm2 for both the API X52-EtOH and the API X70-HAc. Solution resistances begin around 15 to 20 ohms*cm^2 for the API X70-EtOH and API X52-HAc tests. All solution resistances decrease during the experiments.

The parameters given in

Figure 4.26 describe circuit elements that correspond to the additional time-constant in the data for all four experiments. Given the nature of the system, the reasonable assumption is made that the second time-constant corresponds to the formation of an iron sulfide on the surface of the metal. The resistance of the iron sulfide film varies considerably between the experiments. The capacitance of the iron sulfide film consistently increases several orders of magnitude for all experiments. As general corrosion rates increase for most of the testing duration and then remain high, it can be assumed that the film is not very protective for the API X52 steel tests. The iron sulfide layer may be more protective in the case of the API X70 steel tests. Little can be concluded from the eta values.

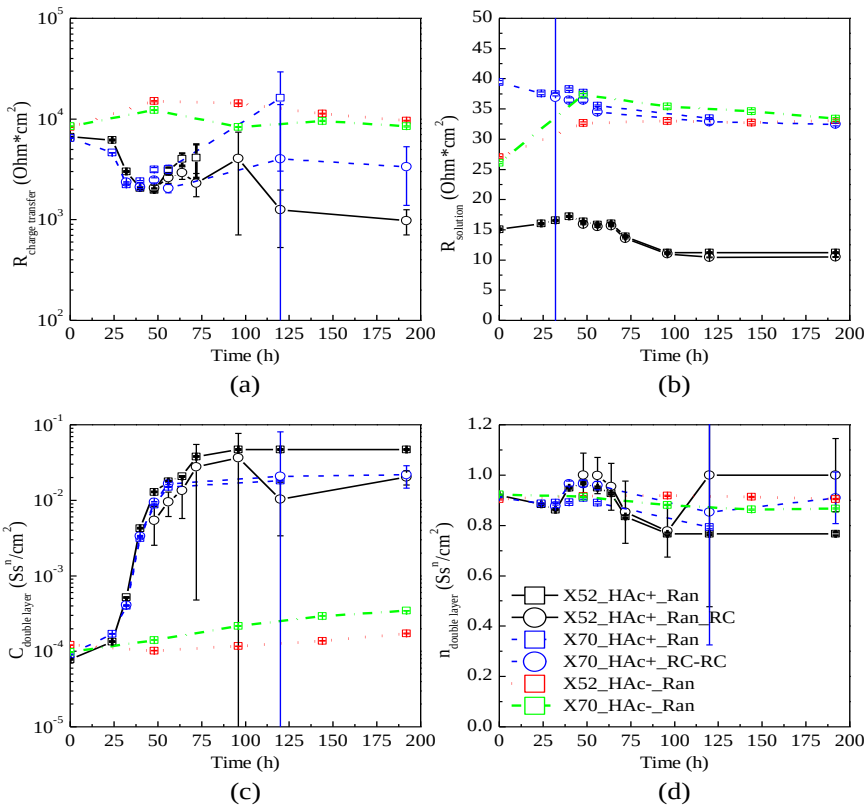

Figure 4.23 Corrosion parameters for API X52 and X70 steels immersed in modified Postage B growth media with one gram per liter acetic acid and inoculated with SRB showing (a) charge-transfer resistance, (b) solution resistance, (c) double-layer capacitance, and (d) constant phase element exponent, **η**

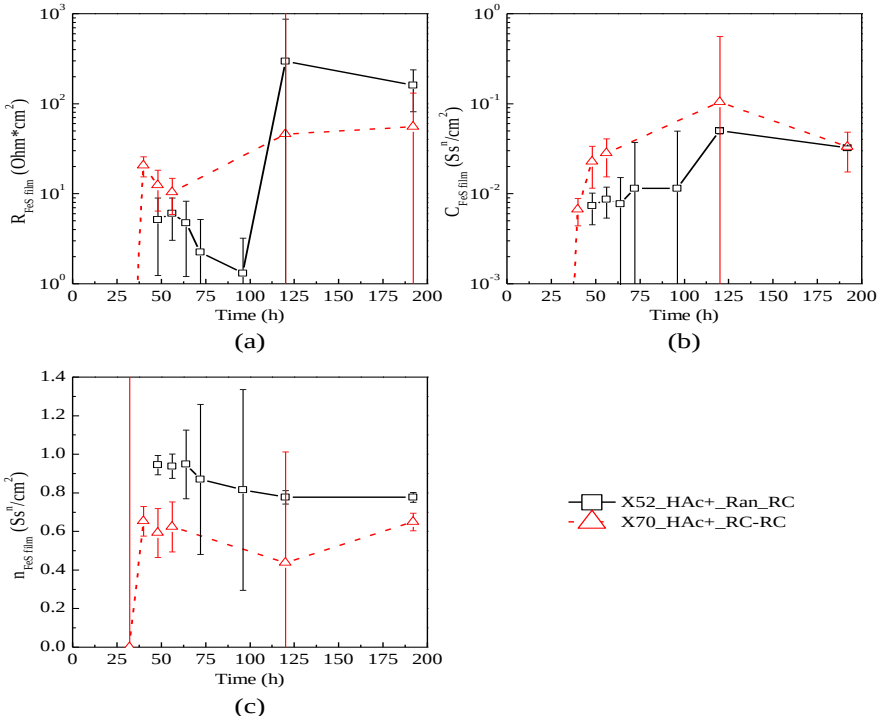

Figure 4.24 Corrosion parameters for API X52 and X70 steels immersed in modified Postage B growth media with one gram per liter acetic acid and inoculated with SRB showing (a) resistance, (b) iron sulfide capacitance and (c) constant phase element exponent, **η**

Linepipe Steels Exposed to SRB with Oil Containment

Corrosion experiments described in the proceeding sections of this Chapter were designed to evaluate the influence of the isolated SRB cultures containing the species grouping with *Clostridium sp.* and *Desulfosporosinus sp.* on corrosion of two linepipe steels while consuming both acetic acid (HAc) and ethanol (EtOH) as a carbon source. Several interesting trends were observed in the electrochemical properties and corrosion parameters of the systems. Many of these behaviors appear to maintain a consistent relationship with significant experimental variables such as steel type or solution chemistry. To further increase confidence in these observations, the four inoculated experiments were repeated with one minor modification. This modification was the addition of an approximately 1-inch layer of vegetable oil over the growth media to form a more effect barrier between the deaerated media and the atmosphere. It was thought that the addition of vegetable oil over the negative control experiments would not significantly affect corrosion behavior and therefore negative controls were not repeated in this study.

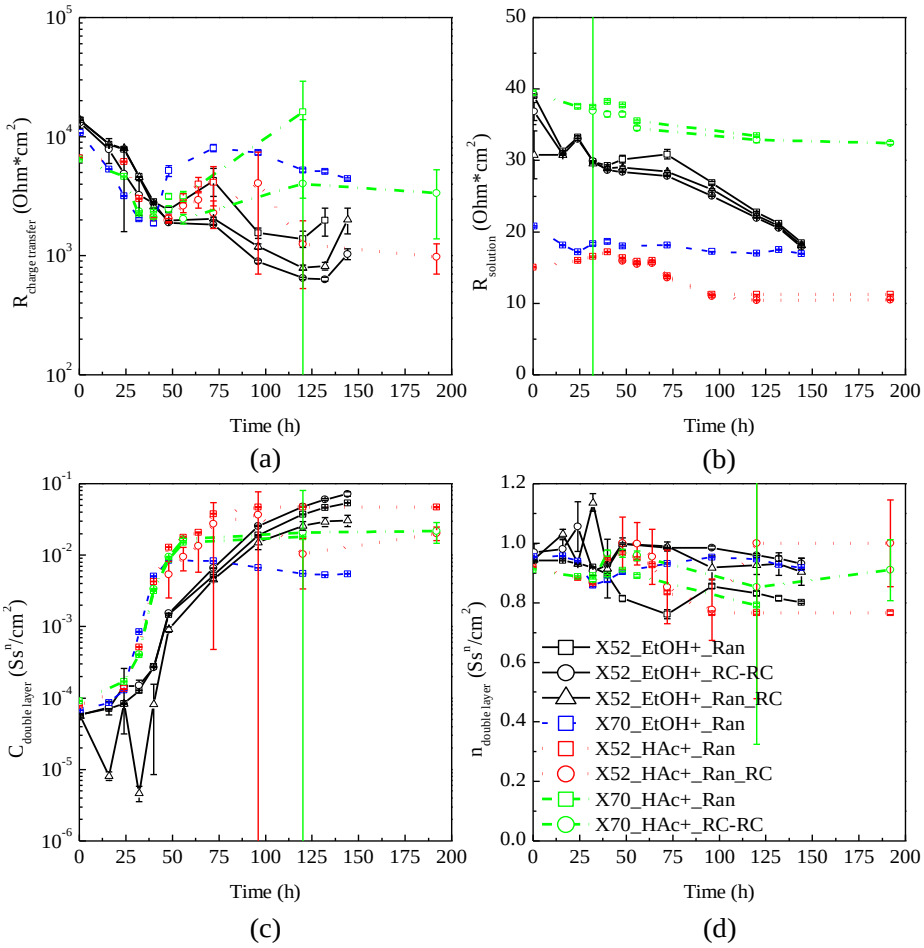

Figure 4.25 Combined corrosion parameters for API X52 and X70 steels immersed in modified Postage B growth media with ethanol or acetic acid additions and inoculated with SRB showing (a) charge-transfer resistance, (b) solution resistance, (c) double-layer capacitance, and (d) constant phase element exponent, **η**

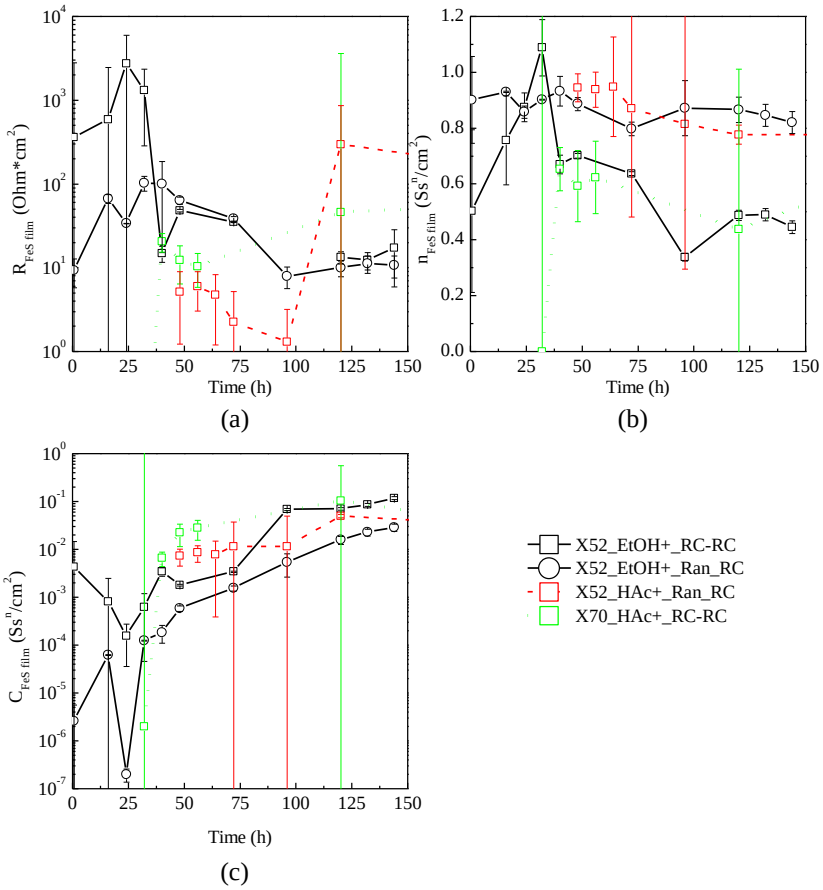

Figure 4.26 Combined corrosion parameters for API X52 and X70 steels immersed in modified Postage B growth media with ethanol or acetic acid additions and inoculated with SRB showing (a) resistance, (b) constant phase element exponent, **η** and (c) capacitance of the iron-sulfide film

The PR measurements taken from the four cells are presented in

Figure 4.27 (a). Corrosion rates (CR) calculated from the PR data are presented in

Figure 4.27 (b). It is evident from the PR and CR graphs in

Figure 4.27 that all cells experienced an initial increase in corrosion rate for the first 2 to 4 days after immersion. This coincides with the initial decrease in the OCP. After the initial drop in PR is arrested, there is observable passivation for the API X52-EtOH, API X70-EtOH, and API X70-HAc tests. The degree of passivation is greatest for the API X70-EtOH test but less pronounced for the API X52-EtOH and API X70-HAc test. After the initial increase in corrosion and passivation, CRs for the tests remain relatively constant for the testing duration. At the end of the test, PR for the API X52-EtOH cell was around 300 ohms*cm2 corresponding to a CR of around 36 mpy. The PR for the API X70-EtOH cell was around 3000 ohms*cm2 corresponding to a CR of around 3 mpy. The PR for the API X52-HAc cell was around 160 ohms*cm2 corresponding to a CR of around 60 mpy. The PR for the API X70-HAc cell was around 25000 ohms*cm2 corresponding to a CR of around 40 mpy.

The OCP, measured at regular intervals during all four experiments, is presented in

Figure 4.27 (c). The OCP for all the tests initially experienced a 10 to 20 millivolt decrease within the first 2 to 3 days after immersion. This initial decrease in OCP was followed by a sharp ennoblement, observed in all of the systems. This ennoblement brought potentials for the API X52-EtOH test and both HAc tests to around -

670 mV versus SCE. The OCP remained near this value for the API X52-EtOH test. The OCP declined to around -690 mV versus SCE in the case of the API X52-HAc test and declined to around -700 mV versus SCE in the case of the API X70-HAc test.

EIS data, presented as nyquist, modulus, high-frequency nyquist, and phase plots, are displayed in Figure 4.29 (a), (b), (c) and (d), respectively. These data were acquired from the API X70 ethanol corrosion cell inoculated with SRB at -2, 24, 32, 40, 48, 56, 64, and 216 hours after immersion. This data is displayed clockwise from top-left as nyquist, modulus, phase and high frequency modulus in the Figure. It is apparent from both the nyquist and modulus plots that there is a significant decrease in the low-frequency limit of the impedance for the system. This observation fits well with the dramatically increasing corrosion rates observed in the PR data. The most obvious behavior exhibited by the phase plot is the dramatic increase in DLC indicated by the shift in the center of the primary peak from around 10 Hz to around 10^{-2} Hz. A small inflection is observed in the phase curve around 40 Hz. This inflection is most notable at 48 hours after immersion. This feature corresponds to curvature in the high frequency nyquist plot at 48 hours after immersion. This evidence of a second time-constant in the data suggests the presence of an additional layer or film near the metal-solution interface. The behavior observed in the data gives justification for the application of equivalent circuit models incorporating two time-constants rather than the lone time-constant in the Randles Circuit.

EIS data, presented as nyquist, modulus, high-frequency nyquist, and phase plots, are displayed in Figure 4.30 (a), (b), (c) and (d), respectively. These data were acquired from the API X52 acetic acid corrosion cell inoculated with SRB at -2, 24, 48, 56, 64, 72, 96, and 216 hours after immersion. This data is displayed clockwise from top-left as nyquist, modulus, phase and high frequency modulus in the Figure. It is apparent from both the nyquist and modulus plots that there is a significant decrease in the low-frequency limit of the impedance for the system. This observation fits well with the dramatically increasing corrosion rates observed in the PR data. The most obvious behavior exhibited by the phase plot is the dramatic increase in DLC indicated by the shift in the center of the primary peak from around 10 Hz to around 10^{-2} Hz. A pronounced second time-constant is observed in the phase curve from 1 to 1000 Hz. This time-constant is best defined at 56 hours after immersion but noticeable throughout the remainder of the testing duration. A well-defined semicircle is evident in the high frequency nyquist plot at 56 hours after immersion and curvature is observed throughout the remainder of the testing duration. This evidence of a second time-constant in the data strongly suggests the presence of an additional layer or film near the metal-solution interface. The behavior observed in the data gives justification for the application of equivalent circuit models incorporating two time-constants rather than the lone time-constant in the Randles Circuit.

EIS data, presented as nyquist, modulus, high-frequency nyquist, and phase plots, are displayed in

Figure 4.31 (a), (b), (c) and (d), respectively. These data were acquired from the API X70 acetic acid corrosion cell inoculated with SRB at -2, 24, 48, 56, 64, 72, 96, and 216 hours after immersion. This data is displayed clockwise from top-left as nyquist, modulus, phase and high frequency modulus in the Figure. It is apparent from both the nyquist and modulus plots that there is a significant decrease in the low-frequency limit of the impedance for the system. This observation fits well with the dramatically increasing corrosion rates observed in the PR data. The most obvious behavior exhibited by the phase plot is the dramatic increase in DLC, indicated by the shift in the center of the primary peak from around 10 Hz to around 10^{-2} Hz. A prominent secondary peak is observed in the phase curve around 10 Hz. This peak is most notable at 56 hours after immersion. Slight curvature can be seen in the high frequency nyquist plot at 56 hours after immersion and after. This evidence of a second time-constant in the data suggests the presence of an additional layer or film near the metal-solution interface. The behavior observed in the data gives justification for the application of equivalent circuit models incorporating two time-constants rather than the lone time-constant in the Randles Circuit.

The raw impedance data from the four experiments was modeled using all three of the equivalent circuit models shown in Figure 4.32(a). Goodness of fit, plotted in Figure 4.32(b), demonstrates fitting quality for models applied to all four experiments. It can be observed that the Chi^2 values range from approximately 10^{-2} to 10^{-4}. In general, fitting quality appears to be as good as or better than that for the previous SRB studies. The Randles Circuit can be seen to provide acceptable fits for the beginning of the test durations but the two time-constant models fit the data better as the experiments proceed.

Corrosion parameters extracted from modeling the impedance spectra from the four cells are displayed in Figure 4.33

Figure 4.34. Parameters describing the metal-solution interface include the CTR given as $R_{charge\ transfer}$, solution resistance given as $R_{solution}$, and the DLC described by $C_{double\ layer}$ and $\eta_{double\ layer}$ shown in Figure 4.33 (a), (b), (c) and (d), respectively. Parameters describing the iron sulfide film include the iron sulfide film resistance given as $R_{FeS\ film}$ and the iron sulfide film capacitance described by $C_{FeS\ film}$ and $\eta_{FeSe\ film}$ shown in

Figure 4.34 (a), (b), and (c), respectively. The legend in the lower-right corner of the Figure applies to all four graphs.

The CTR is shown in Figure 4.33 (a). CTR decreases significantly for all systems for the first 2 to 4 days after immersion. The CTR decreases the least in the case of the HAc tests and the API X70-EtOH test. The increase in CTR is followed by an approximately 1-day period of sharp increase in CTR for both API X70 tests. The API X52 tests do not exhibit this pronounced increase in CTR. All tests show a gradual increase in CTR from 100 hours after immersion until the end of the testing duration. At the end of the testing duration, the CTR is highest for the API X70-EtOH test. The API X70-HAc test exhibits an intermediate CTR and the two API X52 tests show the lowest CTR.

The DLC and corresponding eta is shown in Figure 4.33 (c) and (d), respectively. DLC is observed to increase several orders of magnitude for all four experiments. DLC appears to be roughly an order of magnitude less for the API X70-EtOH test compared to the other three tests. The increase in DLC appears to coincide with and be indirectly proportional to the decrease in CTR. Little can be observed from the CPE double layer exponent as most values group between 0.8 to 1.

Solution resistance is given in Figure 4.33 (b). Solution resistance for the four tests ranged from around 1 to 40 ohms*cm^2. Solution resistance begins at around 35 ohms*cm^2 for both ethanol tests and then decreases. Solution resistances begin around 18 and 28 ohms*cm^2 for the API X52-HAc and API X70-HAc tests, respectively. All solution resistances decrease during the experiments. The solution resistances at the end of the testing duration are around 1 ohm*cm^2 for the both HAc tests and the API X52-EtOH tests. The solution resistance at the end of the testing is around 15 ohms*cm^2 for the API X70-HAc test.

The parameters given in

Figure 4.34 describe circuit elements that correspond to the additional time-constant in the data for all four experiments. Given the nature of the system, the reasonable assumption is made that the second time-constant corresponds to the formation of an iron sulfide on the surface of the metal. Consistent with the inspection of the impedance spectra in Figure 4.28, Figure 4.30, and

Figure 4.31, the resistance, and therefore presence of the iron-sulfide film, is first observed around 50 hours after immersion and remains for the duration of the experiments. Easily identifiable trends are not evident in the capacitance of the iron sulfide film. As general corrosion rates increase for most of the testing duration and then remain high, it can be assumed that the film is not very protective for the API X52 steel and acetic acid tests. The iron sulfide layer may be protective in the case of the API X70 steel and ethanol test. Eta values for the iron-sulfide film are closer to 1 when the data is fit using the "Ran_RC" model than when using the "RC-RC" model. While the models are applied to two different systems, the repeat of this behavior may further suggest that the configuration of the "Ran_RC" circuit model provides a more ideal representation of circuit elements.

Microscopy of Linepipe Steels Exposed to Isolated Cultures

After the electrochemical corrosion evaluation described in the proceeding sections of this Chapter was completed, the working electrodes were carefully removed from the corrosion cells and inspected via scanning electron microscopy (SEM) and energy dispersive x-ray spectroscopy (EDS). The SEM was used to study corrosion morphology while EDS was applied to characterize the chemical composition of features of interest. Two microscopes, described in Chapter 3, were used. One was an environmental scanning electron microscope (ESEM) and the other was a field emission scanning electron microscope (FESEM). This section presents SEM and EDS inspection of biofilm, corrosion product, and corrosion damage on the surface of the corroded steel coupons.

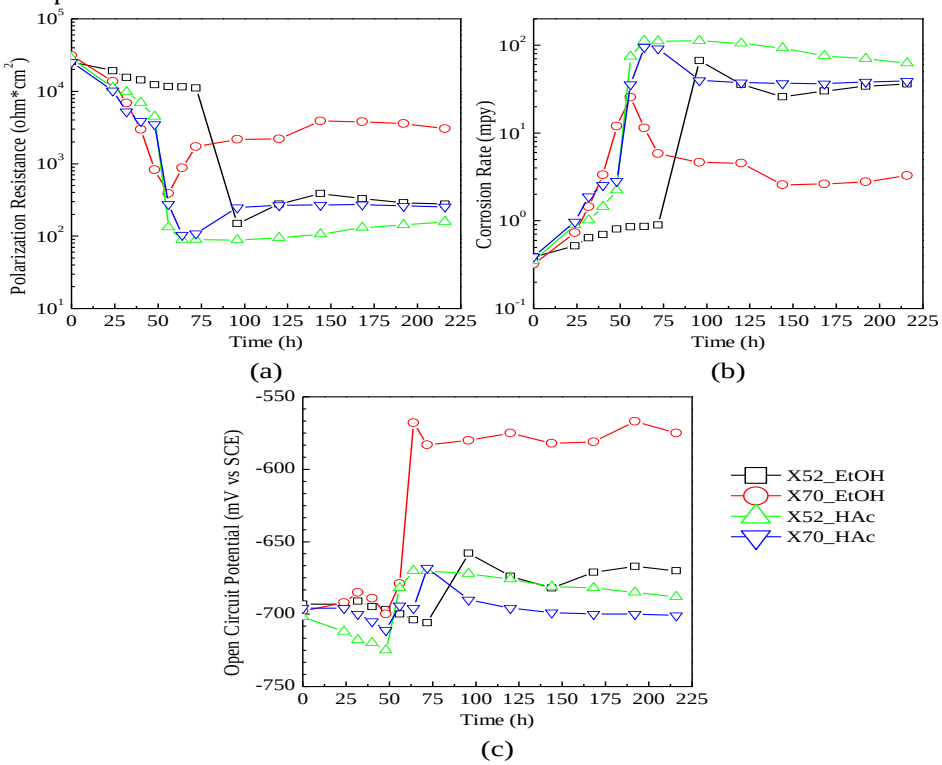

Figure 4.27 Experimental data from the sulfate reducing consortium with oil tests series including (a) polarization resistance, (b) corrosion rate, and (c) open circuit potential

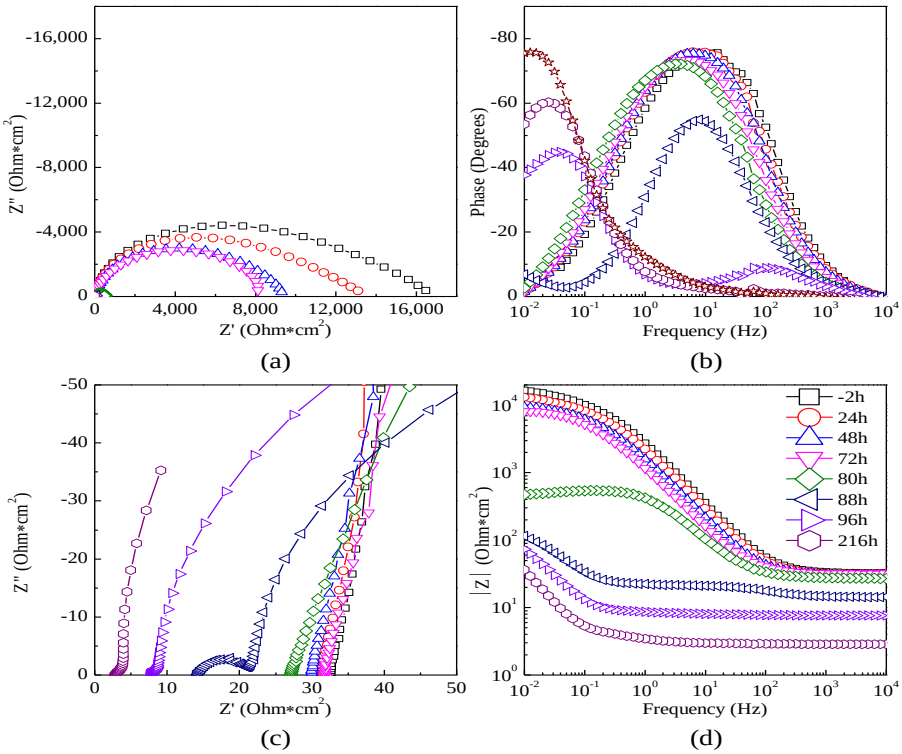

Figure 4.28 Electrochemical impedance data for API X52 steel immersed in modified Postage B growth media with two vol. pct. ethanol oil and inoculated with SRB showing (a) nyquist, (b) modulus, and (c) high frequency modulus and (d) phase plots

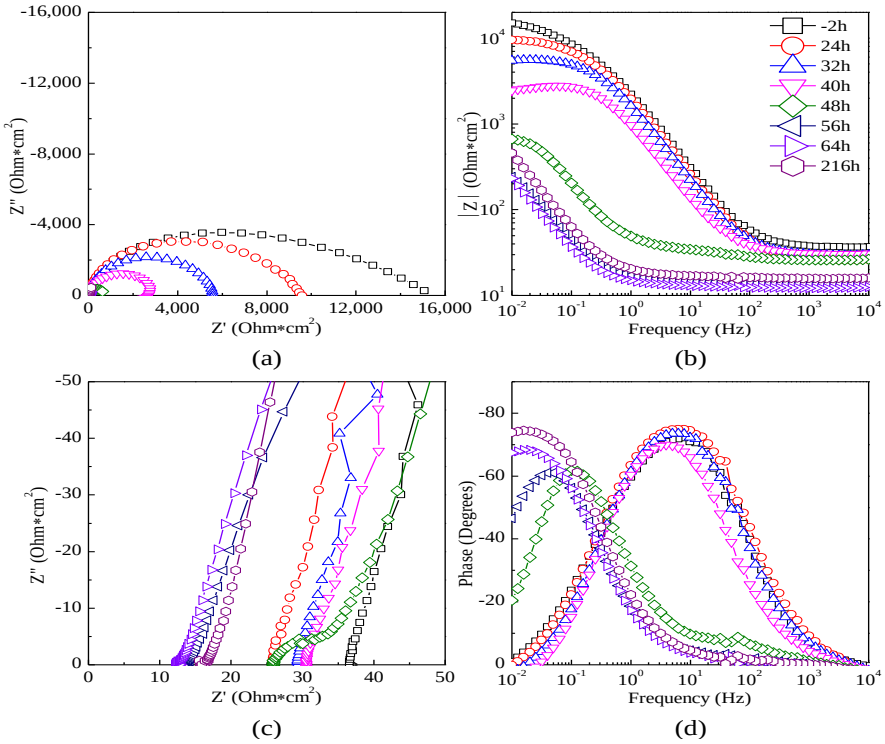

Figure 4.29 Electrochemical impedance data for API X70 steel immersed in modified Postage B growth media with two vol. pct. ethanol covered oil and inoculated with SRB showing (a) nyquist, (b) modulus, and (c) high frequency modulus and (d) phase plots

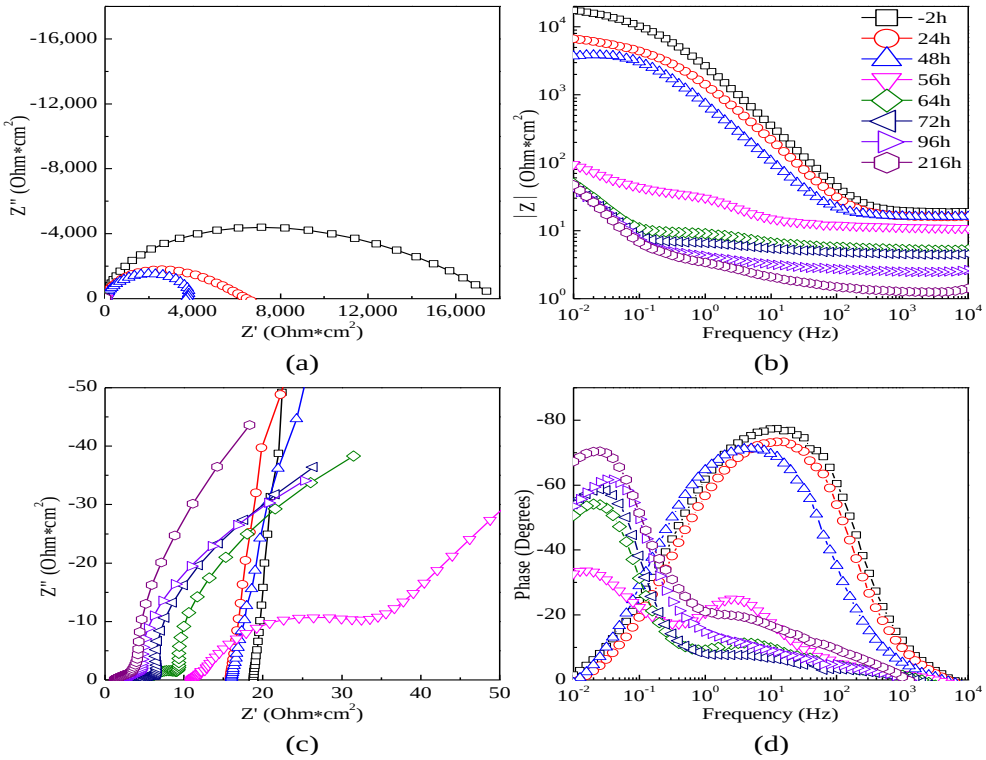

Figure 4.30 Electrochemical impedance data for API X52 steel immersed in modified Postage B growth media with one gram per liter acetic acid covered oil and inoculated with SRB showing (a) nyquist, (b) modulus, and (c) high frequency modulus and (d) phase plots

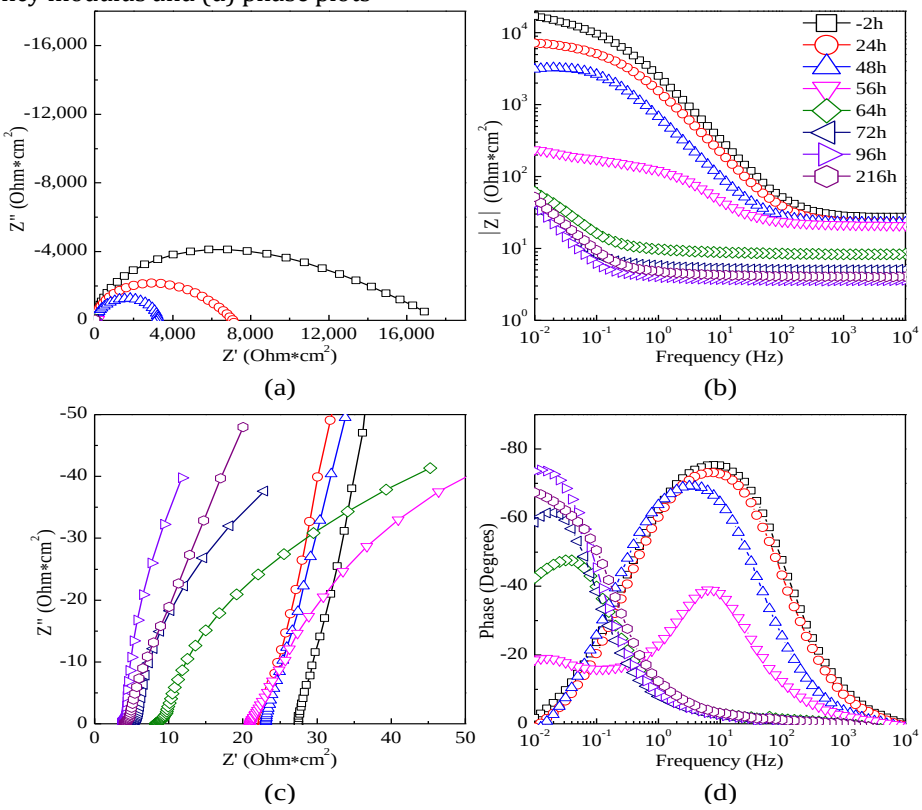

Figure 4.31 Electrochemical impedance data for API X70 steel immersed in modified Postage B growth media with one gram per liter acetic acid covered oil and inoculated with SRB showing (a) nyquist, (b) modulus, and (c) high frequency modulus and (d) phase plots

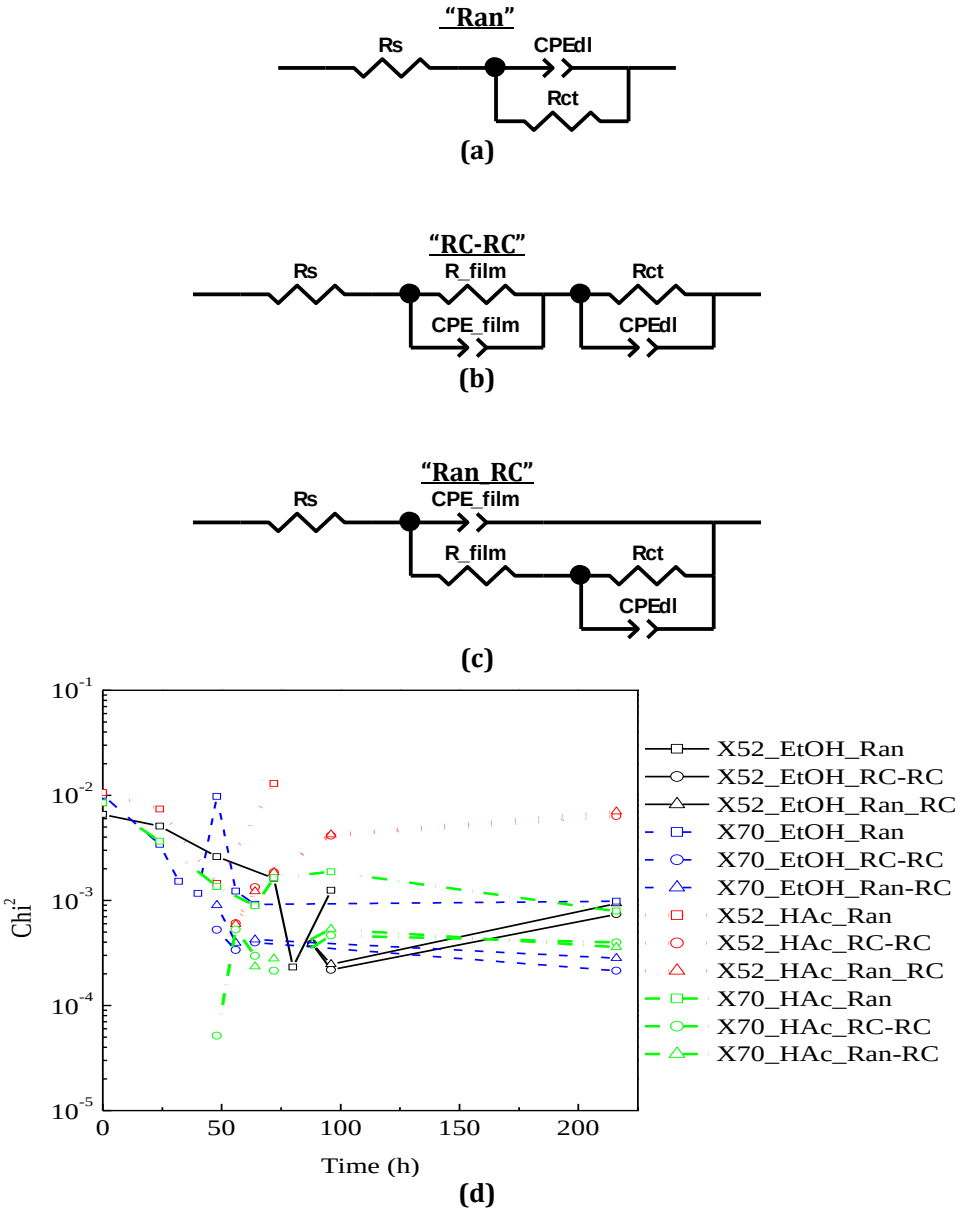

Figure 4.32 (a) Representations of applied equivalent circuit models (b) Goodness of fit of the applied equivalent circuit models to the experimental electrochemical impedance data from the SRB consortium with oil study

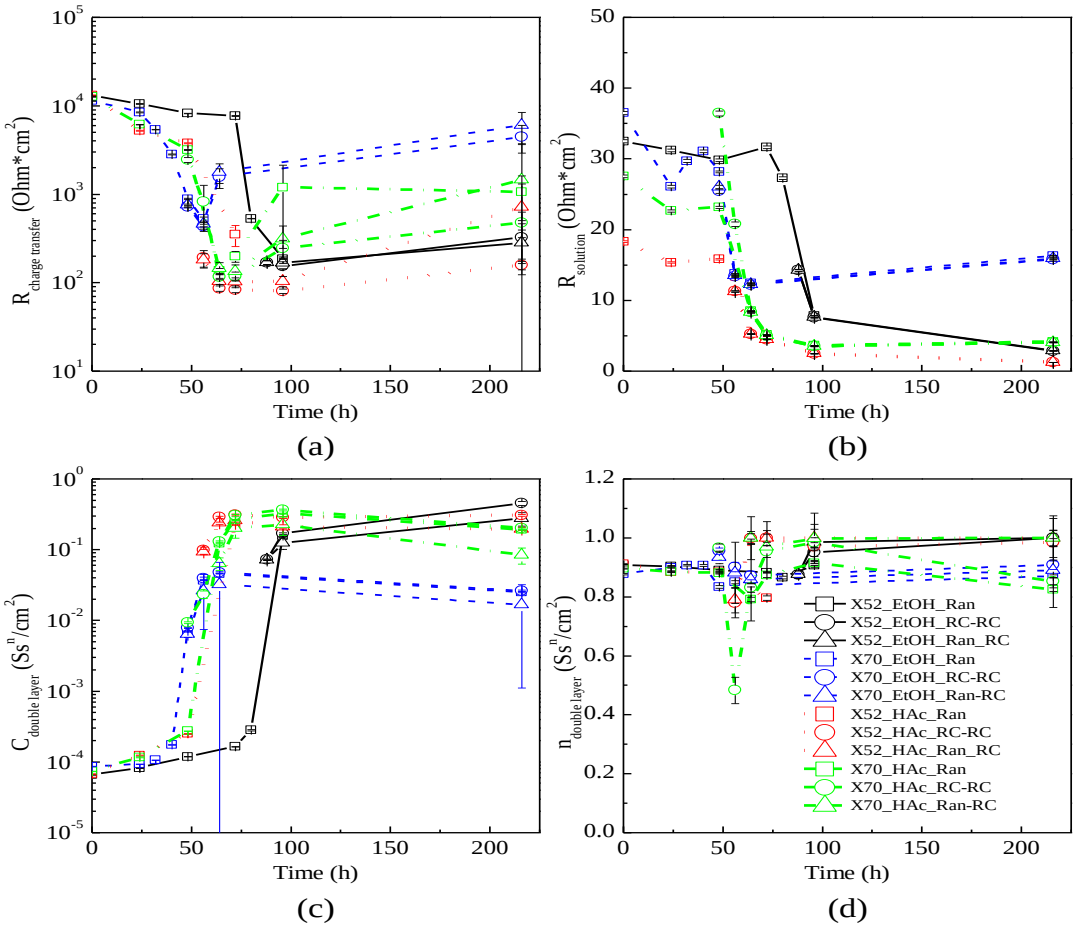

Figure 4.33 Corrosion parameters for API X52 steel with two vol. pct ethanol, API X70 steel with two vol. pct ethanol, API X52 steel with one gram per liter acetic acid, and API X70 steel with one gram per liter acetic acid immersed in modified Postage B growth media and inoculated with SRB showing (a) charge-transfer resistance, (b) solution resistance, (c) double-layer capacitance, and (d) constant phase element exponent, **η**

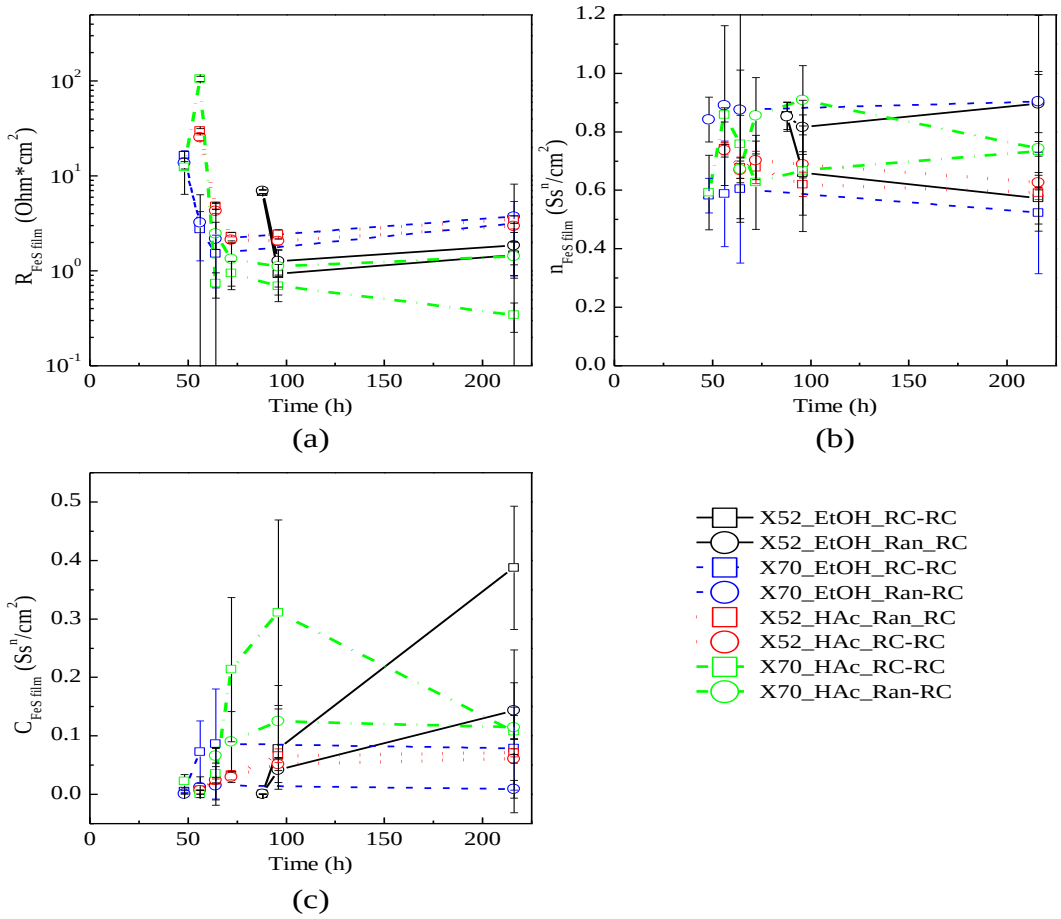

Figure 4.34 Corrosion parameters for API X52 steel with two vol. pct ethanol, API X70 steel with two vol. pct ethanol, API X52 steel with one g per liter acetic acid, and API X70 steel with one gram per liter acetic acid immersed in modified Postage B growth media and inoculated with SRB showing (a) iron sulfide film resistance, constant phase element exponent, and iron-sulfide film capacitance

Linepipe Steel Exposed to SRB Consortium with Ethanol

An electrochemical corrosion study (described earlier in this Chapter) was conducted to evaluate the influence of an isolated SRB culture containing species grouping with *Clostridium sp.* and *Desulfosporosinus sp.* on corrosion of API X52 linepipe steel and API X70 linepipe steels. The electrochemical immersion tests were conducted in a modified Postgate B growth media containing 2 vol. pct. ethanol added as the microbial carbon source. After completion of electrochemical testing, the working electrodes from the inoculated cells were removed from the testing media and prepared for microscopic inspection. The specimens were imaged as recovered from the corrosion cell and after cleaning according to ASTM G1 Standard Practice (ASTM 2003).

The API X52 steel working electrode was first imaged prior to cleaning. The surface of the electrode displayed in

Figure 4.35(a). This image shows coverage of the steel surface with a thick, coherent layer of corrosion product. This is representative of the entire electrode surface. The corrosion product can also be observed at high magnification in

Figure 4.35 (b). The high-resolution image, [

Figure 4.35 (b)], indicates that the film consists of fine crystals. The thin plate-like morphology of these crystals appears similar to that of mackinawite precipitated on API X65 steel in the presence of hydrogen sulfide and carbon dioxide (Sun and Nesic 2009). The EDS spectra given in

Figure 4.35 (d) indicate that the film is predominately composed of iron, sulfur, oxygen, and carbon.

The surface of the API X70 steel electrode was also imaged prior to cleaning. In contrast to the API X52 steel electrode, much less corrosion product was observed on the steel surface. The general appearance of the surface is shown in Figure 4.36 (a). Two distinct zones can be distinguished based on apparent color of the surface. In some of the lighter regions, microbial tubercles can be observed. These tubercles are often associated with sites of localized MIC and pitting. Higher resolution images acquired of these lighter colored tubercles are shown in Figure 4.36 (b) and (d). The high-resolution images show dense microbial colonization of the electrode surface. Extensive cell adhesion and biofilm development is evident. Inspection of the darker areas, shown in Figure 4.36 (c), demonstrates a thin layer of corrosion product. This corrosion product is presumed to be iron sulfide due to the nature of the testing environment and the color. Minimal corrosion damage is anticipated on these areas, as polishing marks are still visible.

Both API X52 and API X70 steel electrodes were cleaned according to ASTM G1 Standard Practice (ASTM 2003), rinsed with DI water and 200 proof absolute ethanol, dried with forced air, and held in a low humidity atmosphere. The microscopy subsequently conducted was intended to inspect the morphology of the corrosion damage on the surface of the electrode. The relationship between the observed corrosion and the metallurgy of the steels was also evaluated.

The cleaned steel electrodes were imaged at low magnification in Figure 4.37. The most striking observation is the irregular pitting observed in Figure 4.37(b) on the surface of the API X70 steel electrode. Closer inspection of the API X52 steel electrode in Figure 4.37(a) shows variations in surface roughness, displayed as relatively lighter or darker shades in the image.

Higher magnification inspection of the cleaned surface of the API X52 steel electrode is presented in Figure 4.38, Figure 4.39, and Figure 4.40. Images in Figure 4.38, taken at are representative of the relatively less rough (less corroded) areas of the electrode. Images in Figure 4.39 are representative of the relatively rougher (more corroded) areas. Corrosion appears to proceed in an irregular but mostly general fashion. Intergranular attack producing microstructural relief and etching of pearlite colonies can be observed. The images in Figure 4.39 also show preferential etching of select ferrite grains in a regular, rectangular, and repeating manner. The attack appears to be on an un-preferred orientation, as the areas of the attacked grains are generally less than the average grain size observed in the image. These features are shown at much higher resolution in Figure 4.40. This secondary attack, found predominantly in the more corroded areas on the surface, may be the result of the localized aggressive conditions.

Microscopy of the cleaned surface of the API X70 steel electrode is presented in Figure 4.41,Figure 4.42, and Figure 4.43. The relatively lower magnification images shown in Figure 4.41 show the pitting morphology on the electrode surface. Polishing striations can be observed on the relatively un-corroded areas surrounding the pits. Microstructural etching is largely absent from these areas. Images in Figure 4.42 show the morphology of the pit interiors. Intergranular attack seems to be the primary mode of corrosion. The surface is also characterized by the presence of small voids having roughly the same size and distribution as carbides observed in the polished API X70 steel microstructure. The high-resolution images shown in Figure 4.43(a) and (b) more clearly depict the intergranular nature of the attack. Multiple triples-points are evident in the etched microstructure. Rectangular etch pits in ferrite grains are also evident. The images in Figure 4.43(c) and (d) were acquired from the un-corroded area of the surface adjacent to the pits. The presence of polishing marks is observed. The anticipation of low corrosion rates upon inspection of Figure 4.36 (c) (prior to cleaning) seem to be confirmed by the images in Figure 4.43.

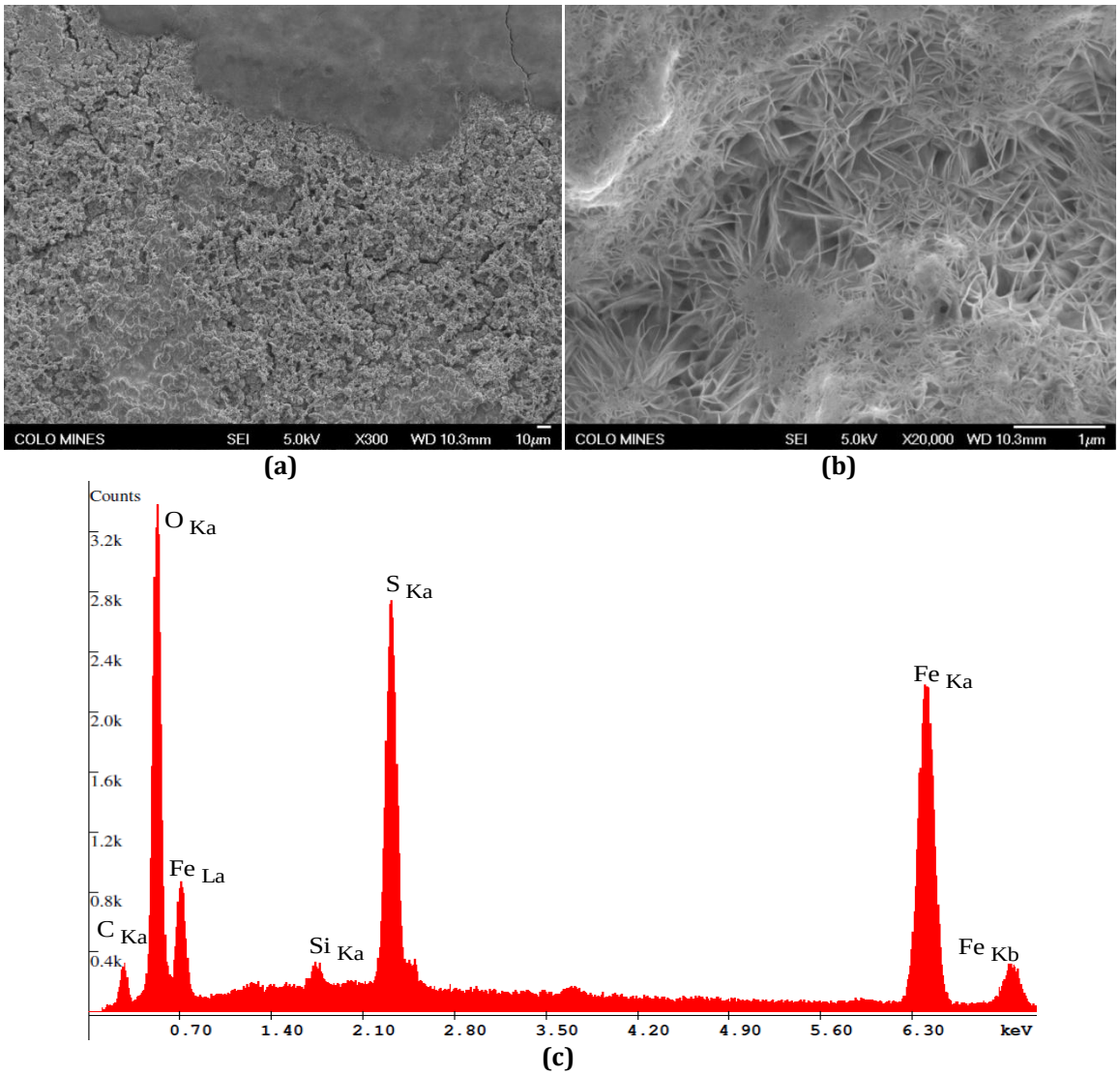

Figure 4.35 FESEM of API X52 steel surface in modified Postgate B media inoculated with an SRB consortium removed after 10 days of immersion showing corrosion product (a) 100x (b) 20,000x (c) corresponding EDS spectra

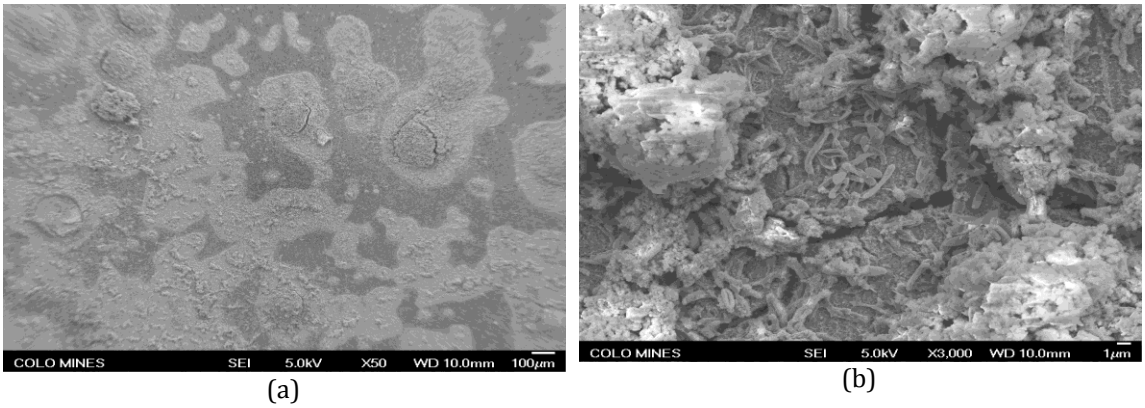

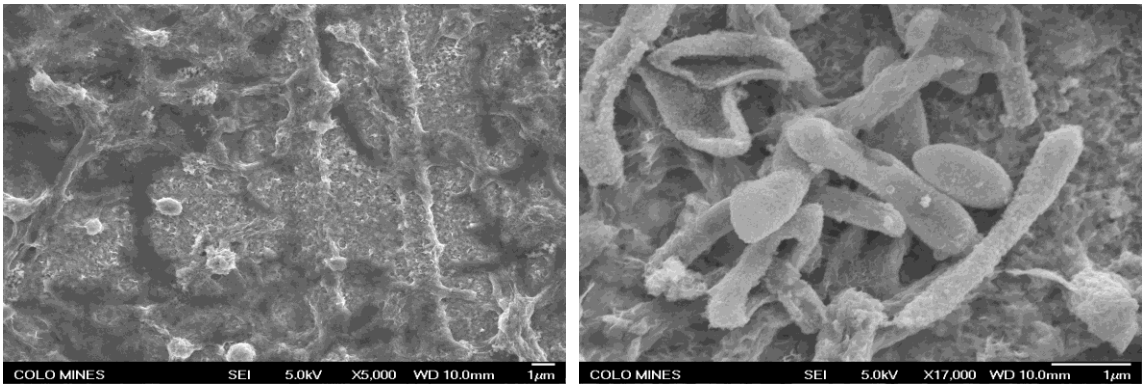

(c) **(d)**

Figure 4.36 (a) FESEM of API X70 steel in modified Postgate B media inoculated with SRB removed after 10 days of immersion (a) 50x (b) 3,000x (c) 17,000x (d) 30,000x magnification

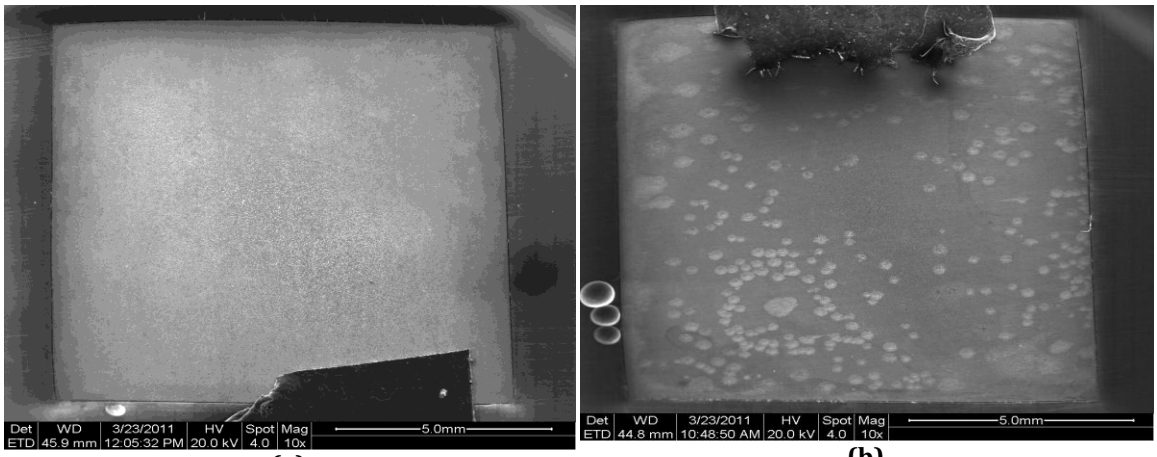

(a) **(b)**

Figure 4.37 ESEM of (a) API X52 and (b) API X70 steel exposed to SRB removed from modified Postgate B media with 2 vol. pct. ethanol after approximately 10 days of immersion and cleaned according to ASTM G1 Standard Practice

Linepipe Steel Exposed to SRB Consortium with Acetic Acid

An electrochemical corrosion study (described earlier in this Chapter) was conducted to evaluate the influence of an isolated SRB culture containing species grouping with *Clostridium sp.* and *Desulfosporosinus sp.* on corrosion of API X52 linepipe steel and API X70 linepipe steels. The electrochemical immersions tests were conducted in a modified Postgate B growth media containing one gram per liter acetic acid added as the microbial carbon source. After completion of electrochemical testing, the working electrodes were removed from the testing media and prepared for microscopic inspection. The specimens were imaged first after rinsing with DI water and then after cleaning according to ASTM G1 Standard Practice (ASTM 2003).

The API X52 steel working electrode was first imaged after rinsing with DI water to remove the thick corrosion product layer similar to that imaged in Figure 4.35 (a). The corrosion product layer was easily removed from the surface of the API X52 steel electrode. Beneath the thick layer of corrosion product, the steel surface was observed to have large colonies of *Clostridium sp*. covering vast stretches of the electrode. Images taken of one of these colonies are presented in Figure 4.44 (a) and (b). A few stray *Desulfosporosinus sp*. were also observed on the surface as shown in Figure 4.44 (c) and (d). It is not known if more colonies of *Desulfosporosinus sp*. were present on the surface but were removed due to washing with DI water.

The API X70 steel working electrode was also first imaged after rinsing with DI water. The API X70 electrode was covered by a much thinner but much more adhered layer of iron sulfide. Flushing with DI resulted in the removal of the corrosion product from one part of the surface of the electrode constituting approximately 15 pct. of the area of the electrode. The exposed surface of the electrode was imaged in Figure 4.45 and Figure 4.46. The image shown in Figure 4.45 (a) shows the boundary between the exposed steel surface and the region covered by the adherent iron sulfide film. The image in Figure 4.45 (b) contains a higher magnification image taken from along this boundary showing a *Desulfosporosinus sp*. cell embedded in or attached to the exposed steel surface. The images in Figure 4.45 (b) and (c) depict colonies of *Clostridium sp*. on the steel surface. Microstructural etching can also be observed in Figure 4.45, especially in Figure 4.45 (c) and (d). The images presented in Figure 4.46 were acquired from the steel surface exposed after removal of the non-adherent iron sulphide film. This region exhibited areas with varying degrees of roughness. Greater roughness is assumed to coincide with localized areas of the surface that experienced relatively more aggressive conditions and suffered greater corrosion. The images shown in Figure 4.46 (a) and (b) were taken from the less corrodes areas of the exposed steel surface. Microstructural etching is evident in these micrographs, however, attack appears to be relatively light. The images in Figure 4.46 (c) and (d) were acquired from the more corroded regions. Intergranular attack and striated ferrite grains are pronounced.

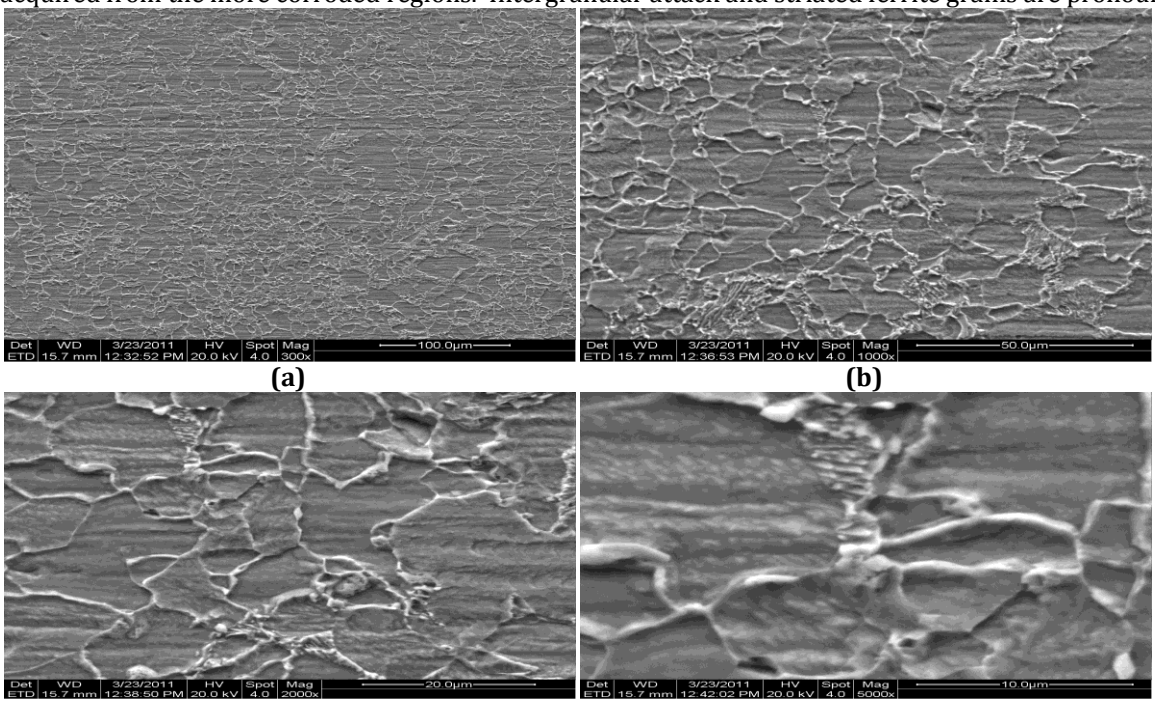

Figure 4.38 Representative SEM of less corroded areas of API X52 steel immersed in modified Postgate B growth media containing 2 vol. pct. ethanol, inoculated with SRB, removed after approximately 10 days of immersion, and cleaned according to ASTM G1 Standard Practice at Location 1 at (a) 300x (b) 700x (c) 2,000x (d) 5,000x magnification

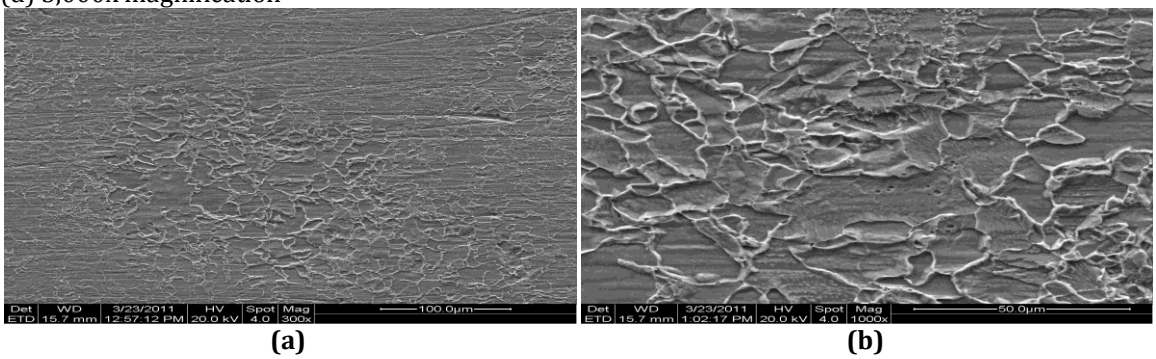

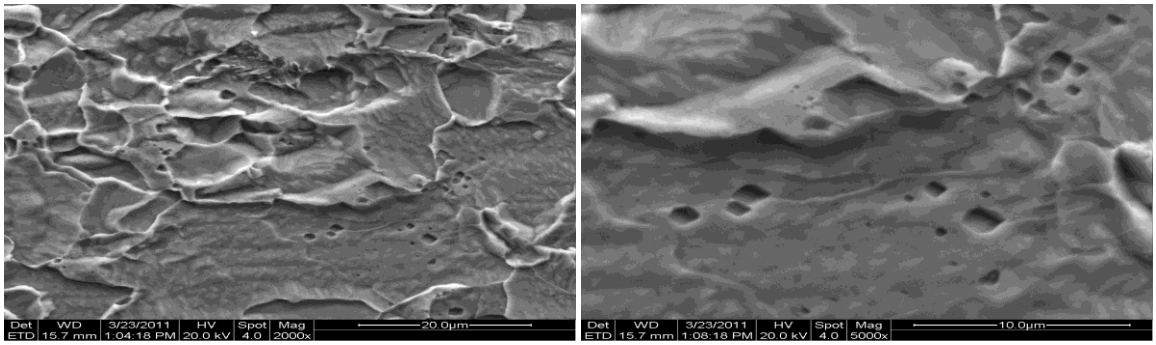

(c) **(d)**

Figure 4.39 Representative SEM of more corroded areas of API X52 steel immersed in modified Postgate B growth media containing 2 vol. pct. ethanol, inoculated with SRB, removed after approximately 10 days of immersion, and cleaned according to ASTM G1 Standard Practice at Location 1 at (a) 300x (b) 700x (c) 2,000x (d) 5,000x magnification

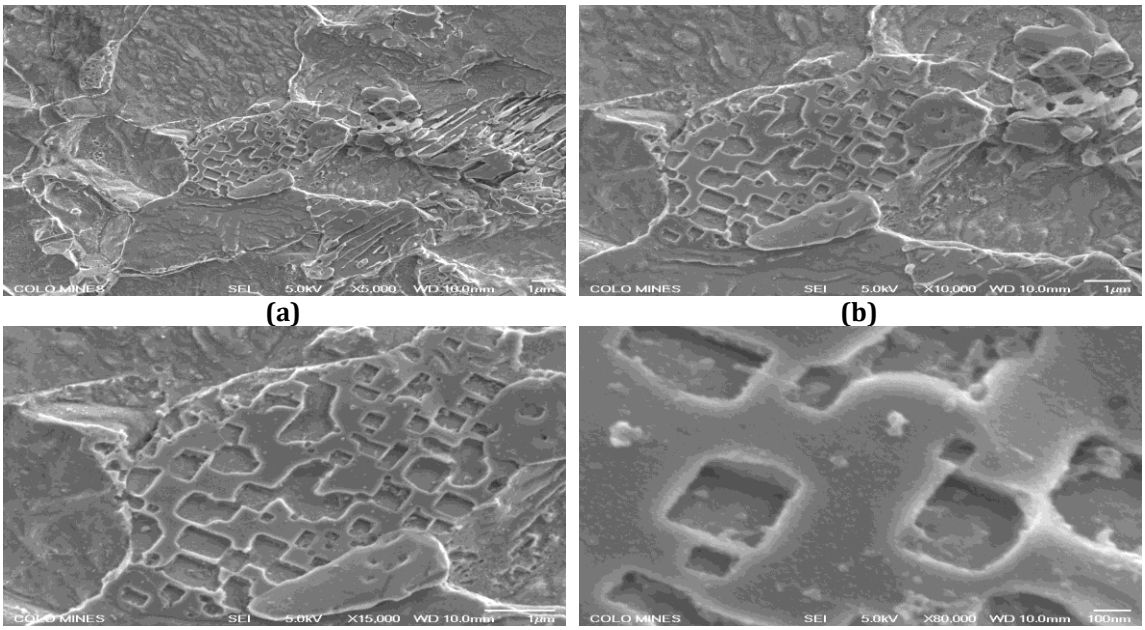

(a) **(b)**

(c) **(b)**

Figure 4.40 FESEM of API X52 steel in modified Postgate B media inoculated with SRB removed after 10 days of immersion and cleaned according to ASTM G1 Standard (a) 5,000x (b) 10,000x (c) 45,000x (d) 80,000x magnification

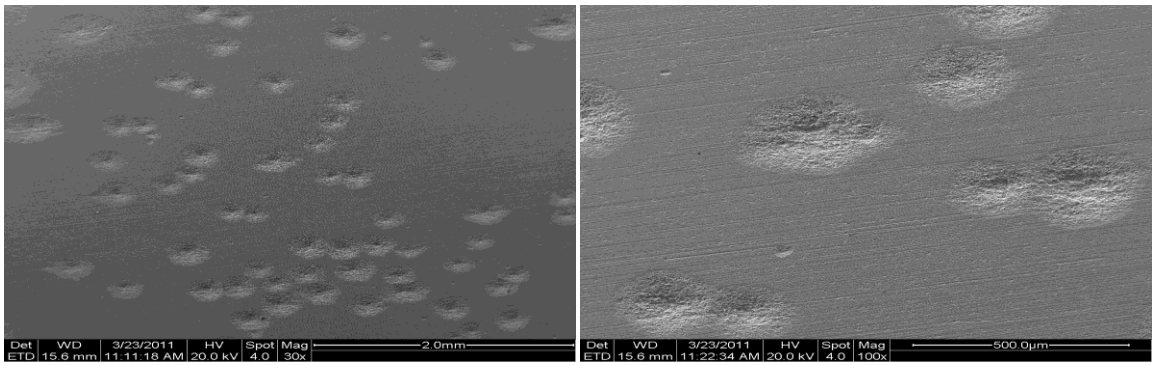

(a) **(b)**

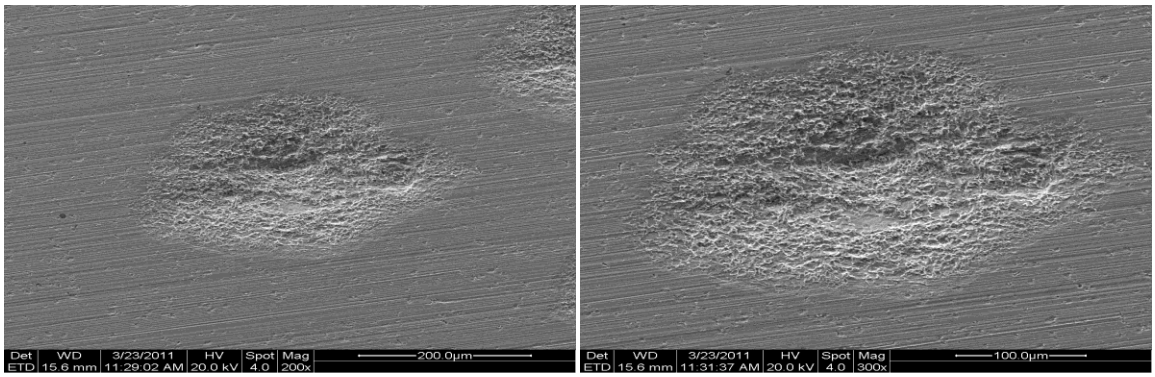

(c) **(d)**

Figure 4.41 Representative SEM of API X70 steel immersed in modified Postgate B growth media containing 2 vol. pct. ethanol, inoculated with SRB, removed after approximately 10 days of immersion, and cleaned according to ASTM G1 Standard Practice at Location 1 at (a) 30x (b) 100x (c) 200x (d) 300x magnification

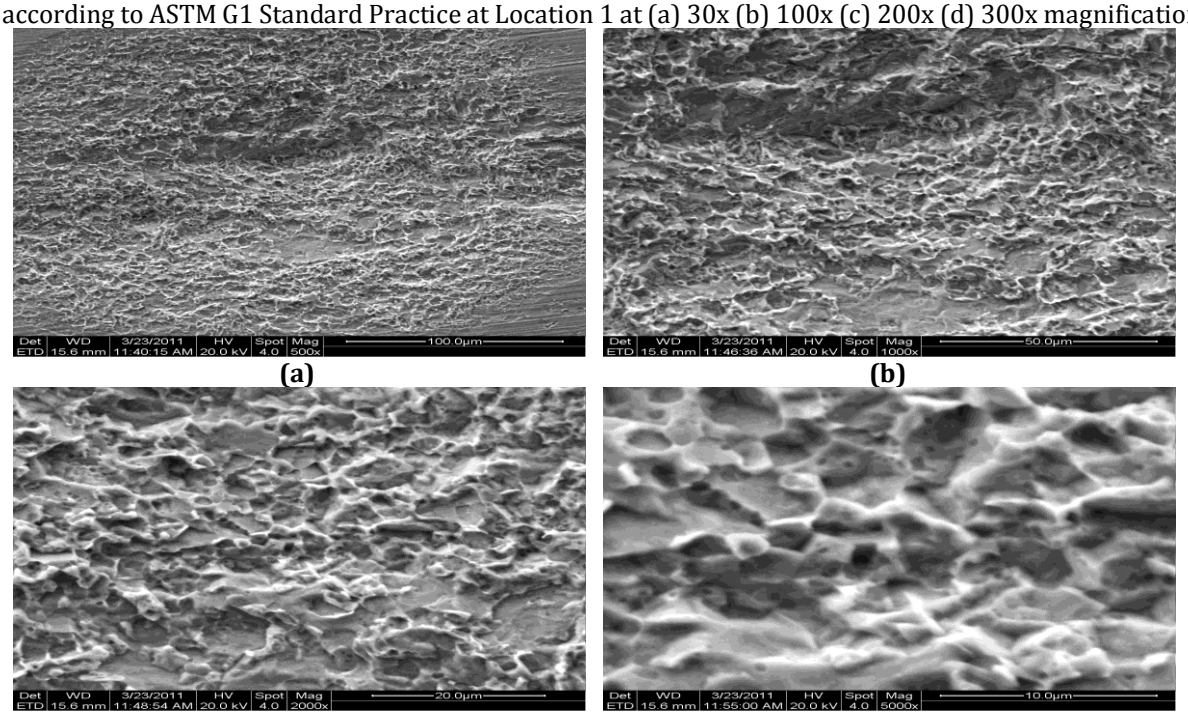

(a) **(b)**

(c) **(d)**

Figure 4.42 Representative SEM of API X70 steel immersed in modified Postgate B growth media containing 2 vol. pct. ethanol, inoculated with SRB, removed after approximately 10 days of immersion, and cleaned according to ASTM G1 Standard Practice at Location 1 at (a) 500x (b) 1,000x (c) 2,000x (d) 5,000x magnification

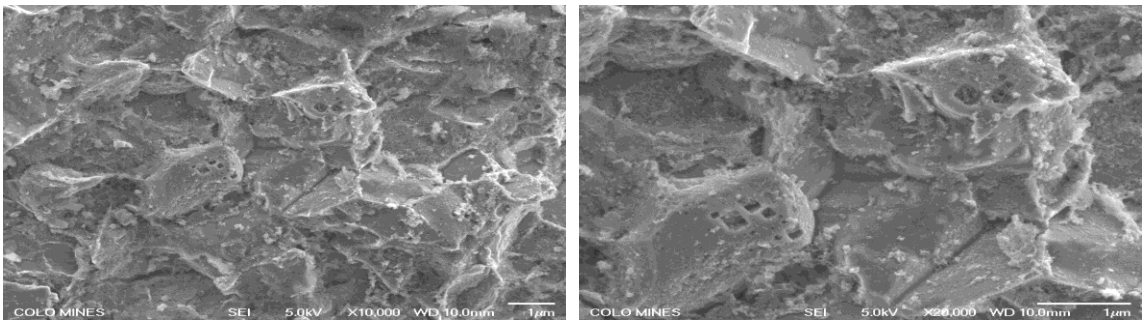

(a) **(b)**

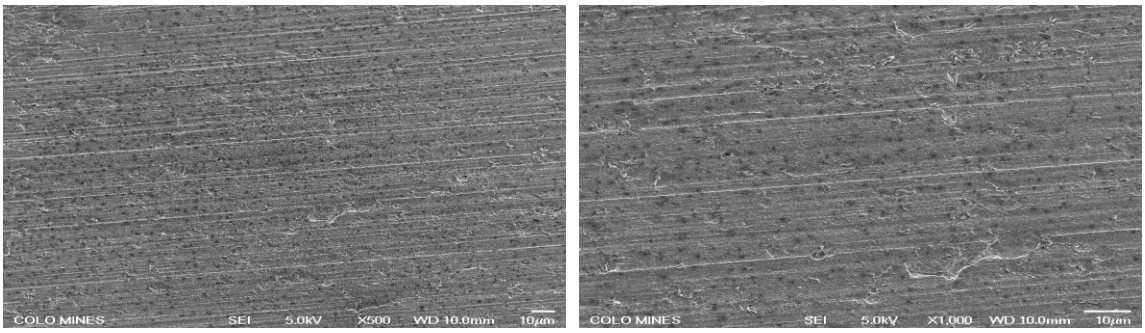

(c) **(b)**

Figure 4.43 FESEM of API X70 steel in modified Postgate B media inoculated with SRB removed after 10 days of immersion and cleaned according to ASTM G1 Standard pitted area (a) 10,000x (b) 20,000x and un-pitted (c) 500x (d) 1,000x magnification

The API X52 and API X70 steel electrodes from both the inoculated and control experiments were cleaned according to ASTM G1 Standard Practice (ASTM 2003), rinsed with DI water and 200 proof absolute ethanol, dried with forced air, and held in a low humidity atmosphere. The microscopy subsequently conducted was intended to inspect the morphology of the corrosion damage on the surface of the electrode. The relationship between the observed corrosion and the metallurgy of the steels was also evaluated.

The cleaned steel electrodes were imaged at low magnification in Figure 4.47. Pitting is not apparent on these images. It is important to note, however, that the prominent pitting observed on the API X70 steel electrode in Figure 4.37(b) is not displayed in Figure 4.47(b). Inspection of the cleaned surface of the API X52 steel electrode is presented in Figure 4.48. Images in Figure 4.48(a) and (b) are representative of the rougher (more corroded) areas of the electrode. Images in Figure 4.48(c) and (d) are representative of the less rough (less corroded) areas. Corrosion appears to proceed with a general mode. Intergranular attack producing microstructural relief can clearly be observed in the Figure. The image in Figure 4.48(b) also exhibits etch pitting features previously examined. This observation of these features is consistent with the more corroded areas on the surface experiencing conditions that are more aggressive. The micrographs in Figure 4.48(c) and (d) were acquired from the less corroded areas. Uniaxial polishing marks are faint but evident and microstructural etching cannot be observed.

Microscopy of the cleaned API X70 steel electrode is presented in Figure 4.49. These images were acquired from the areas of the steel surface covered by the adherent iron sulfide layer. The images reveal less aggressive corrosion of the surface than observed for the areas of the electrode covered by the non-adherent corrosion layer. Images in Figure 4.49 (a) and (b) are representative of the smoother (less corroded) areas of the electrode. Images in Figure 4.49 (c) and (d) are representative of the rougher (more corroded) areas. Some pitting attack and irregular corrosion can be observed on the surface. Polishing striations can be observed in all images in the Figure but are most pronounced in Figure 4.49 (a) and (b). Microstructural etching is not found.

The images in Figure 4.50 were acquired from the negative control API X52 steel electrode. The images in Figure 4.50 show polishing marks and slight pitting. Microstructural etching is absent. These images may be compared to those in Figure 4.48. Corrosion is far more pronounced in Figure 4.48 (a) and (b) than for Figure 4.50(a) and (b). Although the difference between Figure 4.48 (a) and (b) and Figure 4.50(a) and (b) is less pronounced, the surface imaged in Figure 4.48 (a) and (b) is rougher and more irregular.

The images in Figure 4.51 were acquired from the negative control API X70 steel electrode. The images in Figure 4.51 show polishing marks and slight pitting. Microstructural etching is absent. These images may be compared to those in Figure 4.49. Corrosion is far more pronounced in Figure 4.49 (a) and (b) than for Figure 4.51 (a) and (b). Little difference exists between Figure 4.49 (a) and (b) and Figure 4.51 (a) and (b). If any discernable difference exists, it is that the images in Figure 4.51(a) and (b) show more pitting than those in Figure 4.49 (a) and (b).

Linepipe Steel Exposed to SRB with Acetic Acid and Covered with Oil

An electrochemical corrosion study (described earlier in this Chapter) consisting of four experiments was conducted to evaluate the influence of an isolated SRB culture containing species grouping with *Clostridium*

sp. and *Desulfosporosinus sp.* on corrosion of API X52 and API X70 linepipe steels. The first two corrosion experiments were conducted in a modified Postgate B growth media containing 2 vol. pct. ethanol added as the microbial carbon source. One experiment was assembled with a working electrode fabricated from API X52 steel. The other experiment was assembled with a working electrode fabricated from API X70 steel. The second two electrochemical immersions tests were conducted in a modified Postgate B growth media containing one gram per liter acetic acid added as the microbial carbon source. One experiment was assembled with a working electrode fabricated from API X52 steel. The other experiment was assembled with a working electrode fabricated from API X70 steel. After completion of electrochemical testing, the working electrodes from all four cells were removed from the testing media for microscopic inspection. The specimens were imaged after cleaning according to ASTM G1 Standard Practice (ASTM 2003).

Iron sulfide layers of varying thickness were observed to cover the surface of the working electrode when they were removed from the corrosion cells. The API X52 and API X70 steel electrodes from the four experiments were cleaned according to ASTM G1 Standard Practice (ASTM 2003), rinsed with DI water and 200 proof absolute ethanol, dried with forced air, and held in a low humidity atmosphere. The microscopy subsequently conducted was intended to inspect the morphology of the corrosion damage on the surface of the electrode. The relationship between the observed corrosion and the microstructure of the steels was also evaluated.

The cleaned steel electrodes were imaged at low magnification in Figure 4.52. It is important to note that the prominent pitting observed on the API X70 steel electrode in Figure 4.37 (b) is not displayed in Figure 4.52 (b) or (d).

Inspection of the cleaned surface of the API X52 steel electrode from the ethanol experiment is presented in Figure 4.53. Corrosion was found to be uniform across the electrode surface. Images in Figure 4.53 are representative of the overwhelming majority of the electrode surface. Corrosion appears to proceed with a generally uniform mode. Intergranular attack can be observed in the Figure; however, strong dissolution of ferrite grains is observed. This morphology suggests that conditions were far more corrosive when an oil covering was applied to the system. The images in Figure 4.53 also exhibit a high density of the etch pitting features previously examined. Polishing marks are completely absent from the electrode surface.

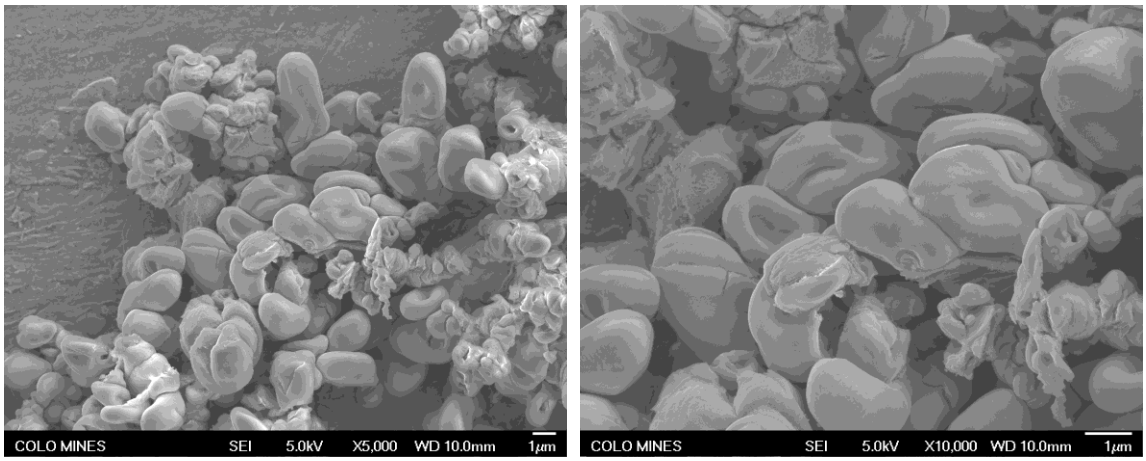

(a) (b)

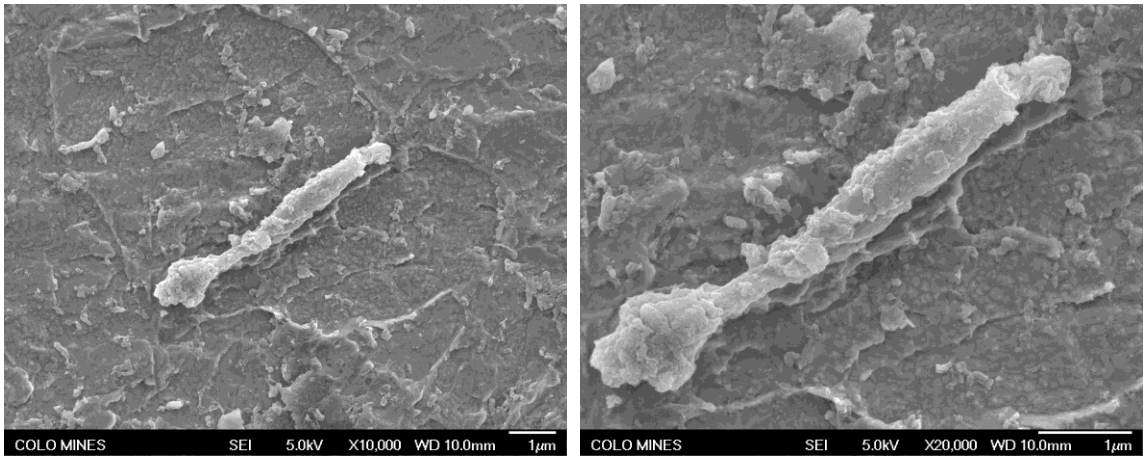

(c) (d)

Figure 4.44 Field emission SEM of *Clostridium sp*. (a) 5,000x (b) 10,000x and *Desulfosporosinus sp*. (c) 10,000x and (d) 20,000x magnification on API X52 steel immersed in modified Postgate B growth media containing one gram per liter acetic acid, inoculated with SRB, removed after approximately 10 days of immersion and rinsed with deiSonized water and ethanol

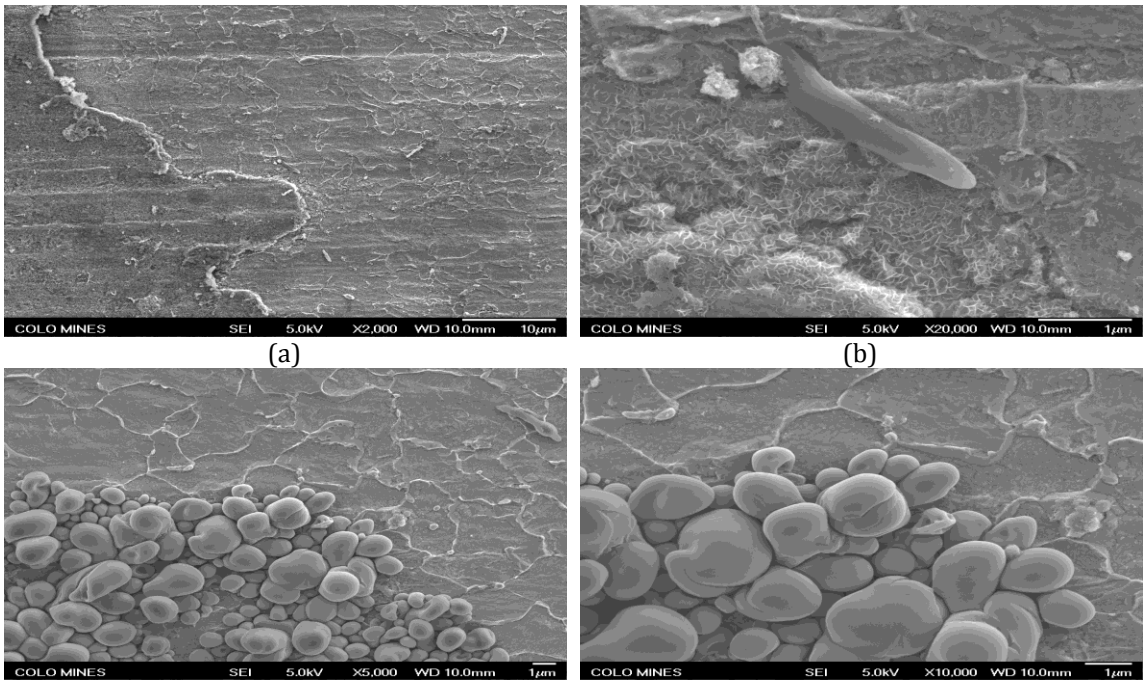

(a) (b)

(c) (d)

Figure 4.45 Field emission SEM of API X70 steel immersed in modified Postgate B growth media containing one gram per liter acetic acid, inoculated with SRB containing, removed after approximately 10 days of immersion and rinsed with DI water and ethanol location 1 (a) 2,000x (b) 20,000x (*Desulfosporosinus sp*.) and location 2 (*Clostridium sp.*) (c) 5,000x and (d) 10,000x magnification

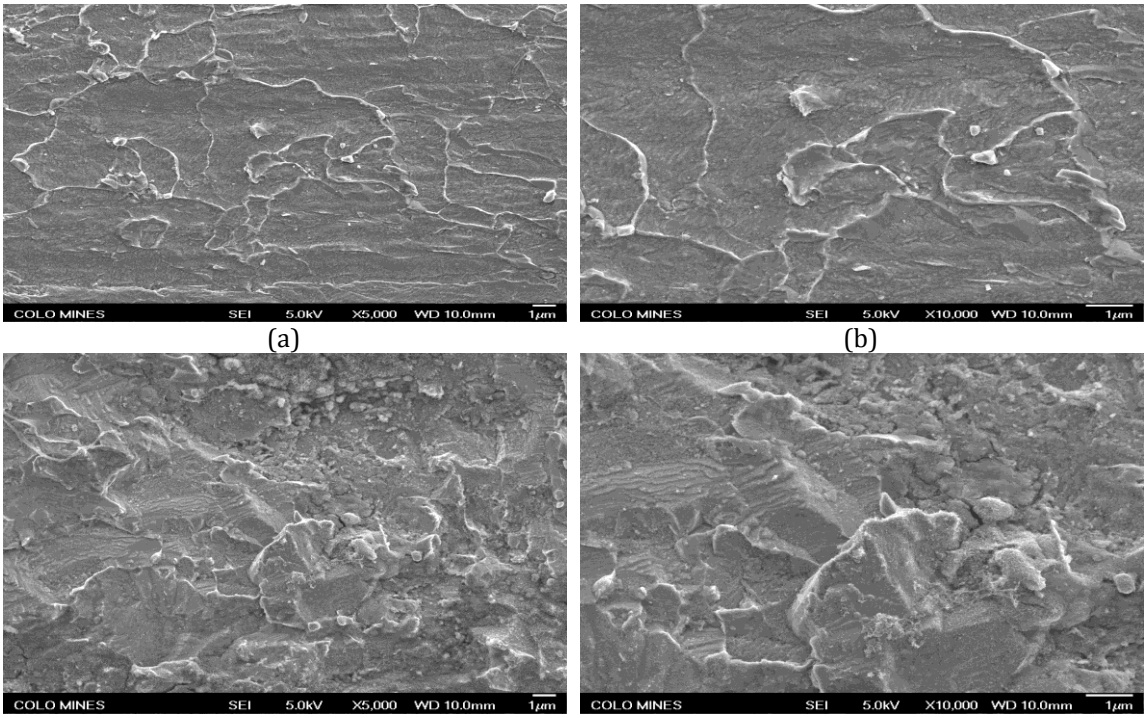

Figure 4.46 Field emission SEM of API X70 steel immersed in modified Postgate B growth media containing one gram per liter acetic acid, inoculated with SRB containing, removed after approximately 10 days of immersion and rinsed with DI water and ethanol location 1 (a) 5,000x (b) 10,000x and location 2 (c) 5,000x and (d) 10,000x magnification

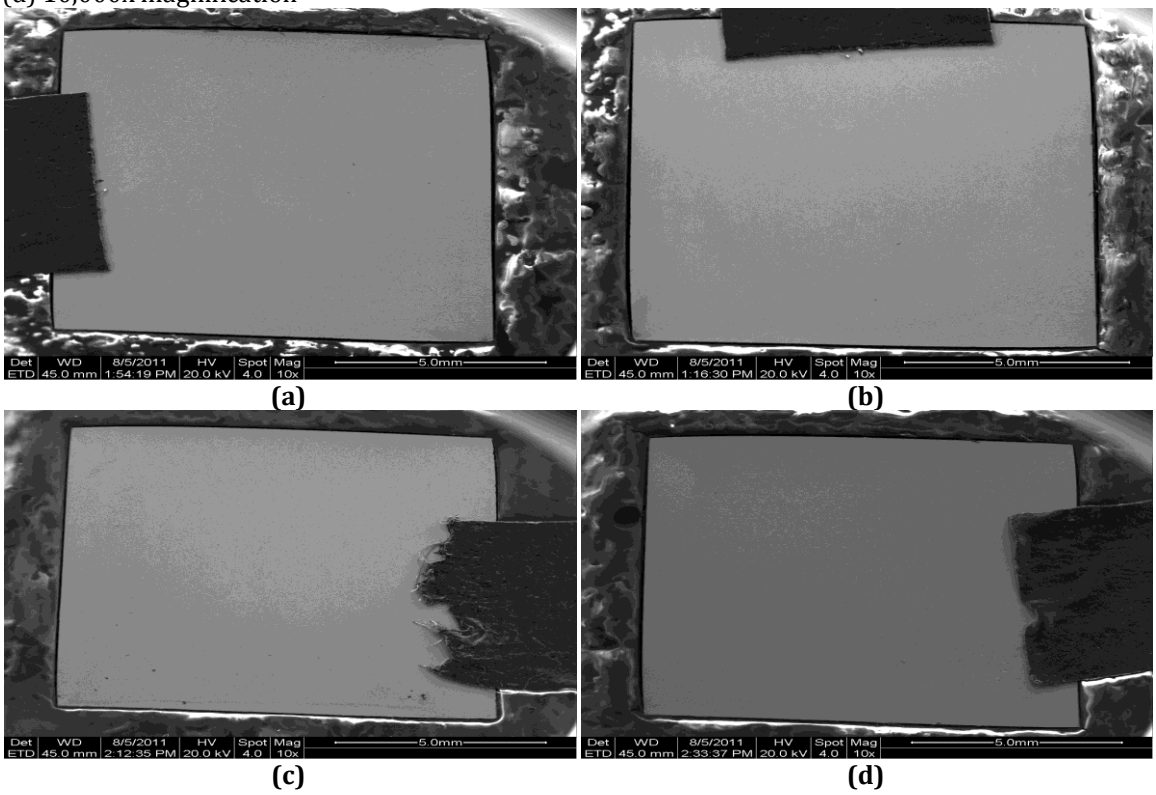

Figure 4.47 SEM of (a) API X52 steel exposed to an SRB consortium (b) API X70 steel exposed to SRB (c) API X52 steel negative control (d) API X70 steel negative control removed from modified Postgate B media with

one gram per liter acetic acid after approximately 10 days of immersion and cleaned according to ASTM G1 Standard Practice

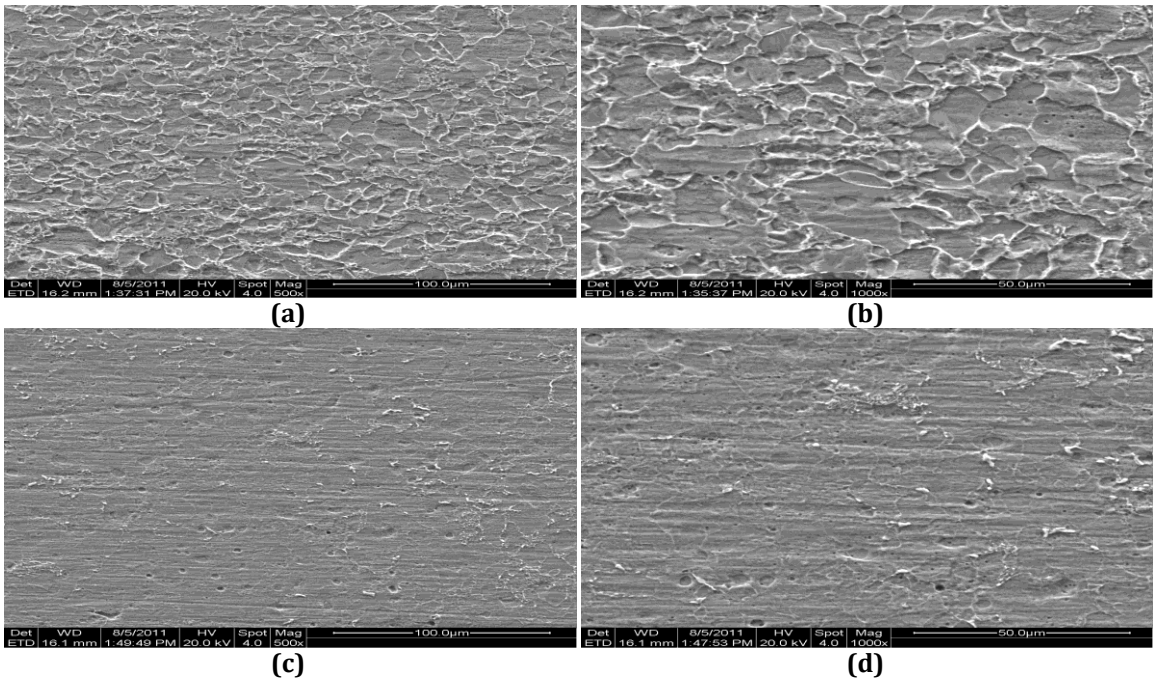

Figure 4.48 Representative SEM micrographs of API X52 steel immersed in modified Postgate B growth media containing one gram per liter acetic acid, inoculated with SRB, removed after approximately 10 days of immersion and cleaned according to ASTM G1 Standard Practice at location 1 (a) 500x and (b) 1,000x and location 2 (c) 500x and (d) 1,000x magnification

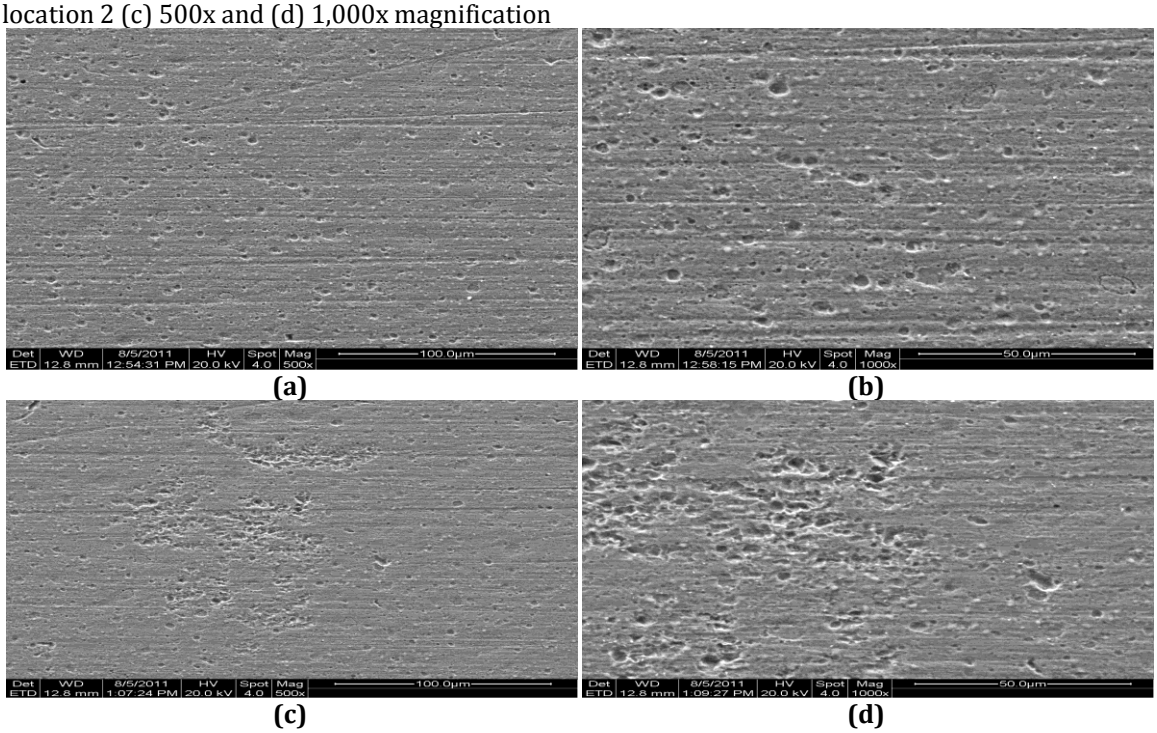

Figure 4.49 Representative SEM of API X70 steel immersed in modified Postgate B growth media containing one gram per liter acetic acid inoculated with SRB removed after approximately 10 days of immersion and cleaned according to ASTM G1 Standard Practice at (a) 500x (b) 1,000x and location 2 (c) 500x and (d) 1,000x magnification

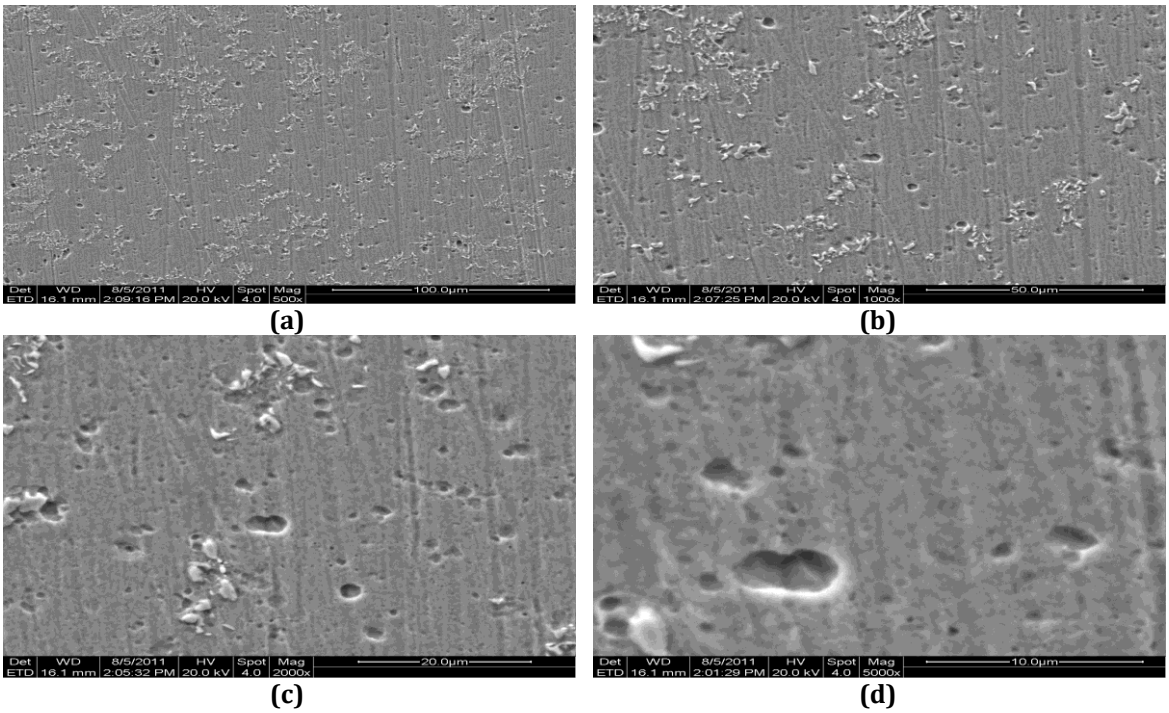

Figure 4.50 Representative SEM of API X52 steel immersed in modified Postgate B growth media containing one gram per liter acetic acid, removed after approximately 10 days of immersion and cleaned according to ASTM G1 Standard Practice at (a) 500x (b) 1,000x (c) 2,000x and (d) 5,000x magnification

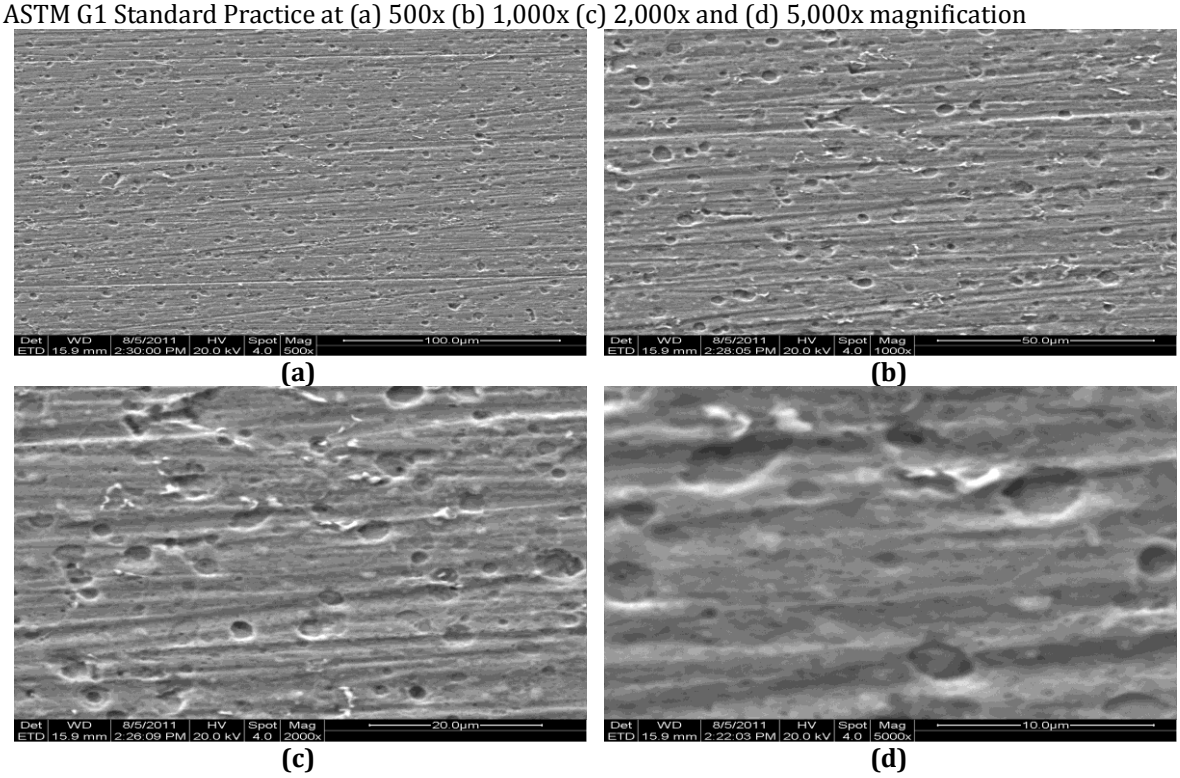

Figure 4.51 Representative SEM of API X70 steel immersed in sterile modified Postgate B growth media containing one gram per liter acetic acid, removed after approximately 10 days of immersion and cleaned according to ASTM G1 Standard Practice at (a) 500x (b) 1,000x (c) 2,000x and (d) 5,000x magnification

Inspection of the cleaned surface of the API X70 steel electrode from the ethanol experiment is presented in Figure 4.54. Microstructural etching is uniform across the surface of the electrode. Pitting was also observed across the entire electrode. Images in Figure 4.54 are representative of the overwhelming majority of the electrode surface. Intergranular attack can be observed in the Figure. Dissolution of ferrite grains may also be present. Again, conditions appear to have been more corrosive during this experiment when compared to earlier inoculated API X70 steel experiments [Figure 4.42 and Figure 4.49]. Polishing marks are completely absent from the electrode surface.

Inspection of the cleaned surface of the API X52 steel electrode from the acetic acid experiment is presented in Figure 4.55 and Figure 4.56. Corrosion was found to be fairly uniform across the electrode surface. Images in Figure 4.55 are representative of the vast majority of the electrode surface. Corrosion appears to proceed with a generally uniform mode. Strong microstructural etching can be observed in the Figure. The images in Figure 4.55 also exhibit a high density of the etch pitting features previously examined. Polishing marks are completely absent from the electrode surface. Images in Figure 4.56 are representative of some localized areas on the electrode surface that seem to have experienced accelerated attack. The surface topography is more irregular. Intergranular attack producing microstructural relief can be observed in the Figure although significant dissolution of the ferrite grains seems to have occurred. Corrosion of API X52 steel seems to be most severe in Figure 4.56, followed by Figure 4.53 and least severe in Figure 4.55 when comparing the oil experiments. Compared to the previous API X52 steel experiments shown in Figure 4.39 and Figure 4.48, the images in Figure 4.53, Figure 4.55 and Figure 4.56 all suggest more aggressive environments.

Inspection of the cleaned surface of the API X70 steel electrode from the acetic acid is presented in Figure 4.57. Corrosion was found to be remarkably uniform across the electrode surface. Images in Figure 4.57 are representative of the overwhelming majority of the electrode surface. Corrosion appears to proceed with a generally uniform mode. Intergranular attack can be observed in the Figure; however strong dissolution of ferrite grains is also observed. This morphology suggests that conditions were far more corrosive during this experiment. Polishing marks are completely absent from the electrode surface. The images in Figure 4.57 demonstrate the most pronounced attack on an API X70 steel electrodes and the only instance without sites of localized corrosion.

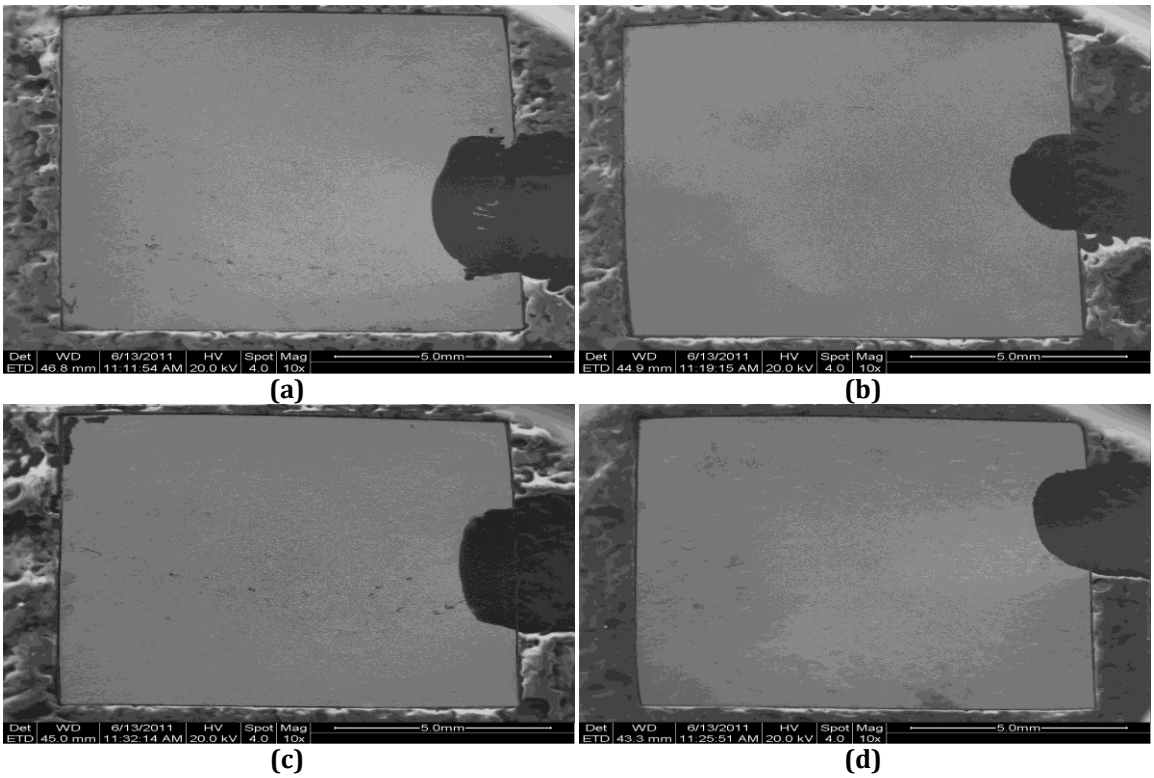

Figure 4.52 SEM of (a) API X52 steel immersed with two vol. pct. ethanol, (b) API X70 steel immersed with two vol. pct. ethanol (c) API X52 steel immersed with one gram per liter acetic acid and (d) API X70 steel

immersed with one gram per liter acetic acid under oil in modified Postgate B media, inoculated with SRB, removed after approximately 10 days of immersion and cleaned according to ASTM G1 Standard Practice

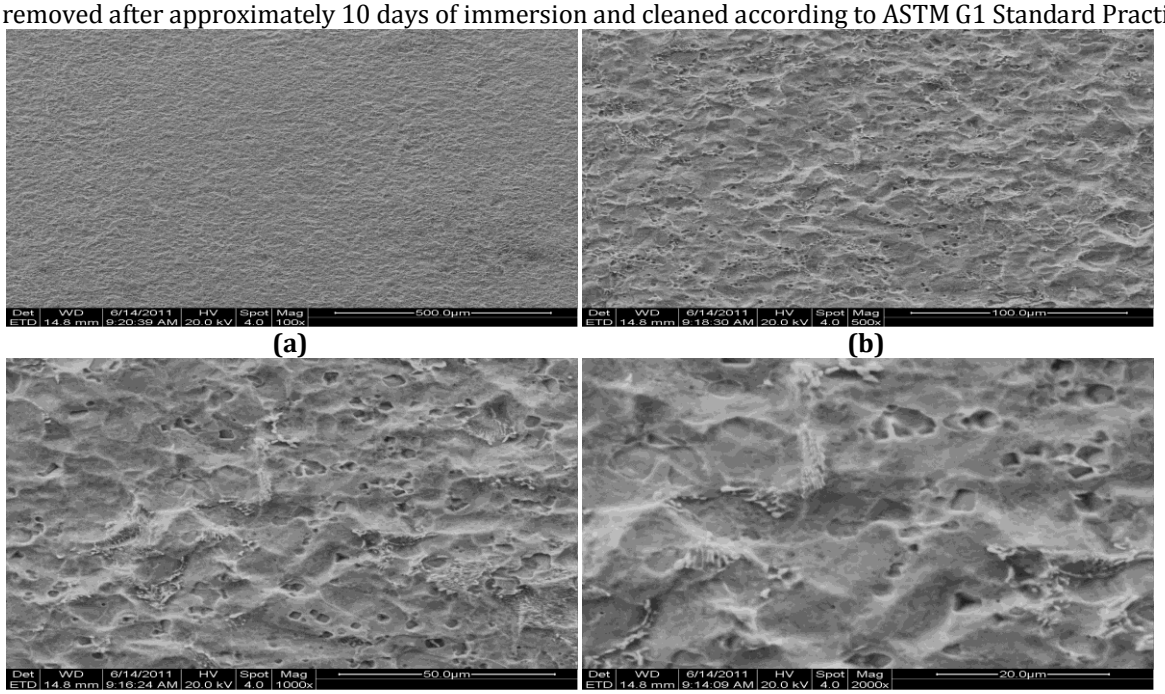

Figure 4.53 SEM of API X52 steel immersed under oil in modified Postgate B growth media containing two vol. pct. ethanol, inoculated with SRB, removed after approximately 10 days of immersion and cleaned according to ASTM G1 Standard Practice at (a) 100x (b) 500x (c) 1,000x and (d) 2,000x magnification

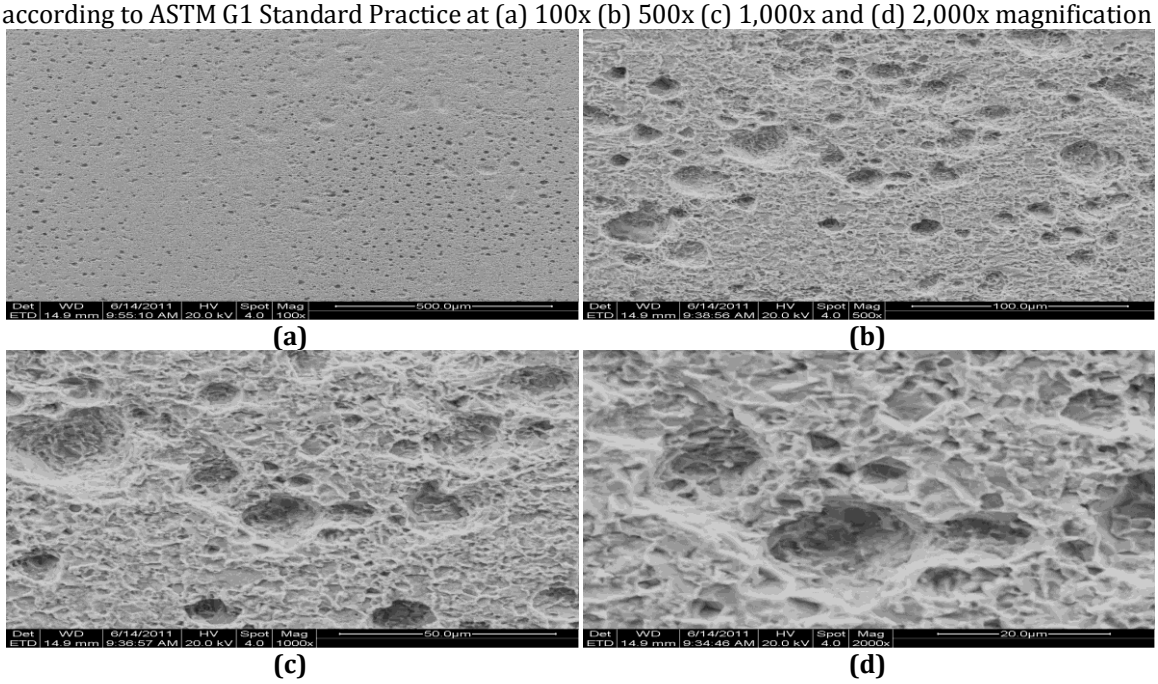

Figure 4.54 SEM of API X70 steel immersed under oil in modified Postgate B growth media containing two vol. pct. ethanol, inoculated with SRB, removed after approximately 10 days of immersion and cleaned according to ASTM G1 Standard Practice at (a) 100x (b) 500x (c) 1,000x and (d) 2,000x magnification

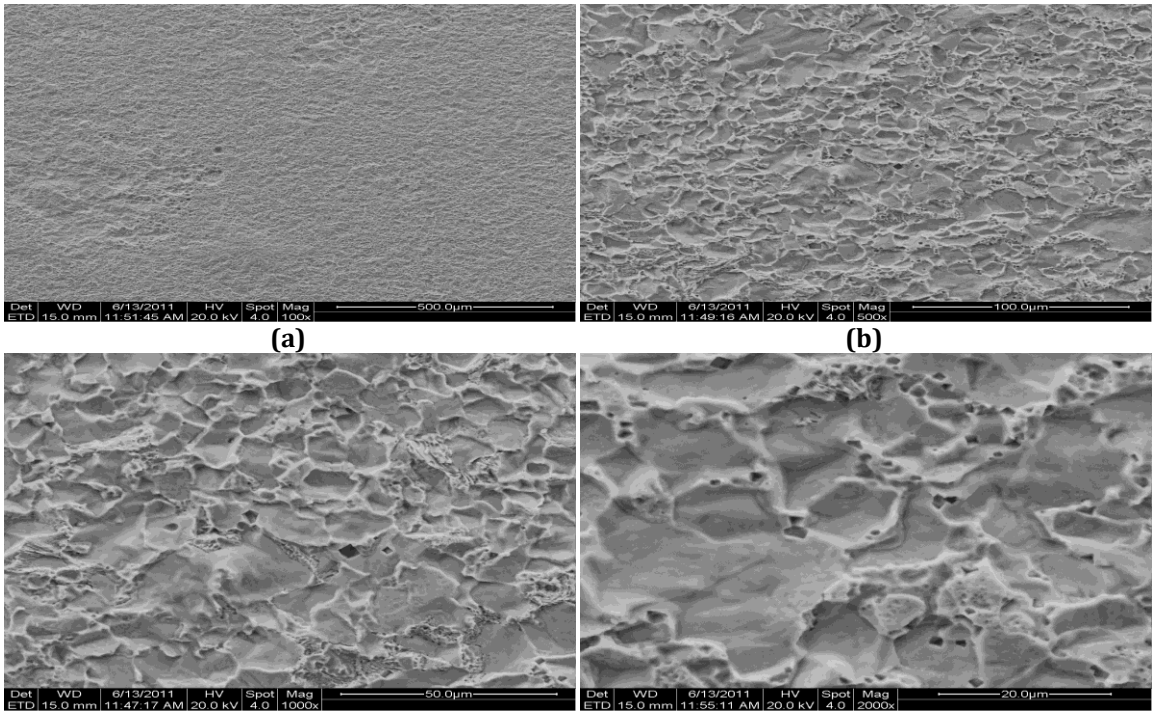

(a) **(b)**

(c) **(d)**

Figure 4.55 Representative SEM of API X52 steel immersed under oil in modified Postgate B growth media containing one gram per liter acetic acid, inoculated with SRB, removed after approximately 10 days of immersion and cleaned according to ASTM G1 Standard Practice at (a) 100x (b) 500x (c) 1,000x and (d) 2,000x magnification

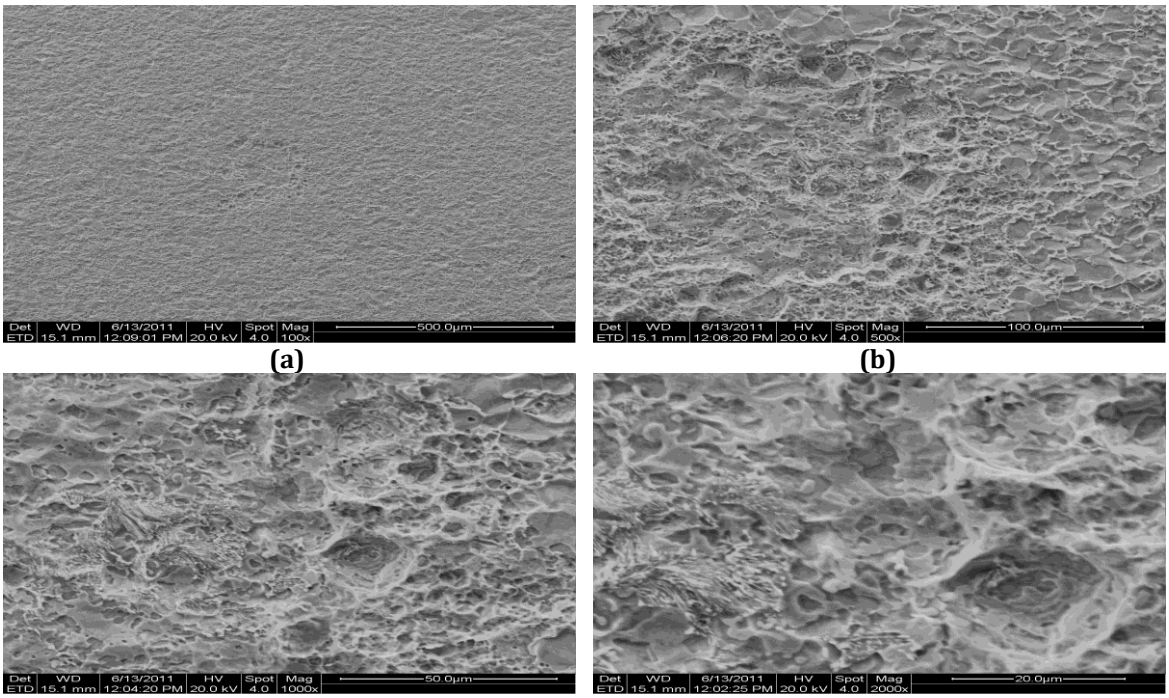

(a) **(b)**

(c) **(d)**

Figure 4.56 SEM of localized areas displaying more aggressive attack on API X52 steel immersed under oil in modified Postgate B growth media containing one gram per liter acetic acid, inoculated with SRB, removed after approximately 10 days of immersion and cleaned according to ASTM G1 Standard Practice at (a) 100x (b) 500x (c) 1,000x and (d) 2,000x magnification

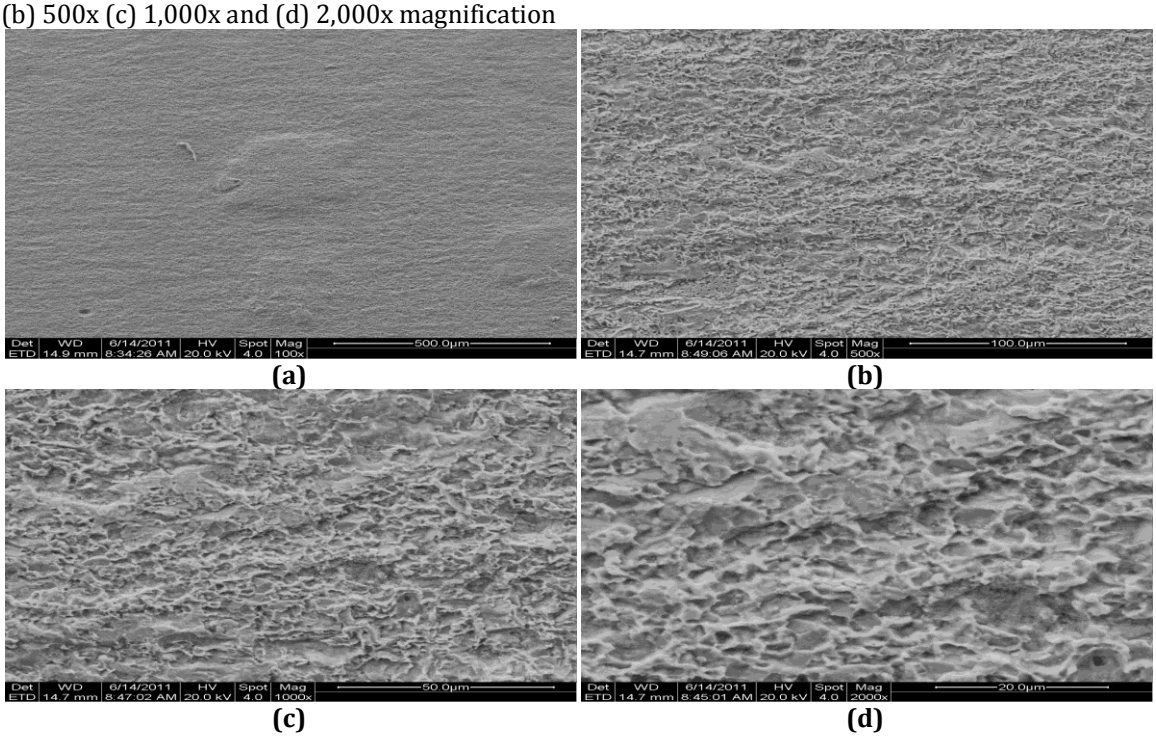

Figure 4.57 Representative SEM of API X70 steel immersed under oil in modified Postgate B growth media containing one gram per liter acetic acid, inoculated with removed after approximately 10 days of immersion and cleaned according to ASTM G1 Standard Practice at (a) 100x (b) 500x (c) 1,000x and (d) 2,000x magnification.

Linepipe Steel Exposed to Acetic APB

An electrochemical corrosion study (described earlier in this Chapter) was conducted to evaluate the influence of an isolated *Acetobacter aceti* culture on the corrosion of API X52 and API X70 linepipe steels. The electrochemical immersions tests were conducted in a modified growth media containing 5 vol. pct. ethanol added as the microbial carbon source. After completion of electrochemical testing, the working electrodes from the inoculated corrosion cells were removed from the testing media and prepared for microscopic inspection. The specimens were imaged first as recovered from the corrosion cell, next after rinsing with DI water, and finally after cleaning according to ASTM G1 Standard Practice (ASTM 2003).

The API X52 steel working electrode was first imaged prior to cleaning. The surface of the electrode is displayed in Figure 4.58 (a). This image shows coverage of the steel surface with a thick, coherent layer of corrosion product and biofilm. This morphology is representative of the entire electrode surface. The corrosion product can also be observed at high magnification at a different location in Figure 4.58 (b). Microbial tubercles and *Acetobacter aceti* cells can be distinguished in the image.

The surface of the API X70 steel electrode was also imaged prior to cleaning. A thick continuous layer of corrosion product and biofilm can be found on the steel surface. The general appearance of the surface is shown in Figure 4.59. Extensive biofilm development is evident. Higher resolution images show dense microbial colonization of the electrode surface. *Acetobacter aceti* cells can be distinguished.

Imaging of the API X50 steel after removal of the film with DI water revealed the presence of small well-defined pits. Two of these pits are shown in Figure 4.60. The morphology of the un-occluded pit is clearly shown in Figure 4.60 (a), (b) and (c). The size and geometry of the pit walls shown in the Figure are representative of other pits discovered on the surface. The pit morphology does not clearly indicate attack of microstructural features in the steel. A second pit can be found in Figure 4.60 (a), (b) and (d). This pit remains encrusted with biofilm and corrosion product. Both of the pits were presumably initially covered by microbial tubercles.

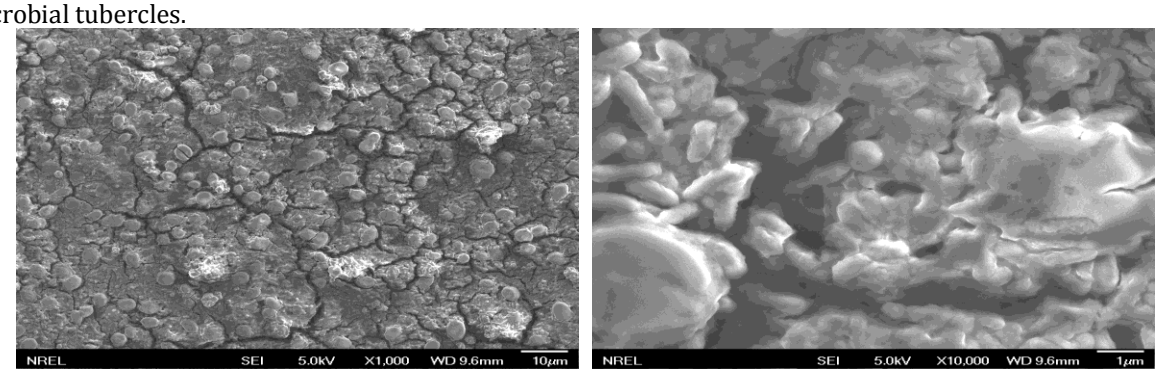

(a) **(b)**

Figure 4.58 Representative FESEM of biofilm and corrosion product on API X52 steel immersed growth media containing ethanol, inoculated with *Acetobacter aceti*, removed after 60 days of immersion at (a) 1,000x (b) 10,000x magnification

Both API X52 and API X70 steel electrodes were subsequently cleaned according to ASTM G1 Standard Practice (ASTM 2003), rinsed with DI water and 200 proof absolute ethanol, dried with forced air, and held in a low humidity atmosphere. The microscopy subsequently conducted was intended to inspect the morphology of the corrosion damage on the surface of the electrode. The relationship between the observed corrosion and the metallurgy of the steels was also evaluated.

The cleaned API X52 steel electrode was imaged in Figure 4.61 and Figure 4.62. The images presented in Figure 4.61 (a) and (b) are representative of the surface of the electrode. Interlamellar etching of pearlite is observed and pronounced etching around pearlite colonies can be found [Figure 4.61 (b)]. Instances of pitting, as observed previously in Figure 4.60, continued to be discovered. One pit in particular was capture and presented in Figure 4.61 (c) and (d). Sessile *Acetobacter aceti* cells can clearly be observed

inside the pit. Extra-polymeric microfilaments can be seen anchoring the cells to the interior walls and base of the pit. This suggests active colonization by the bacteria during the 60-day testing duration. Images shown in Figure 4.62 capture suspected galvanic corrosion of the ferrite matrix adjacent to an inclusion embedded in the surface of the electrode. The EDS spectra of the area adjacent to the suspected inclusion and the inclusion itself are presented in

Figure 4.63 (a) and (b), respectively. The baseline spectra of the area surrounding the inclusion indicate the presence of iron [

Figure 4.63 (a)]. The spectra recorded from the site of the inclusion indicate the presence of iron, manganese, sulfur, aluminum, and calcium. The presence of iron, manganese, sulfur, aluminum, and calcium are all consistent with the composition of an inclusion. Deposition of calcium is also known to occur in regions of localized higher pH. Higher pH could be produced near the inclusion by cathodic reaction processes.

The cleaned API X70 steel electrode was imaged in Figure 4.64 and Figure 4.65. The images presented in Figure 4.64 are representative of the surface of the electrode. Voids having approximately the same size and distribution of carbides as found in micrographs of polished API X70 steel are observed in the images. This correlation suggests galvanic attack of ferrite adjacent to carbides and carbide fall-out. Instances of pitting, similar to those previously observed in Figure 4.60 and Figure 4.61 were discovered. Images of several pits were captured and presented in Figure 4.65. All of the pits shown in the Figure are incrusted with biofilm and *Acetobacter aceti* cells. These observations further suggest colonization by the bacteria during the 60-day testing duration.

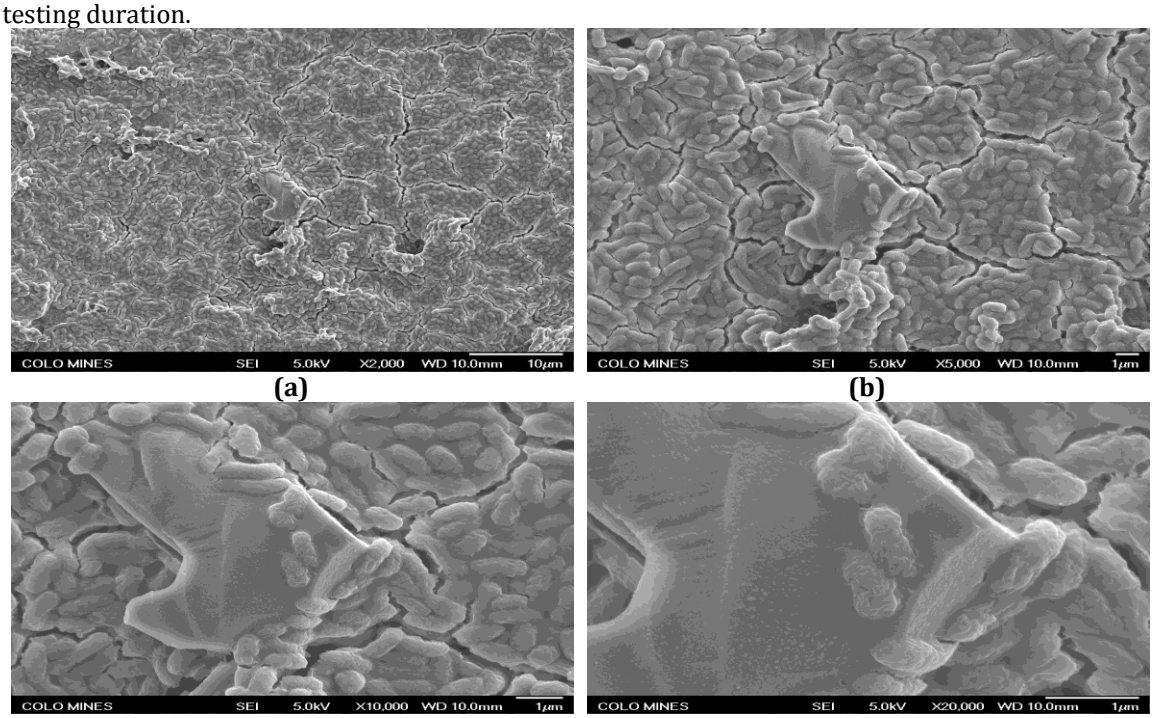

Figure 4.59 Representative field emission scanning electron micrographs of biofilm and corrosion product on API X70 steel immersed growth media containing five vol. pct. ethanol, inoculated with *Acetobacter aceti*, removed after 60 days of immersion at (a) 2,000x (b) 5,000x (c) 10,000x and (d) 20,000x magnification

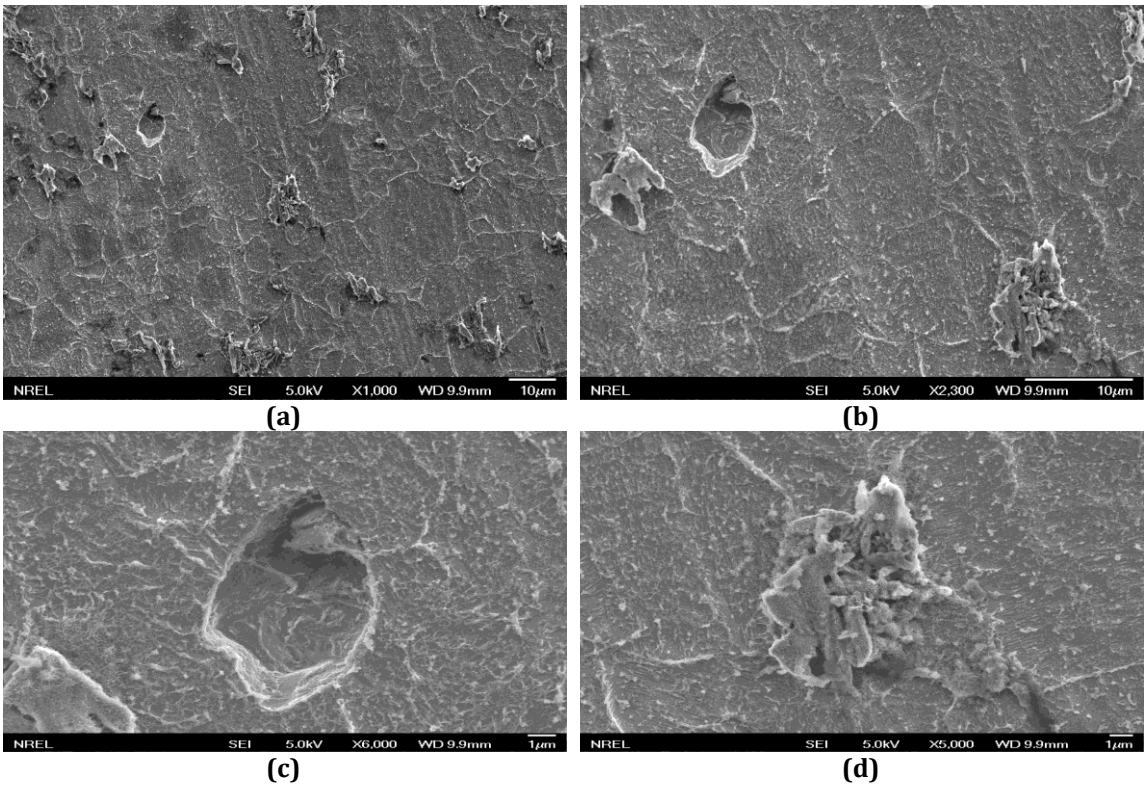

Figure 4.60 FESEM of API X52 steel in APB media inoculated with ethanol and inoculated with *Acetobacter aceti* removed after 60 days of immersion and rinsed with DI water (a) 1,000x (b) 2,300x (c) 6,000x and (d) 5,000x magnification

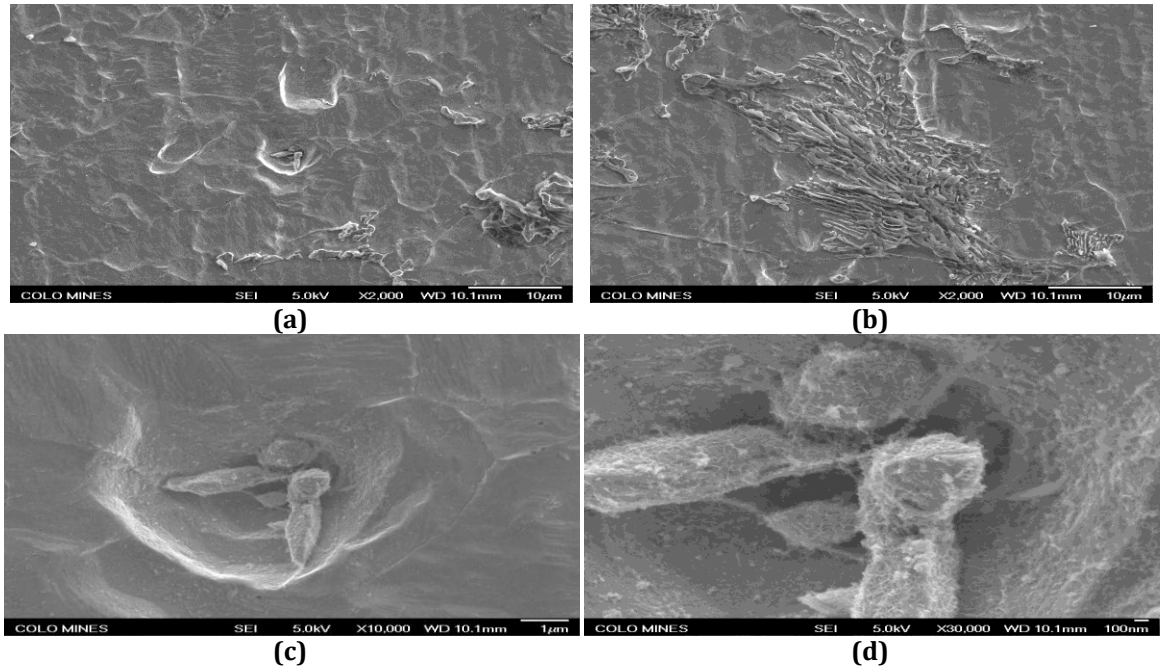

Figure 4.61 FESEM of API X52 steel in APB media inoculated with ethanol and inoculated with *Acetobacter aceti* removed after 60 days of immersion cleaned according to ASTM G1 Standard Practice (a) 10,000x (b) 30,000x

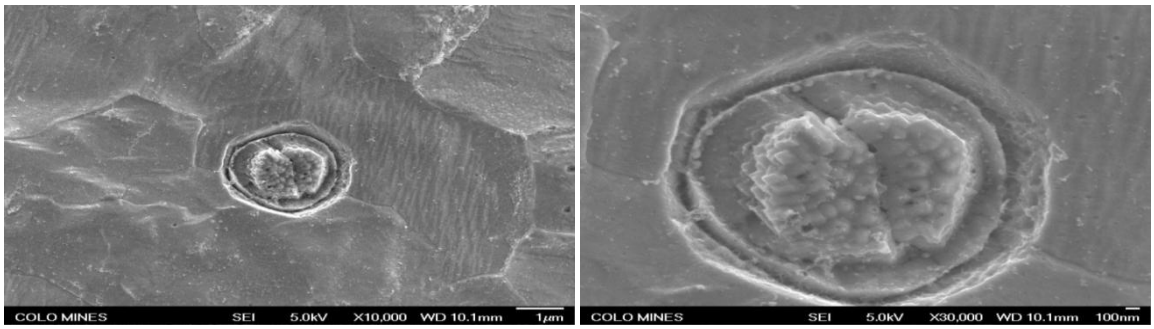

(a) **(b)**

Figure 4.62 FESEM of API X52 steel in APB media inoculated with ethanol and inoculated with *Acetobacter aceti* removed after 60 days of immersion cleaned according to ASTM G1 Standard Practice (a) 10,000x (b) 30,000x

MIC Mechanical Testing Study

In addition to electrochemical testing and electron microscopy of the electrochemical working electrodes, mechanical testing studies were performed. These were intended to investigate environmental cracking of the selected steels in the APB and SRB media. The multi-specimen bend testing method (MSBT) method was employed to screen for crack initiation and embrittlement. Additional tensile testing of corroded specimens was conducted to provide investigate any reduction of mechanical properties due to exposure to the isolated cultures.

Multi-Specimen Bend Testing of Linepipe Steel Exposed to APB and SRB

The MSBT program was described in Chapter 3. Several API X70 and ASTM A36 steel bend specimens were cyclically loaded in a four-point bend fixture for 500,000 cycles while immersed in the microbial media previously described. Several control bend specimens were placed in the bottom of the chamber and not loaded during immersion. One bend specimen was also cyclically loaded in air to 500,000 cycles. After loading to the predetermined number of cycles, these specimens were removed from the testing chamber and cleaned according to ASTM G1 Standard Practice. Areas of interest on the specimen were imaged using the ESEM. Tensile specimens were then machined from the original bend specimens. These tensile specimens were then pulled to failure under two different conditions (room temperature and submerged in liquid nitrogen) to evaluate any reduction in mechanical properties due to the immersion and/or cyclic loading.
Results from the MSBT study are presented in
Little variation was observed for mechanical properties measured for the tensile specimens tested in liquid nitrogen. Elongation for the API X70 steels, when tested in liquid nitrogen, regardless of any other conditions, varied from 2.4 to 8.6 pct. It should be noted that most specimens failed outside the measured gauge length. UTS for all API X70 tensile specimen was around 160-164 ksi, regardless of any experimental variable. The Ys was not measured for the tensile specimens submerged in liquid nitrogen.

Table 4.1. Test ID 0602 includes ASTM A 36 steel bend specimen exposed to Postgate B growth media with 2 vol. pct. ethanol and inoculated with SRB. Test ID 0505 includes steel bend specimen exposed to APB growth media with 5 vol. pct. ethanol and inoculated with APB as well as one bend specimen cyclically loaded in air. Test ID 0715 includes API X70 steel bend specimen exposed to Postgate B growth media with 2 vol. pct. ethanol and inoculated with SRB. Stress designation "Y" indicates that the bend specimen was cyclically loaded. Stress designation "N" indicates that the bend specimen was placed in the bottom of the chamber and not cyclically loaded. The condition designated as "room" indicates that the tensile specimen was loaded to failure at ambient temperature. The condition designated as "liq N_2" indicates that the tensile specimen was loaded to failure while submerged the gauge length was submerged in liquid nitrogen. The three mechanical properties evaluated in the study were total elongation, yield stress (Ys), and ultimate tensile stress (UTS).

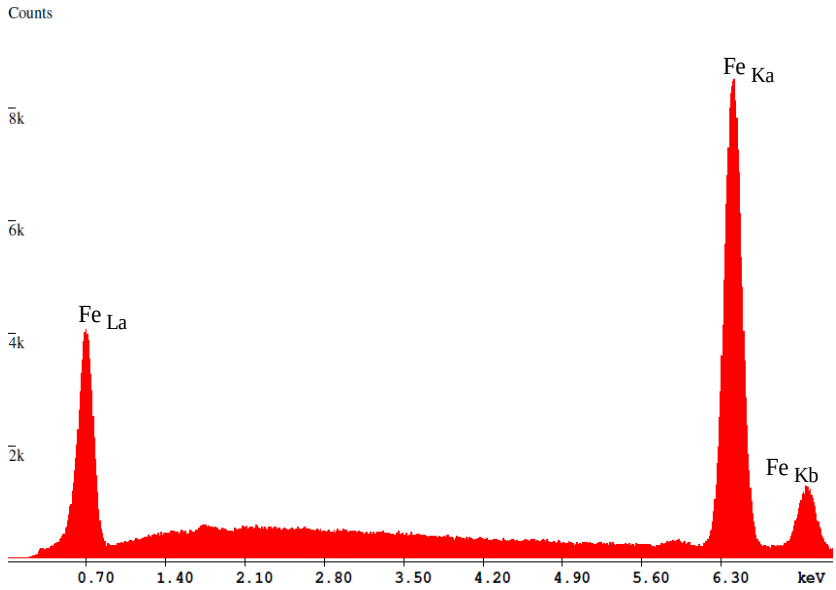

(a)

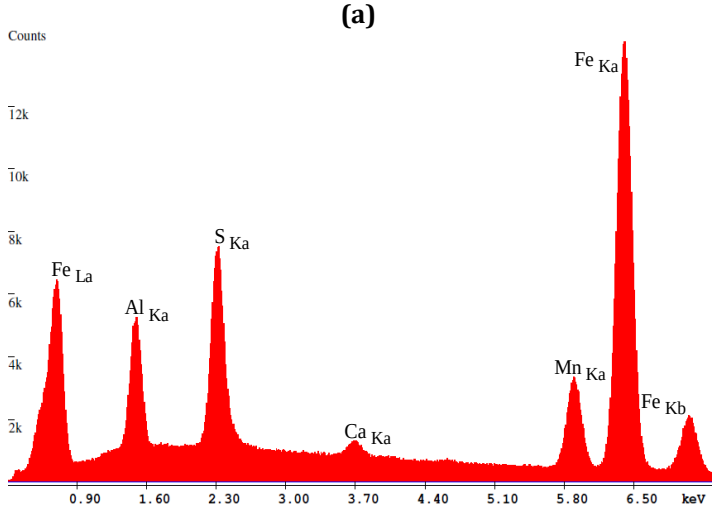

(b)

Figure 4.63 EDS of API X52 steel in APB media with ethanol and inoculated with *Acetobacter aceti* removed after 60 days of immersion cleaned according to ASTM G1 Standard Practice acquired (a) adjacent to inclusion (b) on inclusion shown in Figure 4.62

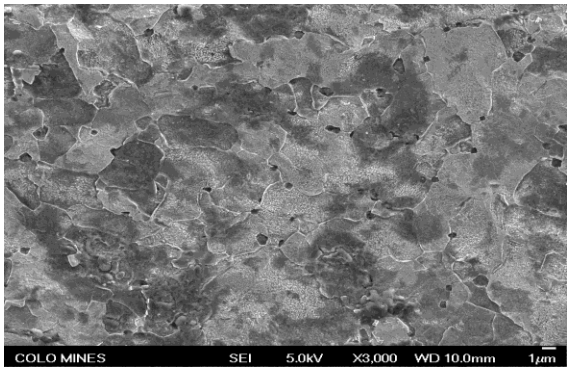

(a)

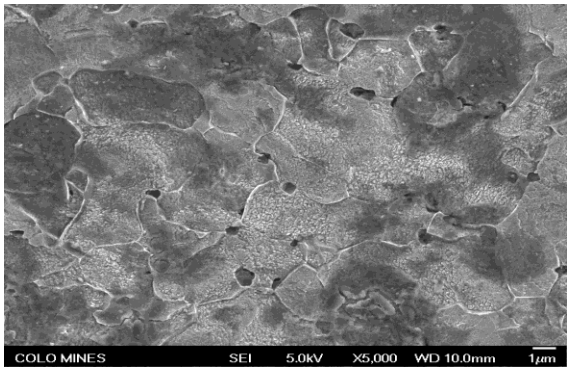

(b)

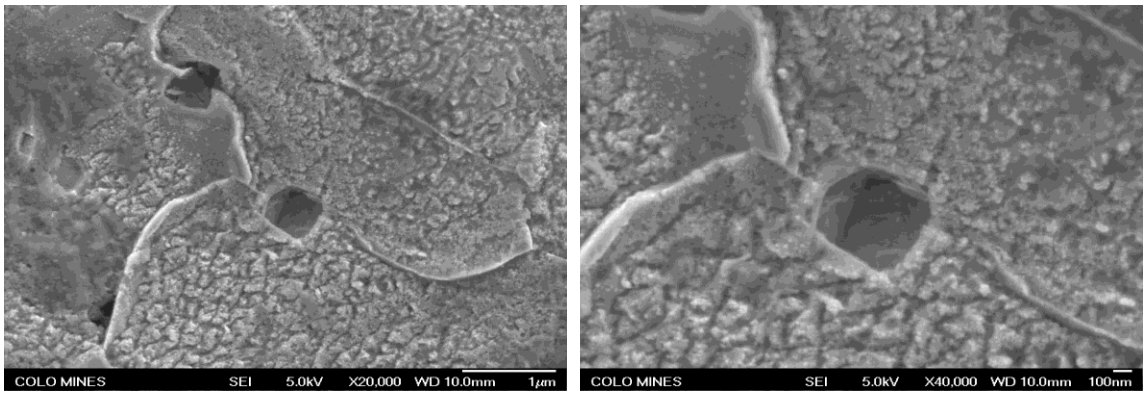

(c) **(d)**

Figure 4.64 Representative field emission scanning electron micrographs of API X70 steel immersed growth media containing five vol. pct. ethanol, inoculated with *Acetobacter aceti*, removed after 60 days of immersion at (a) 3,000x (b) 5,000x (c) 20,000x and (d) 40,000x magnification

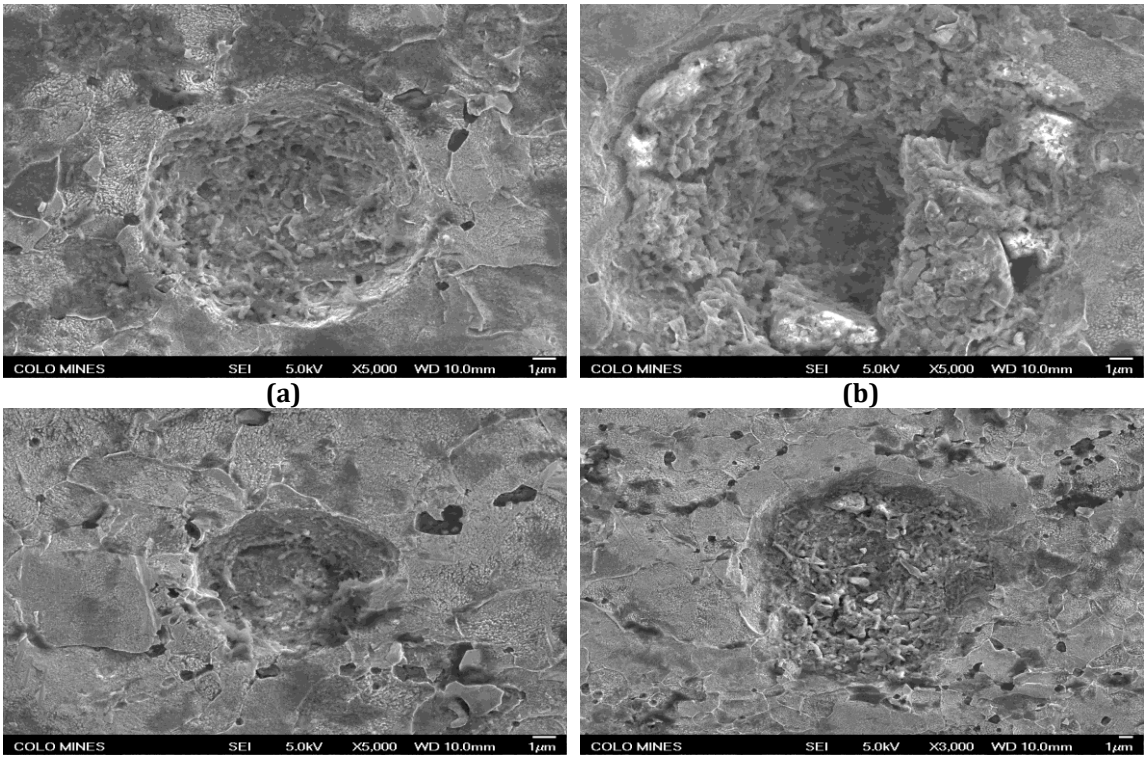

(a) **(b)**

(c) **(d)**

Figure 4.65 Field emission scanning electron micrographs of pits on API X70 steel immersed growth media containing five vol. pct. ethanol, inoculated with *Acetobacter aceti*, removed after 60 days of immersion at (a) – (c) 5,000x and (d) 3,000x

Mechanical properties remain very consistent for ASTM A36 steel tensile specimens tested in air. Elongation for the steels, regardless of any other conditions, remained near 30 pct. The Ys for all ASTM A36 tensile specimen was around 43-44 ksi, regardless of any experimental variable. UTS for all ASTM A36 tensile specimen was around 66-68 ksi, regardless of any experimental variable.

More variation was observed for mechanical properties measured for the tensile specimens testing in liquid nitrogen. Elongation for the ASTM A36 steels, when tested in liquid nitrogen, regardless of any other conditions, varied from 5.7 to 11.3 pct. The average elongations for the specimens immersed in the SRB and ethanol media was 5.8 pct. The average elongations for the specimens immersed in the APB and ethanol

media was 9.3 pct. The elongation for the specimen cyclically loaded in air was 11.3 pct. These results may indicate an alteration of mechanical properties due to immersion in the SRB and to a lesser extend APB media. It should be noted that most specimens failed outside the measured gauge length. Cyclic loading did not seem to affect total elongation. The UTS for all but two ASTM A36 tensile specimens was around 127-132 ksi. Tensile specimens 0602-1b and 0602-2b exhibit an experimental UTS of 98.4 and 96.4 ksi, respectively. It is not apparent why these two specimen exhibited lower properties, and furthermore, why the properties grouped together. The Ys was not measured for the tensile specimens submerged in liquid nitrogen.

Mechanical properties remain very consistent for the API X70 steel tensile specimens tested in air. Elongation for the steels, regardless of any other conditions, remained around 19-22 pct. The Ys for all API X70 steel tensile specimen was around 82-87 ksi, regardless of any experimental variable. UTS for all API X70 steel tensile specimen was around 92-93 ksi, regardless of any experimental variable.

Little variation was observed for mechanical properties measured for the tensile specimens testing in liquid nitrogen. Elongation for the API X70 steels, when tested in liquid nitrogen, regardless of any other conditions, varied from 1.0 to 16.7 pct. It should be noted that most specimens failed outside the measured gauge length. UTS for all API X70 tensile specimen was around 138-155 ksi, regardless of any experimental variable. The Ys was not measured for the tensile specimens submerged in liquid nitrogen.

Multi-Specimen Bend Testing of API X70 Steel Exposed to SRB

The set of API X70 steel tensile tests described in Chapter 3 were placed in the bottom of a chamber containing SRB and ethanol media duration bend testing. Some of there were pulled to failure under the two different conditions (room temperature and submerged in liquid nitrogen) immediately after removal from the microbial media. Others were pulled to failure under the two different conditions (room temperature and submerged in liquid nitrogen) 12 days after removal. Control specimens were also tested.

Microscopy did not yield any evidence of cracking. Results from the tensile study is presented in

Table 4.2. The three mechanical properties evaluated in the study were total elongation, Ys, and UTS.

Mechanical properties remain very consistent for tensile specimens tested in air. Elongation for the API X70 steels, regardless of any other conditions, was around 18-24 pct. The Ys for all API X70 tensile specimen was around 81-83 ksi, regardless of any experimental variable. UTS for all API X70 tensile specimen was around 91-93 ksi, regardless of any experimental variable.

Little variation was observed for mechanical properties measured for the tensile specimens tested in liquid nitrogen. Elongation for the API X70 steels, when tested in liquid nitrogen, regardless of any other conditions, varied from 2.4 to 8.6 pct. It should be noted that most specimens failed outside the measured gauge length. UTS for all API X70 tensile specimen was around 160-164 ksi, regardless of any experimental variable. The Ys was not measured for the tensile specimens submerged in liquid nitrogen.

Table 4.1 Experimental Results from Multi-Specimen Bend Testing

Test ID	Bend ID	Media (type)	Innoc. (type)	Stress (Y/N)	Steel (type)	Tensile ID	Cond. (type)	Elong. (%)	YS (ksi)	UTS (ksi)
0602	1	SRB_2 % Eth.	SRB	N	A36	0602-1a	room	29.9	44.3	67.9
0602	1	SRB_2 % Eth.	SRB	N	A36	0602-1b	liq. N_2	5.7	---	98.4
0602	2	SRB_2 % Eth.	SRB	Y	A36	0602-2a	room	31.0	44.9	68.0
0602	2	SRB_2 % Eth.	SRB	Y	A36	0602-2b	liq. N_2	7.9	---	96.4
0602	3	SRB_2 % Eth.	SRB	N	A36	0602-3a	room	33.3	44.4	67.7
0602	3	SRB_2 % Eth.	SRB	N	A36	0602-3b	liq. N_2	4.5	---	131.7
0602	4	SRB_2 % Eth.	SRB	Y	A36	0602-4a	room	33.6	45.9	68.0
0602	4	SRB_2 % Eth.	SRB	Y	A36	0602-4b	liq. N_2	5.0	---	128.4
0505	1	APB_5 % Eth.	APB	Y	A36	0505-1a	room	30.2	44.3	68.7
0505	1	APB_5 % Eth.	APB	Y	A36	0505-1b	liq. N_2	7.7	---	127.9
0505	2	APB_5 % Eth.	APB	Y	A36	0505-2a	room	31.3	43.9	66.4
0505	2	APB_5 % Eth.	APB	Y	A36	0505-2b	liq. N_2	10.9	---	127.0
0505	3	Air	---	Y	A36	0505-3a	room	34.6	43.0	66.8
0505	3	Air	---	Y	A36	0505-3b	liq. N_2	11.3	---	131.7
0715	1	SRB_2 % Eth.	SRB	Y	X70	0715-1a	room	20.6	81.8	91.6
0715	1	SRB_2 % Eth.	SRB	Y	X70	0715-1b	liq. N_2	1.0	---	138.2
0715	2	SRB_2 % Eth.	SRB	Y	X70	0715-2a	room	22.2	82.0	93.1
0715	2	SRB_2 % Eth.	SRB	Y	X70	0715-2b	liq. N_2	16.7	---	154.6
0715	3	SRB_2 % Eth.	SRB	N	X70	0715-3a	room	19.8	87.0	92.3
0715	3	SRB_2 % Eth.	SRB	N	X70	0715-3b	liq. N_2	2.5	---	153.7
0715	6	SRB_2 % Eth.	SRB	N	X70	0715-6a	room	18.7	84.0	92.9
0715	6	SRB_2 % Eth.	SRB	N	X70	0715-6b	liq. N_2	9.4	---	150.9

Table 4.2 Experimental Results from Tensile Testing

Test ID	Tensile ID	Immers. (Y/N)	Delay (days)	Cond. (type)	Elong. (%)	YS (ksi)	UTS (ksi)
0715	T1	Y	0	room	23.0	81.3	91.0
0715	T2	Y	0	liq. N_2	2.4	---	164.5
0715	T3	Y	12	room	17.7	81.2	93.0
0715	T4	Y	12	liq. N_2	3.8	---	159.7
0715	T5	N	0	room	23.9	83.2	93.0
0715	T6	N	0	liq. N_2	8.6	---	164.4

CHAPTER 5 ANALYSIS AND SUMMARY

This investigation has evaluated the propensity for microbiologically influenced corrosion (MIC) in fuel grade ethanol (FGE) environments. Microbes were isolated from FGE infrastructure and grown in media containing ethanol and acetic acid as carbon sources. These environments were selected to simulate possible localized environments in FGE transportation systems and auxiliary equipment where conditions are ideal for growth. The experimental work in this thesis was directed to answer the question: *Can environments containing ethanol enhance susceptibility of steels to MIC?* Several subsidiary questions were listed to address this inquiry. Discussion of these questions is presented below.

What Forms of Corrosion are Likely?

Classic corrosion literature describes "The Eight Forms of Corrosion" as (1) uniform (general) (2) galvanic (3) crevice (4) pitting (5) intergranular (6) selective leaching (7) erosion corrosion and (8) stress corrosion (Fontana and Greene 1967). MIC is known to initiate or accelerate all of these. Electrochemical corrosion measurements and electron microscopy were conducted to evaluate which of these forms of corrosion occurred to API X52 and API X70 linepipe steels exposed to acid producing bacteria (APB) and sulfate-reducing bacteria (SRB).

Corrosion of Linepipe Steels by Acetic Acid Producing Bacteria

Electrochemical corrosion testing indicated that the applied acetic APB did not accelerate general corrosion rates of either API X70 or API X52 linepipe steels. Subsequent inspection of the working electrode with electron microscopy indicated the presence of microstructural etching and pitting of both steels. Pits on the API X52 steel were around 5 μm in diameter. Pits were circular to oval shaped and exhibited a "scoop-like" appearance. Pit to nearest pit distance generally varied from around 10 to 100 μm. Bimodal pitting was observed on the API X70 steel. The smaller pits were around 1 μm in diameter. These pits were polygonal, often rectangular. The pitting may be associated with carbides. Pit to nearest pit distance generally varied from around 5 to 10 μm. The majority of pits present along grain boundaries. The larger pits were around 10 μm in diameter and infrequently found on the surface. These pits were generally incrusted with microbial tubercles consisting of *Acetobacter aceti* and biofilm.

Corrosion of Linepipe Steels by Sulfate-Reducing Bacteria

Electrochemical corrosion testing indicated that the applied sulfate-reducing bacteria (SRB) accelerated general corrosion rates for both API X70 and API X52 linepipe steels. General corrosion rates increased from API X52 per constant (mpy) (Chapter 4) to higher recorded corrosion rate compared to the API X70 steel. The SRB with acetic acid experiments consistently induced higher corrosion rates in both steels than the SRB with ethanol experiments. Subsequent inspection of the electrode with electron microscopy indicated intergranular corrosion, dissolution of ferrite grains, etch-pitting of ferrite grains, and general pitting. General corrosion was dominate on the API X52 steel. The API X70 steel exhibited pitting, often in addition to general or irregular corrosion. Microstructural etching and intergranular attack was evident in every test on both steels. Etch-pitting and dissolution of ferrite grains was evident in localized areas experiencing particularly aggressive conditions.

Table 5.1 Corrosion Rates (CR) Measured by Polarization Resistance Method

	Maximum CR (mpy)		Final CR (mpy)	
	API X52	API X70	API X52	API X70
EtOH	66	25	36	3
HAc	112	95	63	39

What Corrosion Mechanisms Are Operating?

Corrosion mechanisms are the means by which materials are reduced to lower energy states. These pathways are governed by electrochemical thermodynamic and kinetic principles. The goal of fundamental

corrosion research is to improve understanding of corrosion mechanisms. Proposed corrosion mechanisms are based on the current state of knowledge reviewed in Chapter 2 in conjunction with experimental observations presented in Chapter 4.

Corrosion of Linepipe Steels by Acetic Acid Producing Bacteria

The observed pitting corrosion of linepipe steels exposed to APB culture is proposed to occur in

Corrosion initiation is driven by galvanic coupling between the ferrite matrix and a second phase particle.

The iron adjacent to the carbide becomes a local anode. The second phase particle and surrounding iron

Figure 5.1]. The rate of dissolution is dependent on the anode and cathode, the mixed potential assumed by the galvanic couple, the surface areas of the anode and cathode, and the availability of oxidizing species. Bacterial acetic acid production increases the supply of cathodic reactants. Ethanol is consumed by the acetic acid producing bacteria and metabolically converted to acetic acid. Acetic acid acts as a cathodic reactant according to the reactions:

$$H^+ + e^- \rightarrow \mathrm{H} \tag{5.1}$$

And

$$CH_3COOH + e^- \rightarrow CH_3COO^- + \mathrm{H} \tag{5.2}$$

Iron dissolution produces a crevice in the ferrite matrix adjacent to the second phase particle. A

this nature is observed adjacent to an inclusion on the API X52 steel electrode surface [

Figure 4.63]. The occluded nature of the crevice retards mass transport between the interior of the

crevice and the bulk solution. Autocatalytic pitting processes are initiated. These processes include

hydrolysis of the corrosion product, acidification of the pit interior, and chloride migration into the crevice.

Once a critical area of iron is dissolved adjacent to the carbide or inclusion, the particle delaminates from the

ferrite matrix and disperses into the bulk solution [

Figure 5.2]. Carbide fall-out is evidenced by the abundance of smaller, approximately 1 μm pits,

observed on the API X70 steel [Figure 4.64]. The bimodal distribution of pit sizes indicates that a minority of

the pits grow at a much higher rate. This elevated growth rate is due to the colonization of some of these pits

with *Acetobacter aceti*. Microbial acetic acid in the pit interiors and biofilm production over the surface of the

pits produces a concentration cell and local acidification. Exceptionally aggressive conditions lead to

accelerated pit growth [

Figure 5.3]. These larger, approximately 10 μm pits are observed on the surface, occluded with biofilm [Figure 4.65].

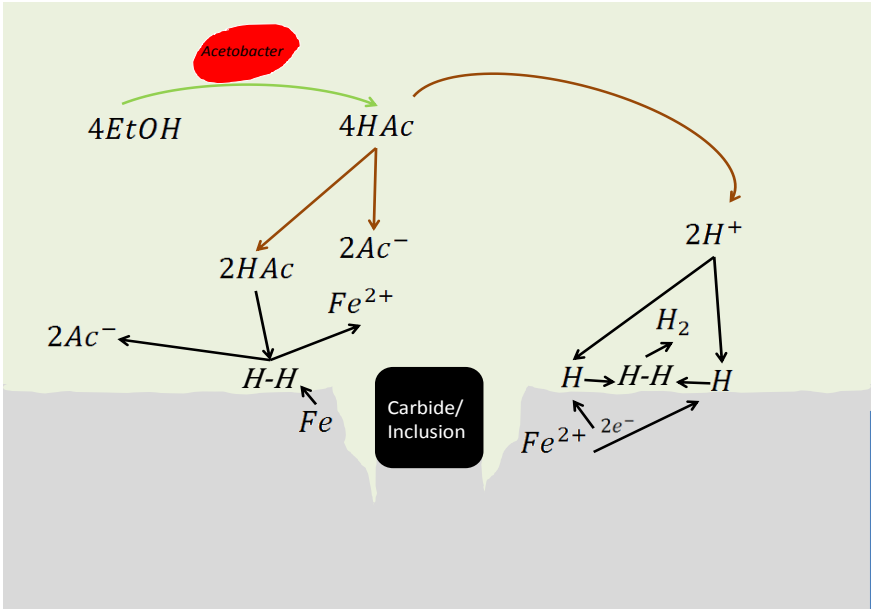

Figure 5.1 Stage 1 of proposed qualitative model for pitting corrosion mechanism for linepipe steels exposed to APB in growth media with 5 vol. pct. ethanol

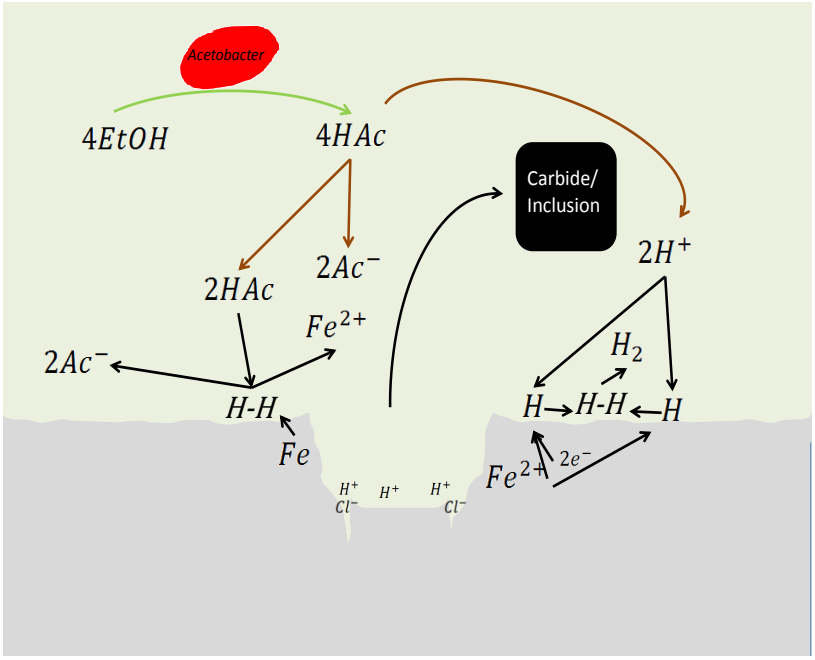

Figure 5.2 Stage 2 of proposed qualitative model for pitting corrosion mechanism for linepipe steels exposed to APB in growth media with 5 vol. pct. Ethanol

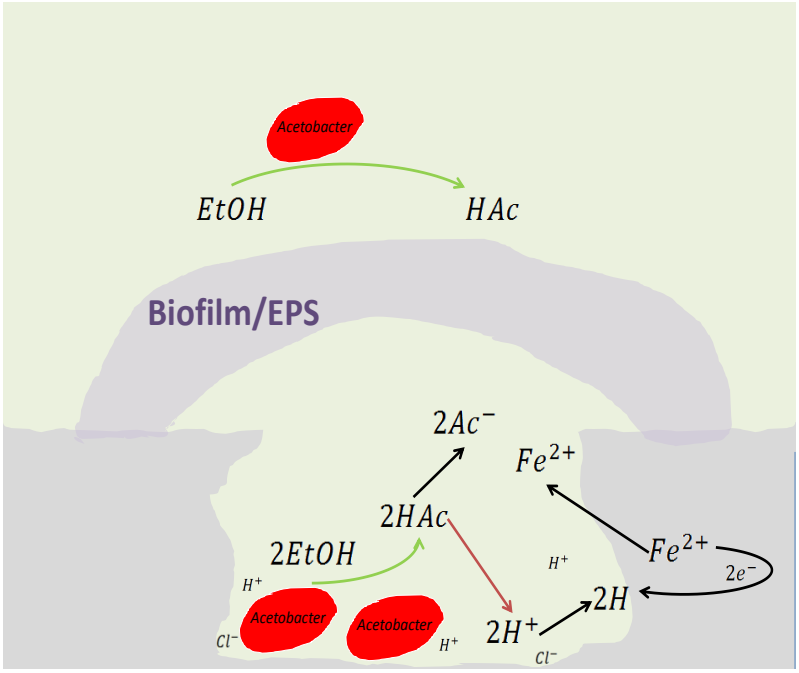

Figure 5.3 Stage 3 of proposed qualitative model for proposed pitting corrosion mechanism for linepipe steels exposed to APB in growth media with 5 vol. pct. ethanol

Corrosion of Linepipe Steels by Sulfate-Reducing Bacteria

Corrosion observed for the linepipe steels exposed to SRB in the presence of ethanol and acetic acid is proposed to be controlled by the evolution of the iron sulfide corrosion product layer residing on the metal surface. Furthermore, it is proposed that the integrity of this film is dependent on three main variables: the composition and microstructure of the steel, the presence of acetic acid, and microbial colonization of the film. It is also presumed that application of oil over the systems produces higher hydrogen sulfide concentration and that these higher concentrations were responsible for higher corrosion rates. As neither sulfide nor hydrogen sulfide measurements were taken, this relationship is not confirmed. Comparison of the three main variables is conducted; however, with special addition to the oil containing experiments as these were inoculated with the most similar cultures and were contained most uniformly.

The greater chemical and microstructural heterogeneity of the API X52 steel electrode presents an inherently less stable material with a greater susceptibility to corrosion. Variations in chemical composition and structure produce differences in electrochemical potential. These potential gradients allow for the type of galvanic coupling identified in the previous section. High material heterogeneity, therefore, corresponds to a high density of sites with potential for initiation of corrosion processes. When kinetic requirements for initiation of corrosion processes are met by microbial production of hydrogen sulfide, high corrosion rates commence. High corrosion rates of steel in hydrogen sulfide produce high concentrations of iron cations and sulfide anions. These precipitate (or form by solid-state reaction) to iron sulfide at high rates. This resulting bulky growth of the iron sulfide layer is known to produce high mechanical strains. Thick porous corrosion product is confirmed by visual inspection and high double layer capacitance (DLC). High corrosion rates also correspond to greater flux of corrosion reactants and products toward and away from the steel surface. High mechanical strains and diffusion of species through this layer are known to compromise the integrity of the film. This compromised integrity is demonstrated by sustained low charge-transfer (CTR) and polarization resistance (PR). Repassivation is not indicated by CTR or PR data.

The presence of trace acetic acid has recently been suggested to inhibit the protectiveness of iron corrosion product (Singer, Brown, et al. 2011). This inhibition of passivation is the case in the present system. CTR and PR are lower for both steels in acetic acid containing experiments when compared to those steels with ethanol. The oxidizing contribution of acetic acid in this system is likely insignificant compared to that of hydrogen sulfide. Internal acidification of the iron sulfide film may be occurring, similar to that proposed for carbon dioxide corrosion systems (Crolet, Thevenot and Nesic 1998). The case of non-protective iron sulfide film, due to steel heterogeneity and/or acetic is illustrated in Figure 5.4.

The observed pitting corrosion of linepipe steels exposed to SRB culture is proposed to occur in three stages. The greater homogeneity of the API X70 steel provides for lower corrosion rates. Lower corrosion rates promote slow stable film growth with low internal stresses. Fluxes of corrosion reactants and products are also less. This is evidenced by both CTR and PR and quantitively increasing the film. This decreasing film is evidenced by a smaller decrease in CTR and PR

Figure 5.5. Repassivation is evidenced by both CTR and PR and quantitively increasing the film. This decreasing film is evidenced by a smaller decrease in CTR and PR

Figure 5.6. The thin coherent nature of the film is also indicated by a lower DLC. Pitting of the API X70 steel is the result of localized rupture of the protective film due to microbial colonization. Microbial rupture of the passive film is documented by electron microscopy and illustrated in

Figure 5.7.

Can Microbes Influence Ethanol Stress Corrosion Cracking?

Ethanol stress corrosion cracking (eSCC) is demonstrated to be an abiotic process not necessary by microbial activity. Microbial action in ethanol systems could influence eSCC behavior by one of two ways. In the first scenario, microbial conversion of ethanol to acetic acid somewhere during the ethanol production

and transportation chain could introduce acetic acid contamination into the process stream resulting in trace acetic acid concentrations. Acetic acid contamination, especially in combination with introduction of excess water has been shown to affect ethanol corrosion and cracking behavior [
Figure 5.8] (Lou and Singh 2010).

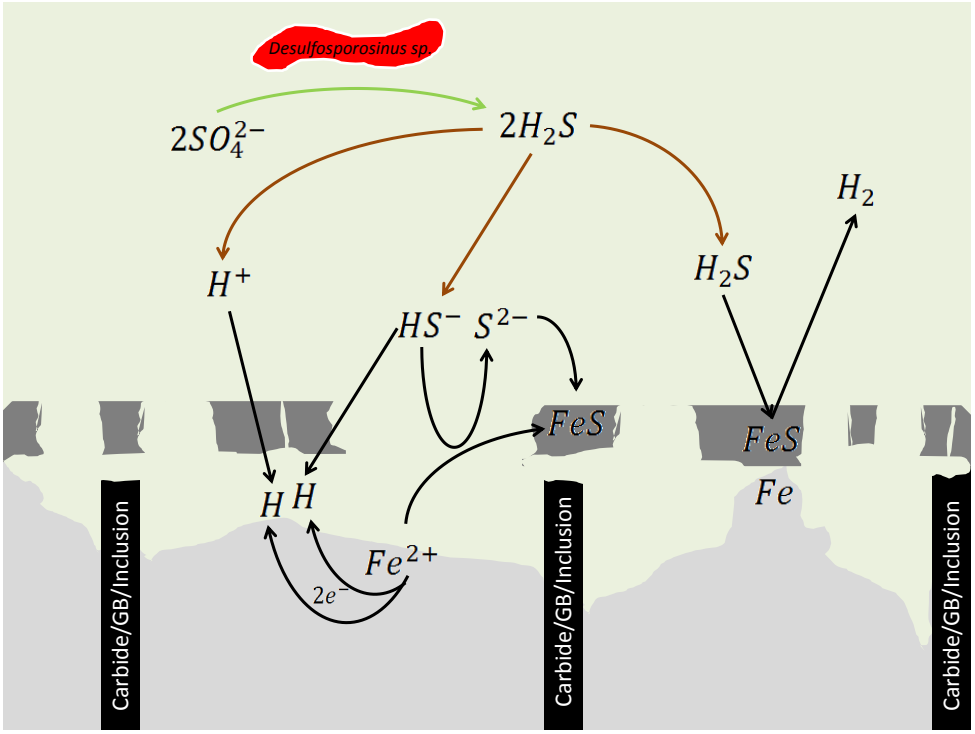

Figure 5.4 Proposed qualitative model for general corrosion of linepipe steels exposed to SRB in growth media with 2 vol. pct. ethanol

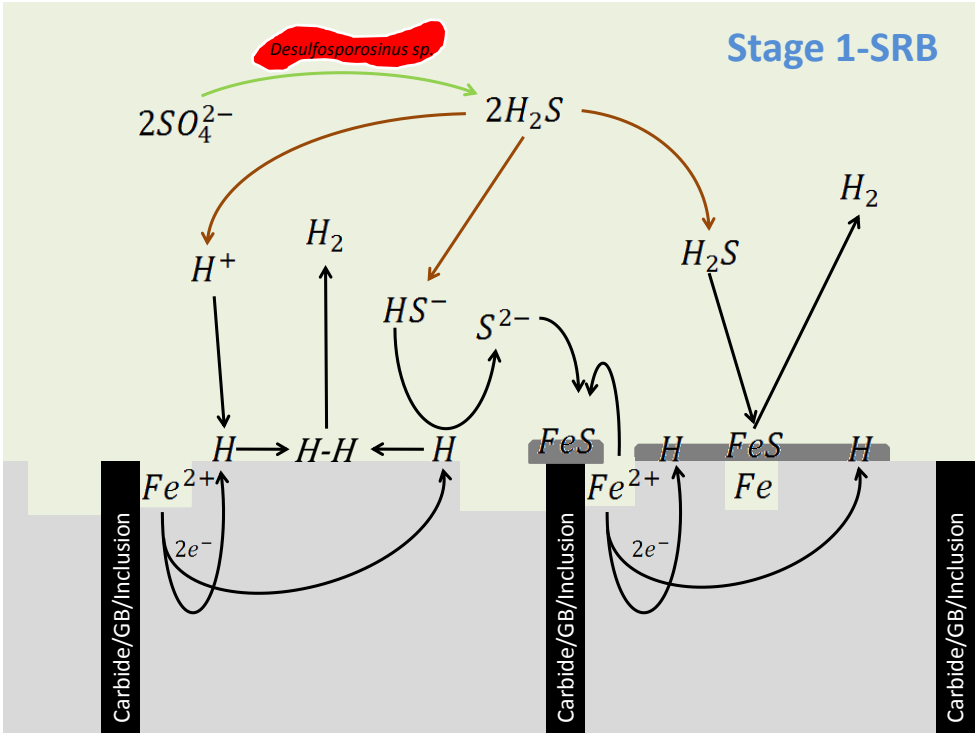

Figure 5.5 Stage 1 of proposed qualitative model for pitting corrosion of linepipe steels exposed to SRB in growth media with 2 vol. pct. ethanol

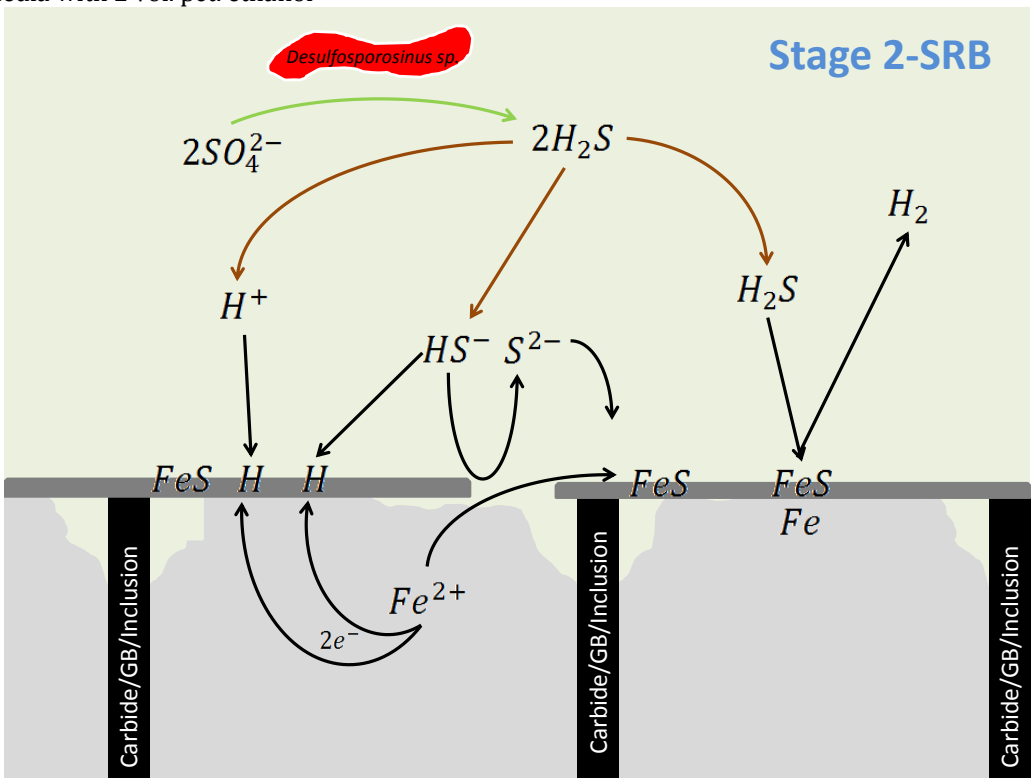

Figure 5.6 Stage 2 of proposed qualitative model for pitting corrosion of linepipe steels exposed to SRB in growth media with 2 vol. pct. ethanol

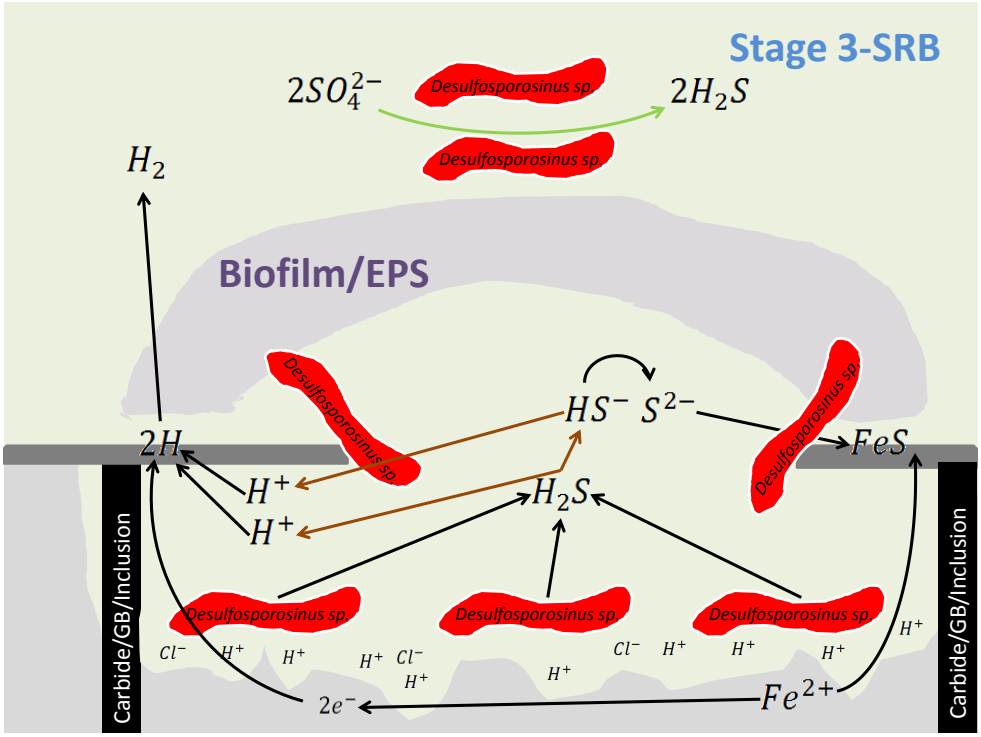

Figure 5.7 Stage 3 of proposed qualitative model for pitting corrosion of linepipe steels exposed to SRB in growth media with 2 vol. pct. ethanol

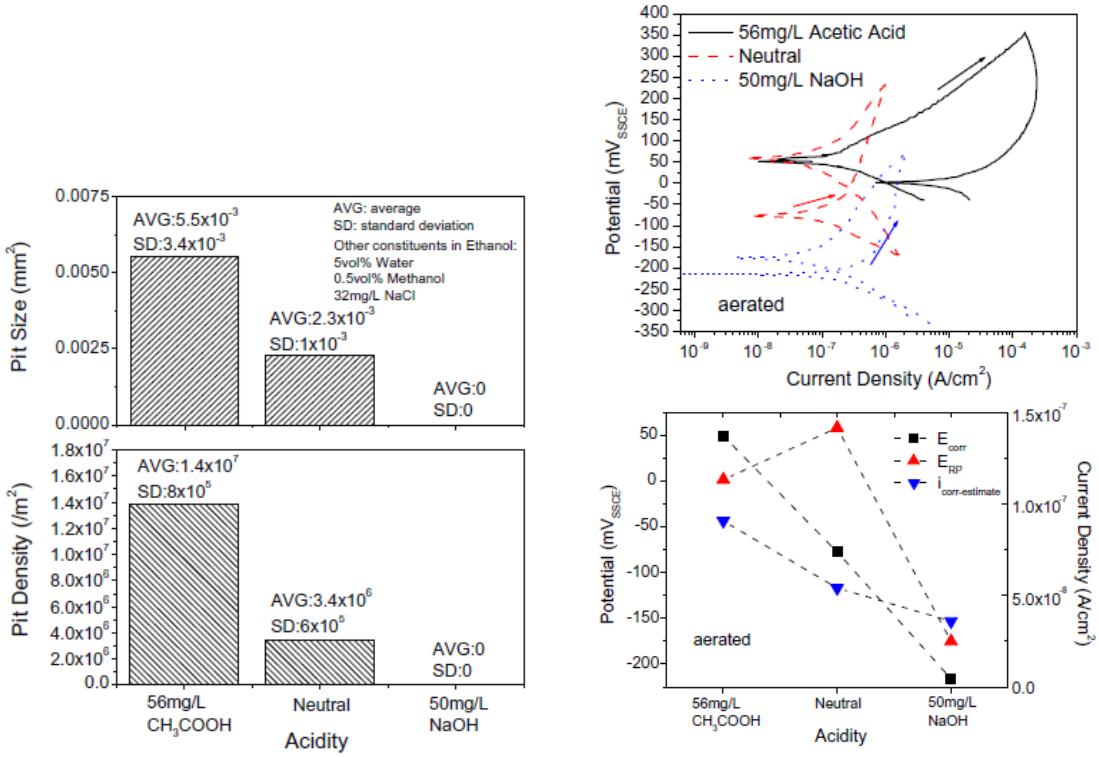

Figure 5.8 Effect of acetic acid additions to FGE on corrosion behavior of API X65 steel including (a) pitting distribution (c) potentiodynamic polarization and (d) open circuit potential and current density (Lou and Singh 2010)

In the second scenario, non-ideal conditions are experienced in a FGE system. A localized area is exposed to a water rich phase with a low concentration of ethanol. Microbes naturally occurring in the system become active and colonize the steel surface causing localized attack such as pitting. When normal conditions resume, the microbial colony may be inactivated or removed; however, a stress concentrator may remain on the surface. This stress concentrator could serve as a site of initiation for eSCC if other environmental conditions are satisfied. A FGE storage tank failure due to cracking (identified during the microbial field survey) is shown in Figure 5.9. MIC pitting occurred when the tank was used to contain heavy oil. Subsequently, when the tank was used to contain FGE, eSCC initiated from the existing pits.

Figure 5.9 Intergranular ethanol stress corrosion cracking (eSCC) of carbon steel initiating from a MIC pit developed under previous service conditions

How Can a Mechanical Testing System Analyze the Effect of Cyclic Elastic Stress on Corrosion and Embrittlement?

A multi-specimen four-point bend testing (MSBT) system and method were developed to analyze the effect of cyclic elastic stress on corrosion and environmental crack initiation. As described, the system met design criteria:

1) Apply dynamic loading conditions
2) Contain corrosive media at room temperature and pressure
3) Control aeration
4) Consistently apply cyclic loading over long testing durations
5) Simultaneously test multiple specimens

Can Cyclic Elastic Stresses Affect MIC in the Systems Being Studied?

As documented in Chapter 4, this investigation did not find crack initiation or reduction of yield or tensile strengths for ASTM A36 structural or API X70 linepipe steel due to cyclic elastic loading during exposure to isolated APB or SRB. These results do not prove the negative; however, this data suggest that cyclic elastic stresses do not affect MIC in the systems being studied.

Conclusion: Can environments containing ethanol enhance susceptibility of steels to MIC?

Yes. A microbial field survey has encountered suspected MIC of a steel FGE ethanol spillage containment tank [Appendix II]. Laboratory experimental results demonstrate that microbes isolated from the FGE facility, consuming 2 to 5 vol. pct. ethanol and 1 g per liter acetic acid (a metabolic derivative of ethanol) accelerate corrosion of linepipe steels. The presence of acetic acid significantly accelerates MIC by SRB. These results demonstrate the need for careful monitoring for MIC in systems containing ethanol fuels. Consideration of the increasing risk of MIC in FGE systems due to increasing domestic FGE supply is also noted.

Future Work

This investigation raises many new and exciting questions about MIC. Some topics that should be explored:

1. What is the extent of the diversity of the in situ microbial community in FGE systems?

2. Do certain industrially produced FGEs provide more complete nutrient sources for microorganisms?
3. What is the survivability of corrosion causing organisms in concentrated ethanol solutions?
4. How does acetic acid compromise iron sulfide integrity during MIC by SRB?
5. What is the effect of APB on abiotic hydrogen sulfide and carbon dioxide corrosion?

REFERENCES CITED

Abdel Aal, M. S., M. H. Wahdan, and G. K. Gomma. "Influence of Fe2+ ion on the corrosion of carbon steel." *Materials Chemistry and Physics*, 1995: 290-297.

Al Hashem, AbdulHameed, and John Crew. "Screening Test for Six Dual Biocide Regimes Against Planktonic and Sessile Populations of Bacteria." *CORROSION.* NACE International, 2004. Paper No. 04748.

Barton, L. L., and F. A. Tomei. "Characteristics and Activities of Sulfate-Reducing Bacteria." In *Biotechnology Handbooks Vol. 8 - Sulfate-Reducing Bacteria*, by L. L. Barton. New York: Plenum Press, 1995.

Beech, Iwona B., and Christine C. Gaylarde. "Recent Advances in the Study of Biocorrosion - An Overview." *Revista de Microbiologia*, 1999: 177-190.

Bentoa, F. M., and C. C. Gaylardeb. "Biodeterioration of stored diesel oil: studies in Brazil." *International Biodeterioration & Biodegradation* 47 (2001): 107-112.

Bergy, D. H., and Robert S. Breed. *Bergey's Manual of Determinative bacteriology.* Baltimore, MD: Lippincott Williams and Wilkins, 1973.

Booth, G. H. "Sulphur Bacteria in Relation to Corrosion." *J. Appl. Bacteriol*, 1964: 174-181.

Booth, G. H., and F. Wormwell. "Corrosion of Mild Steel by Sulphate-Reducing Bacteria. Effect of Different Strains of Organisms." *Proceedings of the First International Congress on Metallic Corrosion.* London: Butterworth, 1961. 341-344.

Carlson, Frank N. "Happy Birthday Ethanol Subsidies." *Medill Reports* (Medill School, Northwestern University), November 2008.

Castaneda, Homero, and Xochitl D. Benetton. "SRB-Biofilm Influence in Active Corrosion Sites Fromed at the Steel-Electrolyte Interface When Exposed to Artifiical Seawater Conditions ." *Corrosion Science*, 2007: 1169-1183.

Cetin, Demet, and Mehmet Levent Aksu. "Corrosion Bahavior of Low-Alloy Steel in the Presence of Desulfotomaculum sp." *Corrosion Science*, 2009: 1584-1588.

Cottis, Robert, and Stephen Turgoose. *Electrochemical Impedance and Noise.* Houston: NACE International, 1991.

Craig, Bruce D., ed. *Handbook of Corrosion Data.* Metals Park, OH: ASM International, 1989.

Crolet, J. L., N. Thevenot, and A. Dugstad. "Role of Free Acetic Acid on the CO2 Corrosion of Steels." *CORROSION.* NACE International, 1999. Paper No. 99024.

Crolet, J. L., N. Thevenot, and S. Nesic. "Role of Conductive Corrosion Products in the Protectiveness of Corrosion Layers." *Corrosion*, 1998: 194-203.

Curley, Michael. "Can Ethanol be Transported in Multi-product piplines?" *Pipeline and Gas Journal*, 2008.

De Marco, Roland, Zhong-Tao Jiang, Doug John, Matthew Sercombe, and Brian Kinsella. "An in situ Electrochemical Impedance Spectroscopy/Synchrotron Radiation grazing Incidence X-Ray Diffraction Study of the Influence of Acetate on the Carbon Dioxide Corrosion of Mild Steel." *Electrochimica Acta*, 2007: 3746-3750.

de Romero, Matilde F. "The Mechanism od SRB Action in MIC Based on Sulfide Corrosion and Iron Sulfide Corrosion Products." *CORROSION.* NACE International, 2005. Paper No. 05481.

Dexter, S. C., D. J. Duquette, O. W. Seibert, and H. A. Videla. "Use and Limitations of Electrochemical Techniques for Investigating Microbiological Corrosion." *Corrosion*, 1991: 308-319.

Dexter, Stephen C. "Microbiologically Influenced Corrosion." In *ASM Handbook 13A - Corrosion: Fundamentals, Testing, and Protection*, edited by Stephen D. Cramer and Bernard S. Covino. ASM International, 2003.

Dias, O. C., and M. C. Bromel. "Microbially Induced Organic Acid Underdeposit Attack in a Gas Pipeline." *Environment Treatment & Control*, 1990: 53-56.

Dougherty, J. L. "A Review of the Effect of Organic Acids on CO2 Corrosion." *CORROSION.* NACE International, 2004. Paper No. 04376.

Dowling, N. J.E., S. A. Brooks, T. J. Phelps, and D. C. White. "Effects of Selection and Fate of Substrate Supplied to Anaerobic Bacteria Involved in the Corrosion of Pipe-line Steel." *Journal of Industrial Microbiology*, 1992: 207-215.

Edyvean, R. G. J. "Hydrogen Sulphide - A Corrosive Metabolite." *International Biodeterioration*, 1991: 109-120.

"Ethanol Road Mapping Workshop." Pipeline and Hazardous Materials Safety Administration, U.S. Department of Transportation, Dublin, OH, 2007.

Fontana, Mars G., and Norbert D. Greene. *Corrosion Engineering.* New York: McGraw-Hill Book Company, 1967.
Frankel, Gerald S. "Electrochemical Techniques in Corrosion: Status, Limitations, and Needs." *Journal of ASTM International*, 2008: Paper ID JAI101241.
Gangloff, R. P., and R. G. Kelly. "Microbe-Enhanced Environemental Fatigue Crack Propagation in HY 130 Steel." *Corrosion*, 1994: 345-354.
George, K. S., and S. Nesic. "Investigation of Carbon Dioxide Corrosion of Mild Steel in the Presence of Acetic Acid Part 1: Basic Mechanisms." *Corrosion*, 2007: 278-186.
Gibbon, Donald L., and Mehrooz Zamanazadeh. "Detection and Indentification of Microbially Influenced Corrosion (MIC) in Steels." *CORROSION 2008.* NACE International, 2008. Paper No. 08502.
Gibbon, Donald L., and Mehrooz Zamanzadeh. "Detection and Identification of Microbially Influenced Corrosion (MIC) of Steels." *CORROSION.* NACE International, 2008. Paper No. 08502.
Gonzalez, J. E.G., F. J.H. Santana, and J. C. Mirza-Rosca. "Effect of Bacterial Biofilm on 316 SS Corrosion in Natural Seawater by EIS." *Corrosion Science*, 1998: 2141-2154.
Grunwald, Ernest, and Benjamin J. Berkowitz. "The Measurement and Correlation of Acid Dissociation Constants for Carboxylic Acids in the System Ethanol-Water." *J. Am. Chem. Soc.*, 1951: 4939-4944.
Gulbrandsen, Egil, and Katerina Bilkova. "Solution Chemistry Effects on Corrosion of Carbon Steels in Presence of CO2 and Acetic Acid." *CORROSION.* NACE International, 2006. Paper No. 06364.
Gunaltun, Y. M., Ahmed Belghazi, and Totalfina Elf. "Control of Top of the Line Corrosion by Chemical Treatment." *CORROSION.* NACE International, 2001. Paper No. 01033.
Hamilton, W. A. "Sulphate-Reducing Bacteria and Anaerobic Corrosion." *Annual Review of Microbiology*, 1985: 195-217.
Heitz, E, H.C Flemming, and W Sand. *Microbially Influenced Corrosion of Materials.* Berlin: Springer, 1996.
Hibbeler, R.C. *Mechanics of Materials.* 6th. Upper Saddle River, New Jersey: Pearson Prentice Hall, 2005.
Hill, E. C., and G. C. Hill. "Microbial Contamination and Associated Corrosion in Fuels During Storage, Distribution and Use." *Advanced Materials Research* 38 (2008): 257-268.
Jack, T. R., M. J. Wilmott, and R. L. Sutherby. "Indicator Minerals Formed During External Corrosion of Line Pipe." *Materials Performance*, Nov 1995: 19-22.
Javaherdashi, R. *MIC and Cracking of Mild and Stainless Steels.* Saarbrucken: VDM Verlag Dr. Muller, 2010.
Javaherdashti, R., R. K. Singh Raman, C. Panter, and E. V. Pereloma. "Microbiologically Assisted Stress Corrosion Cracking of Carbon Steel in Mixed and Pure Cultures of Sulfate Reducing Bacteria." *International Biodeterioration and Biodegradation*, 2006: 27-35.
Javaherdashti, Reza. *Microbiologically Influenced Corrosion.* London: Springer-Verlag, 2008.
Jones, Russell H. *Principles and Prevention of Corrosion.* Upper Saddle River, NJ: Prentice-Hall, Inc., 1996.
Kane, R. D, and D. Eden. *Stress Corrosion Cracking of Carbon Steel in Fuel-Grade Ethanol: Review, Experience Survey, Field Monitoring, and Laboratory Testing.* API Technical Report, Amercan Petroleum Institue, 2007, Part I.
Kane, R. D., and M. S. Cayard. "Roles of H2S in the Behavior of Engineering Alloys: A Review of Literature and Experience." *CORROSION.* NACE International, 1998. Paper No. 274.
Kelly, Robert G., John R. Scully, David W. Shoesmith, and Rudolph G. Buchheit. *Electrochemical Techniques in Corrosion Science and Engineering.* New York: Marcel Dekker, Inc., 2003.
King, R. A., and J. D. Miller. "Corrosion by the Sulphate-Reducing Bacteria." *Nature*, 1971: 491-492.
Klemps, R., H. Cypionka, F. Widdel, and N. Pfennig. "Growth with hydrogen, and further physiological characteristics of Desulfotomaculum species." *Arch Microbiol*, 1985: 203-208.
Kock, Bongers, Thompson, Virmani, Payer. *Corrosion Costs and Preventive Strategies in the United States.* Publicaiton No. FHWA-RD-01-156, Houston, TX: NACE International, 2002.
Kuang, Fei, Jia Wang, Li Yan, and Dun Zhang. "Effects of Sulfate-Reducing Bacteria on the Corrosion Behavior of Carbon Steel." *Electrochimica Acta*, 2007: 6084-6088.
Larrey, D., and Y. M. Gunaltun. "Correlation of Cases of Top of Line Corrosion with Calculated Water Condensation Rates." *CORROSION.* NACE International, 2000. Paper No. 00071.
Lee, Anthea K., Martin G. Buehler, and Dianne K. Newman. "Influence of a Dual-Species Biofilm on the Corrosion of Mild Steel." *Corrosion Science*, 2006: 165-178.
Li, SeonYeob, YoungGeun Kim, Kyung Jeon, and YoungTai Kho. "Microbiologically Influenced Corrosion of Underground Pipelines Under the Disbonded Coatings." *Metals and Materials*, 2000: 281-286.

Little, B., P. Wagner, and D. Duquette. "Microbiologically Induced Increase in Corrosion Current Density of Stainless Steel Under Cathodic Protection." *Corrosion*, 1988: 270-274.
Little, B., P. Wagner, and F. Manfield. "Microbiologically Influenced Corrosion of Metals and Alloys." *International Materials Reviews* 36, no. 6 (1991): 253-272.
Little, Brenda J., and Jason S. Lee. *Microbiologically Influenced Corrosion.* Hoboken, New Jersey: John Wiley and Sons, Inc., 2007.
Little, Brenda J., and P. Wagner. "Myths Related to Microbiologically Influenced Corrosion." *Materials Perfromance* 36, no. 6 (1997): 40-44.
Lou, X., D. Yang, and P. M. Singh. "Effect of Ethanol Chemistry on Stress Corrosion Cracking of Carbon Steel in Fuel-Grade Ethanol." *Corrosion*, 2009: 785-797.
Lou, Xiaoyuan, and Preet M. Singh. "Role of water acetic acid and chloride on corrosion and pitting bahavior of carbon steel in fuel-grade ethanol." *Corrosion Science*, 2010: 03-34.
Lou, Xiaoyuan, Di Yang, and Preet M. Singh. "Film Breakdown and Anodic Dissoluiton during Stress Corrosion Cracking of Carbon Steel in Bioethanol." *Journal of The Electrochemical Society*, 2010: 86-94.
Madigan, M. T., and J. M. Martinko. *Brock Biology of Microorganisms.* New Jersey: Pearson Prentice Hall, 2006.
Manfield, F., M. W. Kendig, and S. Tsai. "Recording and Analysis of AC Impedance Data for Corrosion Studies II. Experimental Approach and Reseults." *Corrosion*, 1982: 570-580.
Mansfeld, Flordian. "Recording and Analysis of AC Impedance Data for Corrosion Studies I. Background and Methods of Analysis ." *Corrosion*, 1981: 301-307.
Mansfeld, Florian, and Brenda Little. "A Technical Review of Electrochemical Techniques Applied to Microbiologically Influenced Corrosion." *Corrosion Science*, 1991: 247-272.
Mendez, C., et al. "Effect of Acetic Acid, pH and MEG on the CO2 Top of the Line Corrosion." *CORROSION.* NACE International, 2005. Paper No. 05278.
Miller, J. D. "Metals." *Microbial Biodeterioration*, 1981: 149-202.
Miranda, E., et al. "Biocorrosion of Carbon Steel Alloys by an Hydrogenotrophic Sulfate-Reducing Bacterium Desulfovibrio capillatus isolated from a Mexican Oil Field Separator." *Corrosion Science*, 2006: 2417-2431.
Moussa, M. N., M. M. El-Tagoury, A. A. Radi, and S. M. Hassan. "Carboxylic Acids as Corrosion Inhibitors for Aluminum in Acid and Alkaline Solutions." *Anti-Corrosion Methods and Materials*, 1990: 4-8.
Munoz, Leonardo De Silva, Bergel Alain, and Regine Basseguy. "Role of the Reversible Electrochemical Deprotonation of Phosphate Species in Anaerobic Biocorrosion of Steels." *Corrosion Science*, 2007: 3988-4004.
NACE. *Corrosion by Acetic Acid.* NACE Technical Committee Report, Task Group T-54-3, NACE, 1960.
Perez, Adgar Joe, Roman Cabrera-Sierra, Ignacio Gonzales, and Florina Ranirez-Vives. "Influenced of Desulfovibrio sp. Biofilm on SAE 1018 Carbon Steel Corrosion in Synthetic Marin Medium." *Corrosion Science*, 2007: 3580-3597.
Pfennig, N., and H. Biebel. "The Dissimilatory Sulfate-Reducing Bacteria." In *The Prokaryotes: A Handbook on Habitats, Isolation and Identification of Bacteria*. Springer, 1986.
Pope, D. H., and E. A. Morris III. "Some experiences with microbiologically-influenced corrosion." *Mater Perfrom*, 1995: 23-28.
Pope, Daniel H., Timothy P. Zintel, A. K. Kuruvilla, and Oliver W. Siebert. "Organic Acid Corrosion of Carbon Steel: A Mechanism of Microbiologically Influenced Corrosion." *CORROSION.* St. Louis: NACE International, 1988. Paper No. 79.
Prazak, M., and K. Barton. "The Estimation of Corrosion Velocity by Measuring Polarization Resistance." *Corrosion Science*, 1967: 159-163.
Renewable Fuels Association. 2008.
RFA. *Historic U.S. fuel Ethanol Production.* 2011. http://www.ethanolrfa.org/pages/statistics#B (accessed 8 16, 2011).
Robertson, W. J., J. P. Bowman, P. D. Franzmann, and B. J. Mee. "Desulfosporosinus meridiei sp. nov., a spore-forming sulfate-reducing bacterium isolated from gasoline-contaminated groundwater." *Int J Syst Bacteriol*, 2001: 133-140.
Robinson, M. J., and P. J. Kilgallon. "Hydrogen Embrittlement of Cathodically Protected High-Strength, Low-Alloy Steels Exposed to Sulfate-Reducing bacteria." *Corrosion*, 1994: 626-635.
S., K. Singh, and A. K. Mukherjee. "Kinetics of Mild Steel Corrosion in Aqueous Acetic Acid Solutions." *J. Mater. Sci. Technol.*, 2010: 264-269.

Sauer, Karin, Anne K. Camper, Garth D. Ehrlich, J. Willian Costerton, and David G. Davies. "Pseudomonas aeruginosa Displays Multiple Phenotypes during Development as a Biofilm." *Jounral of Bacteriology* 184, no. 4 (2002): 1140-1154.
Scully, J. R. "Polarization Resistance Method for Determination of Instantaneous Corrosion Rates." *Corrosion*, 2000: 199-218.
Sheng, Xiaoxia, Yen-Peng Ting, and Simo Olavi Pehkonen. "The Influence of Sulphate-Reducing Bacteria Biofilm on the Corrosion of Stainless Steel AISI 316." *Corrosion Science*, 2007: 2159-2176.
Sherar, B. W.A., I. M. Power, P. G. Keech, S. Mitlin, G. Southam, and D. W. Shoesmith. "Characterizing the Effect of Carbon Steel Exposed in Sulfide Containing Solutions to Microbially Induced Corrosion." *Corrosion Science*, 2010: 955-960.
Singer, M., B. Brown, A. Camancho, and S. Nesic. "Combined Effect of Carbon Dioxide, Hydrogen Sulfide, and Acetic Acid on Bottom-of-the-Line Corrosion." *Corrosion*, 2011: ISSN 0011-9312.
Singer, M., S. Nesic, and Y. Gunaltun. "Top of the Line Corrosion in Presence of Acetic acid and Carbon Dioxide." *CORROISON.* NACE International, 2004. Paper No. 04377.
Singh, M M, and A Guta. "Corrosion Behavior of Mild Steel in Acetic Acid Solutions." *Corrosion*, 2000: 371-379.
Spear, J.R, Walker J.J, McCollom T., and Pace N.R. "From the Cover: Hydrogen and Bioenergetics in the Yellowstone Geothermal Ecosystem." *Proceedings of the National Academy of Science.* 2005. 2555-2560.
Stackebrant, E., C. Sproer, F. Rainey, J. Burghardt, O. Pauker, and H. Hippe. "Phylogenic analysis of the genus Desulfotomaculum: evidence for the misclassification of Desulfotomaculum guttoideum and description of Desulfotomaculum orientis as Desulfosporosinus gen. nov., comb. nov." *Int J Syst Bacteriol*, 2001: 133-140.
Starosvetsky, D., J. Starosvetsky, R. Armon, and Y. Ein-Eli. "A Peculiar Cathodic Process During Iron and Steel Corrosion in Sulfate Reducing Bacteria (SRB) Media." *Corrosion Science*, 2010: 1536-1540.
Stott, J. F.D. "What Progress in the Understadning of Microbially Induced Corrosion Has Been Made in the Last 25 Years? A Personal Viewpoint." *Corrosion Science* 35, no. 1-4 (1993): 667-673.
Suflita, J. M., T. J. Phelps, and B. Little. "Carbon Dioxide Corrosion and Acetate: A Hypothesis on the Influence of Microorganisms." *Corrosiion*, 2008: 854-859.
Sun, W., and S. Nesic. "A Mechanistic Model of Uniform Hydrogen Sulfide/Carbon Dioxide Corrosion of Mild Steel." *Corrosion* (NACE International), 2009: 291-307.
Thomas, C. J., G. J. Edyvean, and R. Brook. "Biologically Enhanced Corrosion Fatigue." *Biofouling*, 1988: 65-77.
Tiller, A. K. "Aspects of Microbial Corrosion." *Corrosion Processes*, 1982: 115-159.
Videla, Hector A. *Manual of Biocorrosion.* Boca Raton, Florida: CRC Press, Inc., 1996.
Videla, Hector K., and Liz K. Herrera. "Microbiologically Influenced Corrosion: looking to the future." *International Microbiology* , 2005: 169-180.
von Wolzgogen, C. A.H., and L. S. van der Klught. "Graphication of Cast Iron as an Electrochemcial Process in Anaerobic Soils." *Water*, 1934: 147-165.
Walker, J. J., J. R. Spear, and N. R. Pace. "Geobiology of a Microbial Endolithic Community in the Yellowstone Geothermal Environment." *Nature*, 2005: 1011-1014.
Wolfgang, Sand. "Microbial Mechanisms of Deterioration of Inorganic Substrates - A general mechanistic overview." *International Biodeterioration and Biodegradation* 40, no. 2-4 (1997): 183-190.
Xu, Jin, et al. "The Effects of Sulfate Reducing Bacteria on Corrosion of Carbon Steel Q235 Under Simulated Disbonded Coatings by Using Electrochemical Impedance Spectroscop." *Corrosion Science*, 2011: 1554-1562.
Zamarin, Chad. "Pipeline Industry Needs and Experiences." *Ethanol/Pipeline Technology Road Mapping Workshop.* Dublin, OH: Colonial Pipeline Company, October 26, 2007.
Zobell, Claude E. "Action of Microorganisms on Hydrocarbons." *Bacteriol Rev.*, 1946: 1-49.
Zuo, R., et al. "Inhibiting Mild Steel Corrosion from Sulfate-Reducing Bacteria Using Antimicrobial-producing Biofilms in Three-Mile-Island Process Water." *Appl Microbiol Biotechnol*, 2004: 275-283.

APPENDIX A STEEL MATERIALS

The ASTM A-36 sheet steel was provided without information about composition or mechanical properties. The API X52 and API X70 steels were provided with information about chemical composition. Characterization of ASTM A-36 steel included establishing mechanical properties using tensile testing according to ASTM E-8 and identifying microstructure and rolling direction using light metallographic techniques. Table A- 1 lists the results of chemical analysis by optical emission spectroscopy (OES) [

Table A- 1 Chemical composition in wt pct. for steel materials

ASTM A-36 Grade Steel												
C	S	P	Si	Cr	Ni	Mn	Cu	Mo	Nb	Ti	Al	V
0.22	0.01	0.01	0.04	0.08	0.08	0.9	0.23	0.02	<0.01	<0.01	0.03	<0.01
API 5L X-52 Grade Steel												
C	S	P	Si	Cr	Ni	Mn	Cu	Mo	Nb	Ti	Al	V
0.070	0.008	0.008	0.195	0.030	0.020	1.050	0.050	0.004	0.021	0.001	0.029	0.003
API 5L X-70 Grade Steel												
C	S	P	Si	Cr	Ni	Mn	Cu	Mo	Nb	Ti	Al	V
0.050	0.006	0.012	0.185	0.043	0.017	1.505	0.030	0.010	0.084	0.015	0.032	0.010

The mechanical properties of the ASTM-A36 structural steel and API 5L X42 and API 5L X70 linepipe steels were characterized through tensile testing in accordance with ASTM E-8 in longitudinal and transverse directions. For each material and specimen orientation, triplicate tests were performed. From the tensile data, the 0.2 pct. offset yield stress, ultimate tensile stress (UTS), and total elongation to failure were measured. These data are listed in Table A- 2.

The micrographs shown in Figure A-1 are representative of the microstructures of the steels. The ASTM A36 steel microstructure [Figure A-1 (a)] is composed of ferrite and pearlite. The API X52 steel microstructure [Figure A-1 (b)] is also composed of ferrite and pearlite but contains significantly less pearlite than the ASTM A36 steel. The API X70 steel microstructure [Figure A-1 (c)] is composed of acicular ferrite. Grain size is noticeably more refined for the API X70 steel when comparing with the ASTM A36 and API X52 steels.

Table A- 2 Mechanical property data for the ASTM A36, API 5L X42, and API 5L X70 steels from tensile test data

Specimen Material Type	Elastic Modulus (GPa)		0.2% Offset Yield Strength (MPa)		Ultimate Tensile Strength (MPa)		Total Elongation (%)	
	Average	STDEV	Average	STDEV	Average	STDEV	Average	STDEV
MIC A36L	175	3.3	292	3.1	451	0.5	37.8	1.8
MIC A36T	186	22.5	289	2.2	453	1.6	34.8	1.6
MIC X42L	190	5.9	397	4.2	491	1.0	30.9	0.3
MIC X42T	213	6.1	402	10.8	504	1.7	30.4	1.1
MIC X70L	215	8.8	561	14.5	655	9.1	24.9	1.2
MIC X70T	226	4.5	575	6.3	665	5.7	24.6	0.8

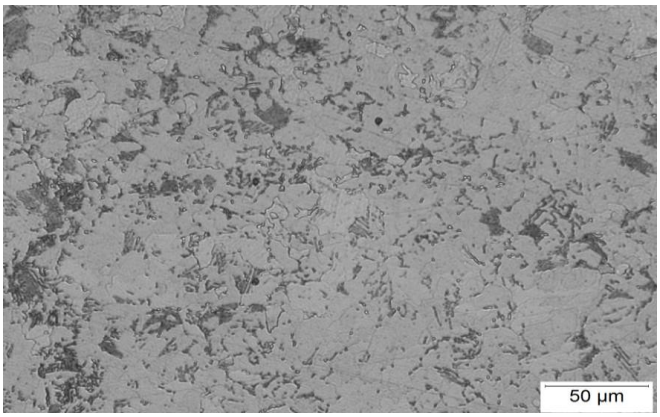

(a)

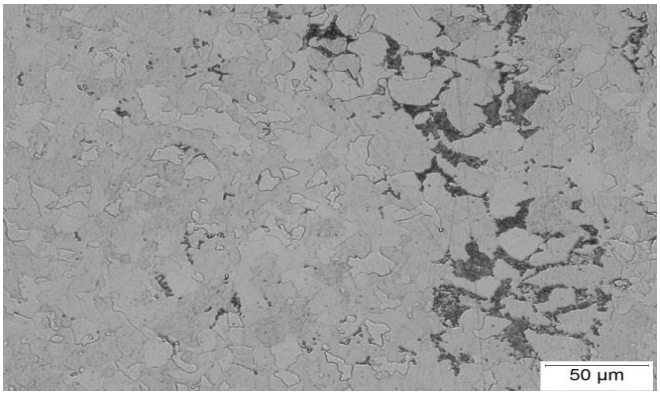

(b)

(c)

Figure A-1 Light microscopy for (a) ASTM A36 steel, (b) API X52 steel, and (c) API X70 steel etched with 2 pct. nital etch showing microstructural features

APPENDIX B MICROBIAL FIELD SURVEY

FGE underground and aboveground containment/storage tanks (UST and AST) are used to capture ethanol spillage and runoff water resulting from normal operation at fueling terminals. These types of tanks were recently discovered to have experienced internal corrosion problems. After the failure of one of these tanks, similar tanks were inspected. Many were reported to smell like acetic acid. Testing of the tank media revealed a pH of 4. As microbes are known to produce acetic acid while using ethanol as a substrate, acetic acid producing microbes were presumed to be active in the ethanol spillage tanks and suspected to be responsible for the corrosion failure. Tank bottoms samples from the ethanol contact-water tanks were acquired.

The microbial diversity of these samples was investigated with 16S rRNA gene sequencing. results indicated that acetic acid bacteria grouping within the *Alphaproteobacteria* were the most abundant

Figure B-1. These findings are consistent with previous results from similar tanks at multiple locations suggesting acetic acid bacteria are commonly present in environments associated with FGE. Acetic acid bacteria fall under a category of microbes recognized to cause MIC known as acid producing bacteria (APB). An anaerobic consortium capable of producing organic acids and reducing sulfate, grouping within the Firmicutes, were also identified as Clostridium sp. and Desulfosporosinus sp.

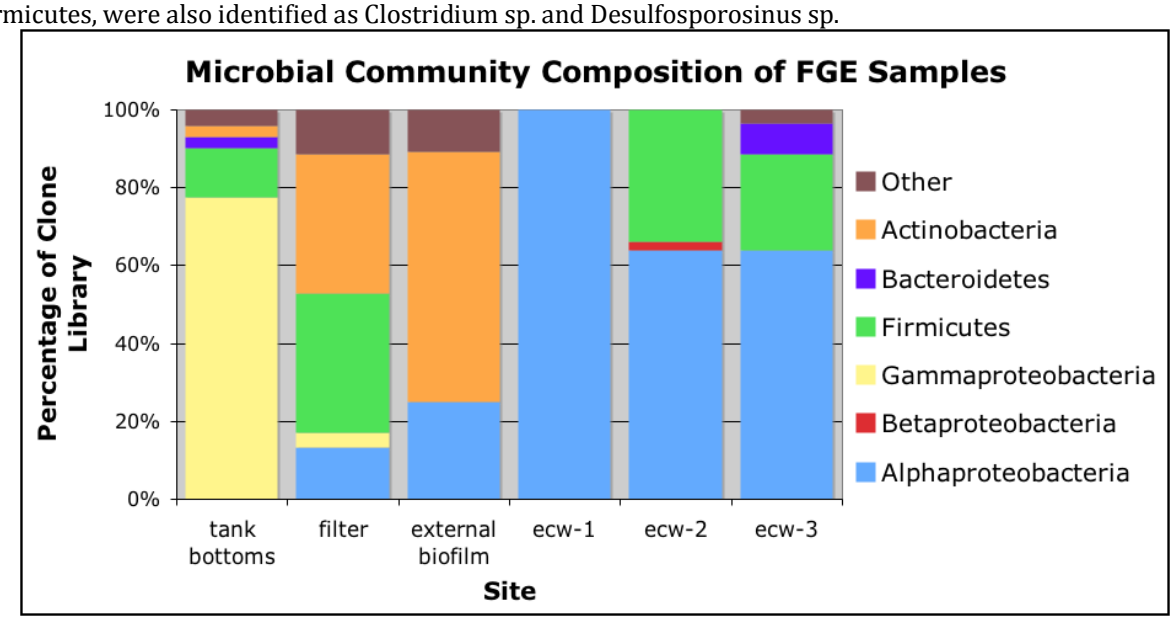

Figure B-1 Microbial community composition of field sites collected from FGE transmission systems. *Alphaproteobacteria* include APB. Firmicutes include SRB.

Isolated Acetic Acid Bacteria

The acetic acid bacteria, *Acetobacter,* are detailed in several common microbial references (Bergy 1973), (Madigan and Martinko 2006). The bacteria are gram-negative and active in aerobic environments. The genius is able to acquire energy by the oxidation of ethanol to acetic acid. *Acetobacter* can also

Figure B-2. Oxidation of ethanol to acetic acid and water via the tricarboxylic acid (Krebs) cycle. The process for conversion of ethanol to acetic acid is shown in

best known for their use as vinegar producers. The cells are ellipsoidal to rod-shaped, and around 0.6-0.8um by 1.0-4 um. The bacteria are ubiquitous in many environments and are commonly transmitted by air. Optimum temperature for growth is around 25-30°C. *Acetobacter aceti* is motile by peritrichous flagella. Optimum growth pH for these bacteria is around 5.0 to 6.5, however, they are relatively acid tolerant, surviving well below pH 4 in the present investigation. The bacteria are also able to produce cellulose. This

cellulose forms as a matrix outside the cell walls composed of a tangled network of microfibrils. In an un-agitated environment, the mass allows the bacteria to be suspended on or near the surface of the aqueous media in which they reside where dissolved oxygen concentrations are higher. When colonizing a steel surface this cellulosic substance forms biofilm facilitating adhesion and colonization.

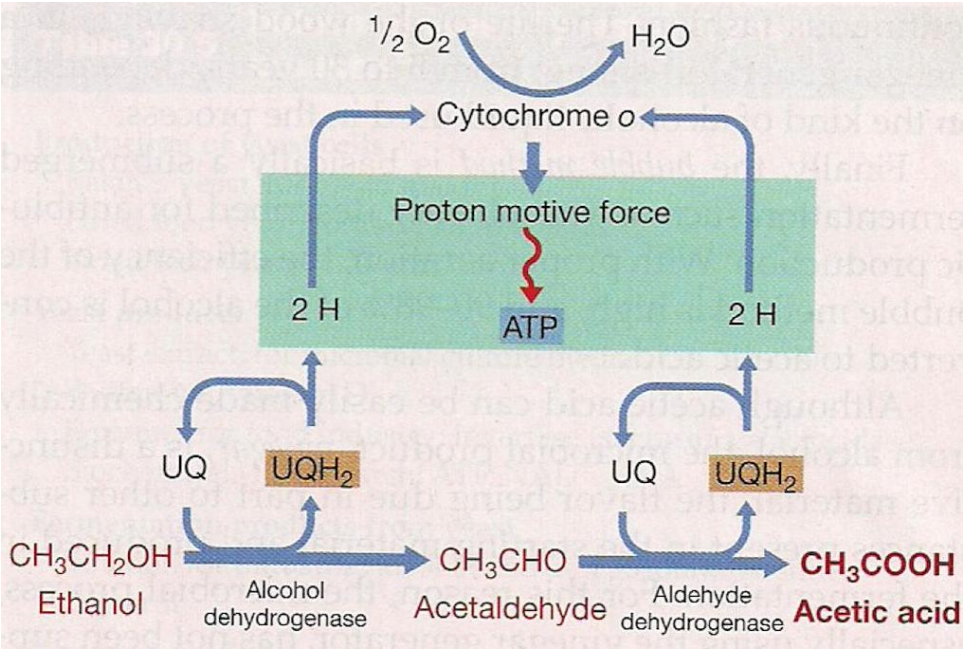

Figure B-2 Oxidation of ethanol to acetic acid by *Acetobacter aceti* (Madigan and Martinko 2006)

Isolated Sulfate-Reducing Bacteria

The isolated sulfate reducing bacteria consist of a mixed culture with microbes grouping with *Clostridium sp*. and *Desulfosporosinus sp*. Both of these microbes are Firmicutes, a phylum within the bacteria domain. The bacteria grouping with Clostridium are in the class clostridia and will be referred to as *Clostridium sp*. Both bacteria are also anaerobic.

The bacteria grouping with *Desulfosporosinus* group within the class Desulfitobacterium will be referred to as *Desulfosporosinus sp*. The *Desulfosporosinus* genus was proposed in 1997 (Stackebrant, et al. 2001). *Desulfosporosinus* were removed from the genus *Desulfotomaculum* due to their unique ability grow autotrophically using sulfate, hydrogen, and carbon dioxide (Klemps, et al. 1985). *Desulfotomaculum sp.* have been demonstrated to influence corrosion of low-alloy steel (Cetin and Aksu 2009). *Clostridia* and *Desulfotomaculum orientis* were both identified at a site of internal corrosion of an API X 42 linepipe steel nature gas pipeline (Dias and Bromel 1990). The *Desulfosporosinus sp.* has been isolated from gasoline-contaminated groundwater and known to breakdown hydrocarbons (Robertson, et al. 2001). *Desulfosporosinus orientis* have also been implicated in corrosion of mild steel (Zuo, et al. 2004).